THÈSE

En vue de l'obtention du

DOCTORAT DE L'UNIVERSITÉ DE TOULOUSE

Délivré par **l'Institut Supérieur de l'Aéronautique et de l'Espace**
Spécialité : Énergétique et transferts

Présentée et soutenue par **Bernhard WAGNER**
le 10 décembre 2009

Mesure de la concentration de vapeur autour de gouttes par absorption infrarouge

Fuel vapor concentration measurements on droplets by infrared extinction

---

JURY

M. Gérard Lavergne, président
Mme Bénédicte Cuenot
M. Fabrice Lemoine, rapporteur
M. Alain Strzelecki, directeur de thèse
M. Hubert Verdier
M. Jakob Woisetschläger, rapporteur

École doctorale : **Mécanique, énergétique, génie civil et procédés**

Unité de recherche : **Équipe d'accueil ISAE-ONERA EDyF**

Directeur de thèse : **M. Alain Strzelecki**
Co-directeur de thèse : **M. Pierre Gajan**

'In the midst of the difficulties lies the opportunity'
(Albert Einstein)

Preface

Fuel/air stoichiometry is an important parameter in modern combustion devices because it has a profound influence on efficiency, power and pollutant formation. In order to predict the distribution of local concentration values a large number of numerical models has been developed. The more sophisticated these methods become, the more it is important to confirm the accuracy of the computed results by experimental data.
Concerning non-intrusive, optical vapour concentration measurements, the most commonly used techniques are Laser Induced Fluorescence (LIF) and its enhancements (PLI(E)F,FARLIF,...). The main advantages of these approaches, the possibility of full 2D images of the vapour field and the detection of several fuel components, are sometimes overshadowed by limits in acquisition speed and the high sensitivity to concentration gradients in two-phase flows.
This thesis describes the development of a complementary measurement technique, the Infrared Extinction (IRE), around a field containing strong concentration gradients - notably a stream of monodisperse droplets - with the objective to cover the lack of information in these regions left by the LIF.
For this purpose an experimental test bench is designed and a simplified simulation of the absorption process by a droplet is created. The basis for the latter is given by existing DNS calculations on interacting droplets. Preliminary tests on both components show satisfactory results. Developed routines for signal treatment allow the separation of the absorption signal by a single droplet out of the continuous signal and the comparison of this signal to the simulations. Additionally an extension to the classic 'Onion-Peeling' deconvolution scheme, adapting it to the present experimental conditions, is proposed.
The system is applied to droplet streams of varying parameters and - in collaboration with V.Bodoc - to a free conical spray. The comparison of the experimental results to the simulated data proves the ability of the IRE to detect single droplets, but indicates also that further improvements on the experimental setup as well as on simulation and treatment are necessary to obtain the desired comparative results to the LIF.

Acknowledgments

The completion of this thesis during those last three years would not have been possible without the aid and support of a great number of people.

First of all I want to express my gratitude to my reviewers, Fabrice Lemoine and Jakob Woisetschläger for accepting to evaluate this work and for their constructive suggestions. Many thanks also to the other members of the jury, Bénédicte Cuenot, Gérard Lavergne and Hubert Verdier for showing interest in my work.
Sincere thanks to my thesis supervisors at ONERA, Pierre Gajan and Alain Strzelecki who had the difficult task to lead me through three years of challenges and who always managed to find an appropriate solution to all the unforeseen obstacles that emerged scientifically as well as organizationally.

A special mention has to be made of Fabrice Giuliani at the ITTM of TU-Graz. His unsolicited contribution as counsellor, secret reviewer and translator was beyond price.
Furthermore, I am very grateful for the contribution of the following persons:

At the ECCOMET Program: Bénédicte Cuenot for organising the pack and defending the quota at Paris, Marie Labadens and Michèle Campassens for accustoming the foreigners to French jurisdiction and bureaucracy and for always being there to help when needed.

At ONERA Toulouse: Yves Biscos, Pierre Berthoumieu, Alain Bontemps, André Alcoser and André Dillinger for the big help on all the small problems with the experimental setup.

Christoph Hassa at the DLR Cologne for the discussions about the Infrared Absorption technique, indicating me where to proceed.

Gérard Gréhan at CORIA for the patient explications on particle scattering and the provision of the software packages DiffGLMT and IntGLMT.

Frederic Grisch and Björn Rossow at ONERA-Palaiseau for insight in their experimental setup.

Not to forget all those friends, that made my life as a PhD student to an unforgettable experience.

The PhD's and Post-Docs of DMAE $2^{ème}$: Géraldine 'Gégé' Salque, Brice 'Pries' Michel, Cedric 'le plus beau professeur' Corre, Davide 'Aikido Panda' Zuzio, Jegan 'Break It' Pushparajalingam, Jochen 'Buy 3 pay 2' Wilms, Madjid 'le pôte berbère' Boukra, Nechtan 'Top Gun' LeLostec, Vincent 'Cptn. Cool' Galoul, Virginel 'l'institution de paintball' Bodoc, Vital 'ça ne rigole pas, la banane' Gutierrez, Benjamin, Christophe, Nico, Loic, Anne and everyone else, who

shared offices, some 'interesting' canteen meals and lots of coffee and tea with me during these past 36 months.

From IMFT: Laia 'le champignon' Moret, Thangasivam Gandhi and his wall of tea boxes, Dirk 'Ironman' Wunsch and Nicolas 'Nicolix' Guezennec. Thank you for all the weekend trips and multicultural dialogues that widened my horizon enormously.

At CERFACS: Björn 'Sissy' Landmann, Felix 'der Schwabe' Jägle, Jean-Mathieu 'Mr.Europa' Senoner, Nicolas 'ODIC' Gourdain, 'LeDieu' Julien Laurenceau, Thomas 'le ronflator' Guedeney, Jan-Willem van Leeuwen, Hugues Deniau and all members of our weekly football matches.

Finally I want to thank my parents for always supporting me with my plans far from home and to the emerald butterfly who carried me on its wings over all the final obstacles.

This research project has been supported by a Marie Curie Early Stage Research Training Fellowship of the European Community's Sixth Framework Program under contract number MEST-CT-2005-020426.

Contents

List of Figures

List of Tables

Chapter 1

Introduction

1.1 Motivation for this thesis

The actual situation of transport and human mobility is dominated by two very contradictory factors. On the one hand, the number of people with access to motorized transport and the volume of internationally shipped cargo is constantly rising, promoted by the fast economic development of former emerging markets such as China or India. On the other hand, the reserves of earths fossil resources are on the brink of depletion and pollution caused by exhaust gases is already at an alarming level. If humanity wants to solve this difficult situation without losing a good part of its cultural achievements, new forms of energy production have to be developed.
However, this is a big step, which will take time. Today, several ideas are investigated. Options are the replacement of fossil hydrocarbons by so-called biofuels or hydrogen, fuel cells, large-scale use of solar power or wind energy, or completely new approaches such as nuclear fission. But until at least one of these alternative technologies is ready for public use, uttermost priority must be set on rendering our present combustion processes as efficient and ecological as possible. One basic necessity to achieve this amelioration of combustion is good knowledge of the ongoing phenomena in a combustion chamber. Especially droplet formation and evaporation have a big influence on combustion speed, temperature, formation of pollutants and overall efficiency. Being able to predict the local vapor concentrations is an important step to control, and therefore optimize the combustion process.
For the purpose of this prediction a large number of numerical methods has been developed. Due to the limits of computational power, each one of these theoretical approaches contains a certain number of simplifying assumptions. The more sophisticated these hypotheses become, the more it is important to confirm the accuracy of the computed results by experimental data. In the field of vapor concentration measurement Laser Induced Fluorescence (LIF) and its enhancements (PLIF,LIEF,FARLIF) are the most commonly used techniques to obtain comparative experimental values.
The main advantages of this way of measuring the fuel concentration are the possibility to obtain 2D images of the vapor field, the distinction of several fuel components and its good adaptability to a great number of reactive and non-reactive applications. However, due to the necessity for high-power-lasers becomes the experimental equipment rather heavy and expensive.

Functional inconveniences of LIF are mostly related to the high power laser sources and CCD cameras. One point is the limitation of the acquisition frequency by the frame rate of the camera and the pulse rate of the laser. With actual cameras, a continuous monitoring of the flame, and therefore the possibility for in-situ combustion management, is only possible by trading resolution for speed. This would practically reduce LIF to a point measurement technique. The high energy needed to excite the molecules demands pulsed lasers, whose pulse frequency is mainly limited by the cooling system of the laser cavity. At the moment, this limitation is significantly below 1 kHz for conventional lasers.
Another problem is the sensibility of Laser Induced Fluorescence to strong concentration gradients in the observed field. Since the fluorescence signal is proportional to the concentration of the investigated species, a fuel droplet will cause a signal several magnitudes higher than the surrounding vapor. As a result, either the vapor concentrations become invisible due to the high threshold that is needed to display the droplets, or the signal from the liquid phase will saturate the respective cells on the CCD-chip, influencing neighbouring cells ('blooming') or even damaging the system. Several efforts to avoid this effect have been made, all with their distinctive advantages and inconveniences [1, 2, 3, 4].
However, there is also the possibility to complement the LIF results with data obtained by a technique which is immune to these limitations. Extinction methods, for example, are based on the attenuation of energy by a species rather than on excitation as LIF. For this reason, they can work at lower energies, making them insensitive to blooming effects. Due to a characteristic absorption spectrum of most hydrocarbons, the use of Lasers in the near to mid-Infrared wavelength ($780nm < \lambda < 8000nm$) is preferable for fuel investigations, leading to the term of Infrared Extinction technique (IRE). This kind of vapor concentration measurements is the main topic of this thesis.
The first use of this technique dates to the end of the seventies of the last century, measuring the extinction by coal dust particles [5]. The introduction of two-wavelengths to the extinction measurements, an absorbing and an non-absorbing one, shortly after, allowed to measure concentration of gaseous and liquid species in a non-intrusive way without delay [6, 7]. However, these first approaches still lacked in accuracy and required complicated accompanying calculations to obtain concentration results.
A great step forward was made ten years later, when extensive research on the IRE gave better understanding of the underlying physics and limitations of this technique [8, 9, 10, 11]. The obtained insights rendered Infrared extinction experiments a lot more comfortable and lead to a wide spectrum of applications, from piston engines [12] to scramjets [13] and detection of aerosols [14], today.
However, in spite of the multitude of works, using extinction measurements during the last thirty years, two points of interest persist:
First, IRE is always employed in a macroscopic way, meaning that the field to be investigated is always significantly larger than the beam diameter. This leads to the consideration of the beam width as infinitely small, automatically integrating over all the objects and effects in the beam cross-section. For the author, this is an unfortunate situation, because it neglects one of the strong points of this technique, to deal with strong concentration gradients such as droplet-vapor interfaces. Bringing the IRE to a more microscopic scale might allow to gather concentration information in the very region, where LIF meets its limits.
The second point is the lack of comparative data between these two optical measurement techniques. The 2D concentration images of Fluorescence techniques might be complemented in its

problematic regions by more robust Extinction measurements, which in turn have the limitation to be point measurements. Therefore a closer investigation of the synergetic effects between these two methods, as well as their constraints, may result in a more complete experimental description of a multiphase vapor field, than it is possible by isolated use of either of these techniques.

1.2 Objectives

Regarding these - in the author's view - interesting perspectives, the following objectives for this theses have been set:

1. Validation of IRE's ability to detect single droplets
2. Comparison of quantitative IRE results to those determined earlier by PLIF
3. Acquisition of complementary information around the droplets
4. Development of an accompanying absorption simulation tool

Point one signifies the first step of turning away of the macroscopic approach towards the investigation of the microscopic behaviour of the IRE. Once the limits of single droplets are successfully identified, more detailed vapor profiles can be developed, leading to point two and three. The final aim is to obtain a seamless characterization of a multiphase vapor field.

Concerning the first three goals, no literature about similar experiments is known to the author. The development of the simulation tool shall provide a basis for continuative research on this topic.

1.3 Organization of the Thesis

In this work the development of Infrared-Extinction measurements on a stream of monodisperse droplets is described.
Chapter 2 starts with an introduction to droplet evaporation. Afterwards the strengths and weaknesses of Laser Induced Fluorescence - representing the most commonly used technique for concentration measurements - are discussed and Infrared-Extinction is proposed as complementary technique. The section closes with a summary of the development of the IRE from its beginnings to the present state.
Chapter 3 presents a numerical simulation of the absorption process, including the choice of the employed evaporation model and its implementation into the computation routines.
In chapter 4 the experimental setup is described in detail. The requirements that lead to its design are discussed, the chosen components are presented and error sources are identified by a series of preliminary tests.

Chapter 5 is about the application of the IRE on a spray system in collaboration with V.Bodoc. The motivation for this joint-venture is given, before presenting the spray characteristics and the necessary adaptations to the test rig.
The results of both experimental configurations, droplet stream and spray, are presented and discussed in chapter 6. The former ones are compared to data obtained by Frackowiak on a similar setup, using Planar Laser Induced Fluorescence [4, 15]. The latter are matched to numerical predictions from Bodoc [16, 17].
The final chapter of this thesis summarizes the work, suggests ameliorations and gives perspectives for this technique.

Glossary

Symbol	Description	Unit
	Latin letters	
A	Surface	[m^2]
A_v	Vapour field expansion factor	[1]
A_{21}	|	
B_{12}	| Einstein coefficients	[1]
B_{21}	|	
B	Spalding number	[1]
C	Spacing parameter	[1]
C_D	Drag coefficient	[1]
Ce	D^2 evaporation constant	[m^2/s]
C_n	Number Density	[1]
C_{ps}	Chopper periods per signal	[1]
C_{p-vap}	Vapour heat capacity	[$J/(g \cdot K)$]
$\mathcal{D}$	Diffusion coefficient	[1]
D	Diameter	[m]
D_{20}	Area Mean Diameter	[m]
D_{32}	Sauter mean diameter	[m]
I	Laser irradiance	[W/m^2]
I_ν	Spectral Laser irradiance	[W/m]
$K_{drop-abs}$	Drop absorption term	[1]
$K_{drop-scat}$	Drop scattering term	[1]
K_{vapour}	Vapour absorption term	[1]
Le	Lewis number	[1]
L_v	Latent heat of evaporation	[J/g]
$\mathcal{M}$	Airy-Disc factor	[1]
$\dot{M}$	Mass flow	[kg/s]
N_A	Avogadro number	[1]
N(D)	Drop diameter distribution	[1]
Nu	Nusselt number	[1]
Nu_m	Modified Nusselt number	[1]
P	Beam power	[W]

continued on next page

Symbol	Description	Unit
P_{flu}	Fluorescence power	[W]
Pr	Prandtl number	[1]
Q_{21}	Collisional transfer coefficient	[J]
Q_{abs}	Absorption efficiency term	[1]
Q_{ext}	Extinction efficiency term	[1]
Q_{scat}	Scattering efficiency term	[1]
Q_l	Liquid mass flow	[m^3/s]
R	Optical thickness ratio	[1]
$R_{f,M}$	Diffusion boundary layer radius	[m]
R_m	Ideal gas constant	[$J/(K \cdot mol)$]
Re_p	Particular Reynolds number	[1]
Sc	Schmidt number	[1]
S_D	Distance between two droplets	[m]
Sh	Sherwood number	[1]
Sh_m	Modified Sherwood number	[1]
T	Temperature	[K]
T_{pass}	Time between the droplets in a period	[s]
T_r	Fractional transmittance	[1]
V	Velocity	[m/s]
$\dot{V}_{gas}$	Gas volume flow	[m^3/s]
X_liq	Liquid molar fraction	[mol/mol]
V_c	Calibration volume	[m^3]
$Y_{1,\infty}$	Vapour mass fraction at infinity	[kg/kg]
$Y_{1,s}$	Vapour mass fraction at the surface	[kg/kg]
c_m	Vapour concentration	[mol/m^3]
d	Object distance	[m]
f	shape factor of the confidence interval	[1]
f_{acq}	Acquisition frequency	[Hz]
h	Segment height	[m]
l	Distance	[m]
m	Mass	[kg]
n	Refraction index: real part	[1]
n	Number of elements	[1]
n_p	Number of points per respective period	[1]
p	Pressure	[Pas]
r	Radius	[m]
t	time	[s]
u,v	Intensity matrix coordinates	[m]
w	Ring width	[m]
w_b	Beam width	[m]
x,y,z	Concentration matrix coordinates	[m]

continued on next page

Symbol	Description	Unit

Greek letters

Δs	Difference in position	[m]
Δt	Time difference	[m]
Φ_0	Orifice diameter	[m]
Θ	Diffraction angle	[$^\circ$]
Ω	Collection angle	[rad]
α	Absorption cross section	[m^2/mol]
β	Shape factor	[1]
ϵ	Decadic absorption cross section	[m^2/mol]
χ_m	Molar fraction	[mol/mol]
δ	thickness	[m]
η_c	Optical efficiency	[1]
η_{corr}	Interaction correction factor	[1]
κ	Refraction index: imaginary part	[1]
λ	Wavelength	[m]
λ_{abs}	Absorbing wavelength	[m]
λ_{na}	Non-absorbing wavelength	[m]
λ_{vap}	Thermal vapour conductivity	[$W/(m \cdot K)$]
μ	Vapour mass fraction	[kg/kg]
σ	Root Mean Square value	[1]
ρ	Density	[kg/m^3]
τ_{ev}	Evaporation time	[s]

Subscripts

0	initial state
3.39	at infrared wavelength
632.8	at visible wavelength
1,2,i,n,m	counters
M	concerning mass
T	concerning temperature
beam	indicating the beam
c	center position
drop	droplet
ex	excitation
inj	injection
j	number of radial position
k	ring number
max	maximum value
neg	negative signal flank
new	computed value
opt	optimal value

continued on next page

Symbol	Description	Unit
pos	positive signal flank	
ref	reference value	
ring	concentric ring	
sat	saturated condition	
seg	segment	
spray	indicating the spray	
th	theoretical value	
vap	vapour	
∞	ambient state	
	Superscripts	
$-$	integral value	
$*$	modified for Stefan flow	

Chapter 2

Literature Survey

2.1 Evaporation of droplets

2.1.1 The D^2 law

When a liquid droplet is brought into an environment where temperature and pressure are beyond the evaporation limits of the liquid, it will vaporise, forming a gaseous air-fuel mixture. This effect is submitted to multiple physical parameters, which makes it quite delicate to model. The following explanations give an introduction to the modeling of some of those physical effects. They represent an excerpt of a more detailed work on evaporation simulation by Cochet et Frackowiak [18, 15].

The easiest case is the evaporation of an isolated droplet under static ambient conditions. This configuration has been the subject to many investigations after Spalding first described it in 1951, proposing a law named 'D^2'[19]. Following assumptions are made for this approach:

1. A perfectly spherical droplet is isolated and immobile in a static gaseous environment. This leads to a problem of spherical symmetry, so only on dimension, r, is necessary
2. The droplet consists of a mono-composant liquid
3. The process is quasi-stationary
4. Evaporation is faster than the transport of the vapor in the surrounding air
5. Heat flux by radiation is negligible
6. No gas is soluted in the liquid phase
7. Droplet temperature T_{drop} is constant and uniform
8. Gas properties (especially the vapor density 'ρ_{vap}' and the diffusion coefficient '$\mathcal{D}$') are constant and the Lewis number $Le = \frac{\lambda_{vap}}{\rho_{vap} \cdot C_{p-vap} \cdot \mathcal{D}}$ equals one.

9. The process is isobar at pressure 'p'.

Be $Y_{1,r}$ the vapor mass fraction for a given radius 'r', D_{drop} the droplet diameter, $Y_{1,\infty}$ the vapor mass fraction at infinity and $Y_{1,s}$ the mass fraction at the surface, we can derive the following expression for the evaporation rate:

$$\frac{dm_{drop}}{dt} = -2 \cdot \pi \cdot D_{drop} \cdot \rho_{vap} \cdot \mathcal{D} \cdot \ln\left(\frac{1 - Y_{1,\infty}}{1 - Y_{1,s}}\right) \tag{2.1}$$

If we express the droplet mass as a function of its diameter

$$m_{drop} = \rho_{drop} \cdot \frac{\pi \cdot D_{drop}^3}{6} \tag{2.2}$$

and substitute this expression into equation 2.1, we get:

$$\frac{D_{drop}^2}{dt} = -\frac{8 \cdot \rho_{vap} \cdot \mathcal{D}}{\rho_{drop}} \cdot \ln\left(\frac{1 - Y_{1,\infty}}{1 - Y_{1,s}}\right) \tag{2.3}$$

By integration this formula we obtain the D^2-law:

$$\begin{aligned} D_{drop}^2 &= D_{drop,0}^2 - Ce \cdot t \\ &\textit{with} \\ Ce &= \frac{8 \cdot \rho_{vap} \cdot \mathcal{D}}{\rho_{drop}} \cdot \ln\left(\frac{1 - Y_{1,\infty}}{1 - Y_{1,s}}\right) \end{aligned} \tag{2.4}$$

Therefore, it is sufficient to determine Ce to obtain the time of evaporation for a droplet. This coefficient can be calculated with the aid of the law of Clausius-Clapeyron, providing us with the saturated vapor pressure under the given conditions and, as a consequence, the vapor mass fraction at the surface, $Y_{1,s}$.
A very common application of this law is the estimation of the time span for the complete evaporation of a droplet of known initial diameter. This value is obtained by setting the left hand side of equation 2.4 to zero:

$$\tau_{ev} = \frac{D_{drop,0}^2}{Ce} \tag{2.5}$$

Other dimensionless numbers that are frequently used are the number of Spalding ,'B_M'

$$B_M = \frac{Y_{1,s} - Y_{1,\infty}}{1 - Y_{1,s}} \tag{2.6}$$

which characterizes the mass exchange at the droplet surface and the number of Spalding for heat transfer,'B_T':

$$B_T = \frac{C_{p-vap} \cdot (T_\infty - T_{surf})}{L_v} \tag{2.7}$$

For a Lewis number of Le=1, which is one of the assumptions made for this model, the two numbers, B_M and B_T, are equal.
Although this model employs heavy simplifications and is only valid for a very restricted number of applications, it has proven its worth. Many much more detailed investigations on evaporation often return to some of the hypotheses above.

2.1.2 Influence of convection

One of the assumptions taken for the D^2-law which is more than questionable for reality, is the completely static behaviour of the surrounding vapor phase. Experiments show, that a strong influence of convection on the evaporation process exists.
The modeling of this influence as proposed by Abramzon and Sirignano, postulates the presence of a gaseous film around the droplet in which the thermal and mass transfers take place. Likewise the hypothesis of spherical symmetry is sustained. To model the transfer processes inside of this film, the modified dimensionless numbers of Nusselt and Sherwood are defined. Using the thicknesses for the thermal (δ_T) and mass (δ_M) films, following expressions result:

$$Nu_m = 2 + \frac{D_{drop}}{\delta_T} \tag{2.8}$$

$$Sh_m = 2 + \frac{D_{drop}}{\delta_M} \tag{2.9}$$

These values replace the factor 2 in equation 2.1 for the evaporation rate. We see, that if there is no convection, the boundary layers approach infinity and Nu_m and Sh_m become two, which leaves us with the original expression for the isolated, static droplet.
Several authors have derived their own correlation for these two dimensionless numbers. As an example the expression of Clift et al. is given:

$$Nu_m = 1 + (1 + Re_p \cdot Pr)^{1/3} \cdot f(Re_p) \tag{2.10}$$

$$Sh_m = 1 + (1 + Re_p \cdot Sc)^{1/3} \cdot f(Re_p) \tag{2.11}$$

$$\text{if } 0.25 < (Pr, Sc) < 100$$

$$\text{with } f(Re_p) = max(1, Re^0.077_p) \text{ for } Re_p < 400$$

The numbers of Prandtl and Schmidt are written using reference values ($T_{ref}, \mathcal{D}_{ref}, ...$). This kind of taking convection into account permits to obtain global values of the mass and heat

transfer. However, forced convection around a droplet typically creates local differences which are not represented due to the assumption of spherical symmetry.

2.1.3 Considering the Stefan flow

The Stefan flow, which transports the vapor in radial direction from the droplet, results in an widening of the boundary layer surrounding the droplet. To determine the influence of this effect the thermal and mass layer thicknesses with (δ) and without Stefan flow (δ_0) are compared. Usually, a correction function like the following is applied to this ratio:

$$\frac{\delta}{\delta_0} = f(B) \tag{2.12}$$

with

$$f(B) = (1+B)^{0.7} \cdot \frac{\ln(1+B)}{B} \tag{2.13}$$

B signifies the Spalding number, for mass and thermal flow, and is ≤ 20 for this application. With the obtained correction functions f_T and f_M we can define the numbers of Nusselt and Sherwood modified for the consideration of the Stefan flow:

$$Nu^* = 2 + \frac{Nu_m - 2}{f_T} \tag{2.14}$$

$$Sh^* = 2 + \frac{Nu_m - 2}{f_M} \tag{2.15}$$

Consequently, the resulting modified expression for the evaporation rate can be written as:

$$\frac{dm_{drop}}{dt} = -\pi \cdot D_{drop} \cdot \rho_{ref} \cdot \mathcal{D}_{ref} \cdot Sh^* \cdot \ln(1+B_M) \tag{2.16}$$

or, using the thermal Spalding number:

$$\frac{dm_{drop}}{dt} = -\pi \cdot D_{drop} \cdot \frac{\lambda_{ref}}{Cp_{vap}(T_{ref})} \cdot Nu^* \cdot \ln(1+B_T) \tag{2.17}$$

2.1.4 Interaction between droplets

Another big influence on evaporation which is neglected by the D^2-law is the interaction between droplets. While the expressions given above are developed for the evaporation of a single droplet, experiments show that many differences to these predictions exist for the evaporation of a spray or a droplet stream.

Two main reasons can be given, why interaction between droplets is not negligible: Primarily, the presence of other droplets causes a modification of the vapor mass fraction at infinity $Y_{1,\infty}$. This implies a change in the evaporation rate. Secondly, important flow parameters such as velocity and temperature are altered by other droplets in the vicinity. Several investigations have been done numerically and experimentally on two or three droplets, aligned vertically, horizontally or in a triangle. In general, they all confirm changes in the values for thermal and mass transfer due to the wake of neighbouring droplets. To quantify this influence, several correlations have been developed, most of them modifying the drag coefficient C_D and introducing a spacing parameter C which represents the ratio of the distance between the droplets ,S_d, and their respective diameter D_{drop}:

$$C = \frac{S_d}{D_{drop}} \tag{2.18}$$

One example for modifications considering interaction is given by Atthasit [20] for a stream of monodisperse droplets. The first one corrects the drag coefficient:

$$C_{D-corr} = C_{D-isolated} \cdot (a \cdot \ln(C) + b) \tag{2.19}$$

with:

$$\begin{aligned} a &= 3.43 \cdot 10^{-5} \cdot Re_p^3 - 1.359 \cdot 10^{-3} \cdot Re_p^2 + 1.8753 \cdot 10^{-2} \cdot Re_p + 0.0484 \\ b &= -1.07 \cdot 10^{-5} \cdot Re_p^3 + 2.1 \cdot 10^{-4} \cdot Re_p^2 + 7.668 \cdot 10^{-4} \cdot Re_p - 0.01 \end{aligned}$$

Additionally, the terms for evaporation rate and heat flux are expanded by a corrective factor:

$$\left(\frac{dm_{drop}}{dt}\right)_{corr} = \eta_{corr} \cdot \frac{dm_{drop}}{dt} \tag{2.20}$$

and

$$Q_{total-corr} = \eta_{corr} \cdot Q_{total} \tag{2.21}$$

For the monodisperse droplet stream, Atthasit proposes the following correlation:

$$\eta_{corr} = 1 - 0.57 \cdot \left(1 - \frac{1 - exp(-0.13 \cdot (C-6))}{1 + exp(-0.13 \cdot (C-6))}\right) \tag{2.22}$$

This relation was found to be in good accordance with the experimental and numerical investigations done by B.Frackowiak [15].

2.2 (P)LIF as experimental validation technique

Laser Induced Fluorescence (LIF) is a nowadays widely used and well studied optical measurement technique. This chapter will give a general overview of its evolution, working principle and experimental devices needed. Afterwards, its difficulties when applied to two-phase environments are highlighted and a choice of experimental solutions to overcome these problems is presented. Since the LIF is not the main subject of this thesis and is only used as a comparative technique, the explanations are kept short on purpose. For more detailed information please refer to the bibliographic sources given in square brackets.

LIF is the emission of light from an atom or molecule following the excitation by a laser beam. In a LIF experiment, the molecule is initially at at lower electronic state before it is excited to an upper electronic energy level by a laser source. The wavelength of the laser light needs to be chosen so that it coincides with the absorption wavelength.
Laser-Induced-Fluorescence was first introduced as a single-point measurement technique (LIF) but was soon developed into a 2D-imaging tool (PLIF - Planar LIF). So far three strategies have been adapted for fuel concentration measurements by Laser Induced Fluorescence: Natural fluorescence by components of the fuel, fluorescence from a dopant of matching properties to the fuel and fluorescence from exciplex forming dopants. The last possibility leads to the LIEF and PLIEF techniques which are discussed in section 2.2.4.
Because the majority of fuels used in engines do not readily fluoresce with laser excitation in the visible or UV range, the second strategy using dopants has been used in most of the experiments not relying on surrogate fuels. LIF can be employed to investigate the liquid phase as well as the vapor phase of a spray. Concerning the first case, the use of LIF to determine droplet temperature has been successfully demonstrated [21, 22, 23]. When applied on the vapor phase, usually concentration measurements are the intention.
The main reason for the high popularity of the various fluorescence techniques surely is the possibility of obtaining full 2D Images containing a magnitude of information using a relatively simple setup. Additionally the application is possible as well on burning as on non-burning conditions with only minor changes to the material used. These advantages make this kind of technique a very powerful tool for quick and efficient investigation of fluids [24, 25, 1].
For the working principle of Laser Induced Fluorescence, an excellent introduction is given by H.Zhao and N.Ladommatos [26]. Excerpts of this publication are used in the following section:

2.2.1 Working principle of (P)LIF

There are five important processes following the excitation of a molecule by a laser source as shown in figure 2.1. First, the molecule can be returned to its original quantum state by laser induced stimulated emission, denoted as $B_{21}I_0$. Secondly, absorption of an additional photon can excite the molecule to higher states, even to ionized levels, shown as $B_{2i}I_0$. Thirdly, the internal energy of the system can be altered in inelastic collisions with other molecules, producing rotational and vibrational energy transfers, represented by $Q_{vib,rot}$. In many cases, the inelastic collisions with other molecules also result in electronic energy transfer(Q_{elec}), which is often referred to as 'quenching'. Fourthly, interactions between the individual atoms of the molecule

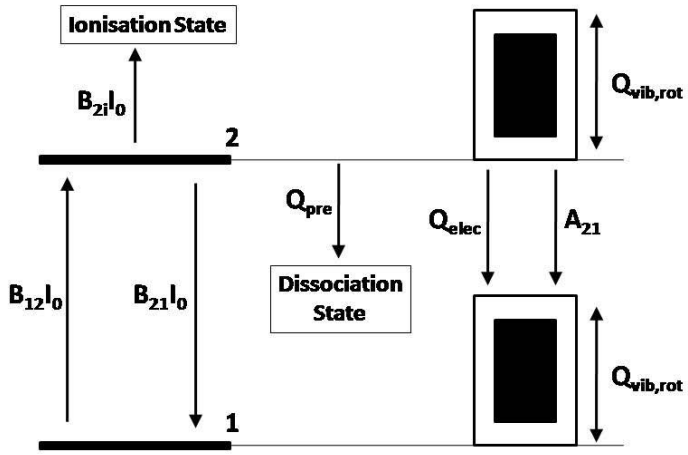

Figure 2.1: Main energy transfer processes in LIF (Source:[26])

produce internal energy transfer and dissociation of the molecule. The dissociation in this case is termed pre-dissociation as it is produced by a change from a stable to an unstable repulsive electronic state. Finally, the originally populated state, and nearby stated indirectly populated through collisions, return to lower states through the emission of light, producing the laser induced fluorescence.
In general, the fluorescence signal can be expressed as

$$P_{flu} = \eta_c \Omega V_c f_1(T) \chi_m N_A I_{\nu 0} \frac{A_{21}}{A_{21+Q_{21}}} \frac{B_{21}}{1 + \frac{I_0}{I_{sat}}} \tag{2.23}$$

$f_1(T)$ represents the fraction of molecules of the absorber species which are in the specific energy level excited by the laser and is given by a Boltzmann distribution. Therefore, the grouping $(f_1(T)\chi_m N_A)$ represents the number density of the absorbing species in the ground state. The saturation intensity I_{sat} is defined as

$$I_{sat} = \frac{A_{21} + Q_{21}}{B_{21} + B_{12}} \tag{2.24}$$

The collisional transfer coefficient, Q_{21}, represents the strength of energy loss rate due to both intermolecular and internal collisions. The more collisional losses the less radiative loss - and thus fluorescence - there will be. This energy loss process due to collision is known as quenching.

2.2.2 Basic experimental PLIF setup

The basic setup for Fluorescence investigations is shown in figure 2.2. A laser sheet enlightens a cross-section of the area of interest while the excited fluorescence can be detected by use of a

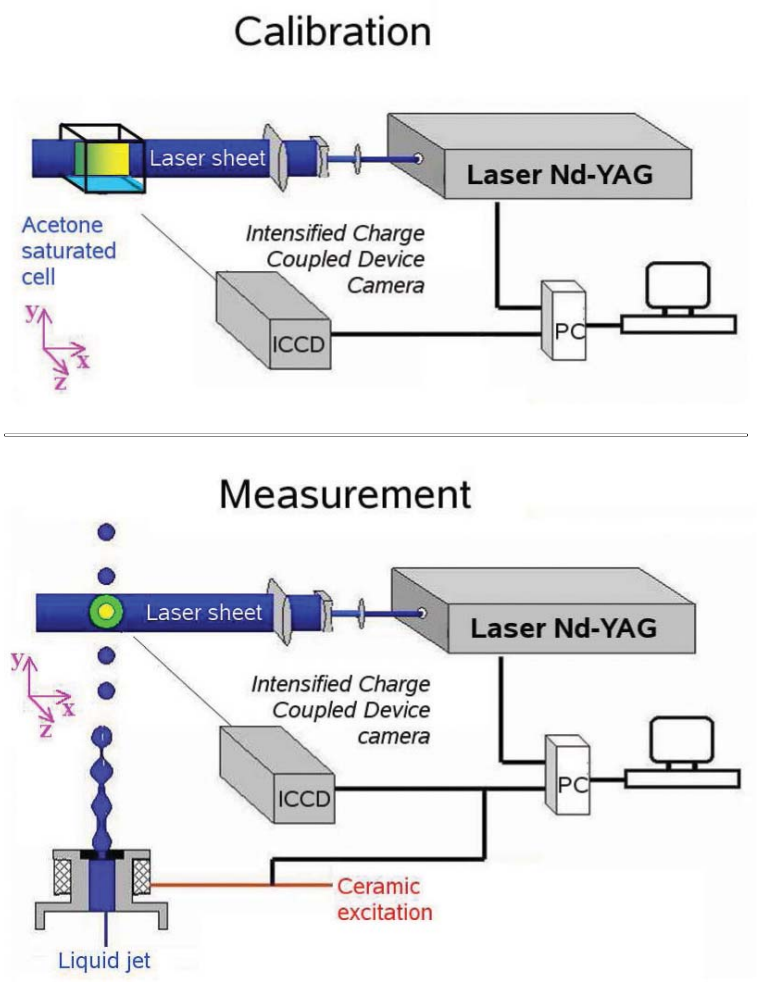

Figure 2.2: Basic PLIF setup

standard CCD-Camera eventually filter-equipped. Usually the camera is placed perpendicular to the laser sheet to obtain the highest spatial resolution. As laser source Nd:YAG lasers on second harmonic, KrF lasers or XeCl lasers with a power range from 10-400 $[mJ]$ are commonly employed. The type of laser used has to be accorded with the fuel and tracer intended. A detailed table for possible combinations of dopant and light source is given by Zhao and Ladommatos [26]. If ambient temperature and pressure rest constant for the duration of the experience, the intensity of fluorescence is direct proportional to the fuel concentration.

2.2.3 Difficulties using this technique

However, there are some flaws in these techniques as well that should not be neglected. First of all, a relatively high amount of laser power is needed to excite the desired molecules or radicals. Whereas this point has no influence on the setup itself it surely complicates the handling

and raises the costs of acquisition and maintenance of the light source. Secondly, as mentioned above, the fluorescence signal is affected by collisional energy loss between the fluorescent and ambient molecules ('Quenching') such as oxygen. While this effect plays a minor role under ambient conditions, it obliges high pressure and high temperature measurements to be performed in inert atmospheres such as nitrogen.[1].
Another minor problem is also the fluorescence of ambient species, such as water vapor, at wavelengths close to the excited one [14]. However, this can be solved by rigorous calibration.

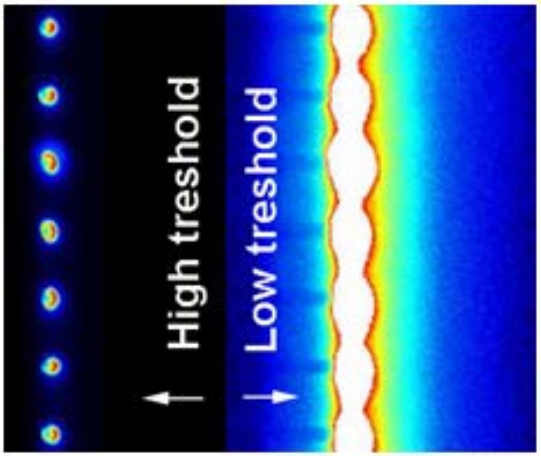

Figure 2.3: Fluorescence signal at different thresholds

The most important difficulty, when using natural tracers in two-phase flow investigations, is the sensibility of this technique towards concentration gradients. Since there is no difference in the fluorescence spectra of liquid and vapor phase, the fluorescence signal of a droplet, for example, is $\approx$ 100 times higher than that of the surrounding vapor field [15]. This leaves the experimenter with two choices: Either, a very high threshold is set for image acquisition. This allows for clear visualization of the liquid phase, but completely suppresses the vapor signal (see figure 2.3 left). Or, the threshold is lowered enough to bring out the vapor fluorescence. In this case, the signal of the liquid phase will saturate. Even if this effect does not damage the imaging hardware, it creates a 'blooming' effect. As a result, droplet diameter are severely overestimated and the liquid-vapor-interface is not directly determinable anymore [3, 15] (see figure 2.3 right). Several experimental strategies have been developed to solve this problem. Three of them are presented in the next section:

2.2.4 Experimental solutions

Use of the inflexion point

This correction, presented by M.Orain et al. [3] is based on the idea to obtain a strong signal gradient by a different optical phenomenon, in order to study the response of the imaging de-

[1]recently, this effect was used to determine the fuel/air ratio directly by determining the amount of oxygen quenching at known conditions → FARLIF (Fuel/Air ration LIF) [27, 28]

vices to this type of gradients. The technique chosen is Mie-scattering since it permits to use the same imaging system as for the main PLIF experiments on acetone droplets. As liquid ethanol is selected which, in contrary to acetone, does not fluoresce.

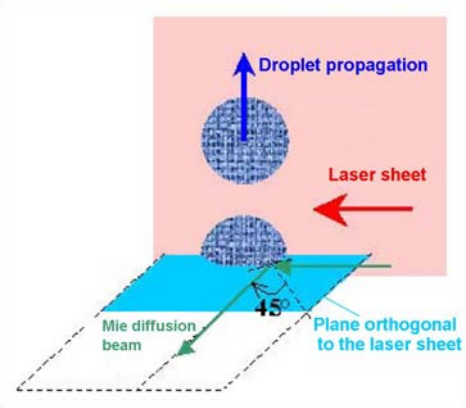

Figure 2.4: Mie scattering corresponding to the reflexion at 45° Source: [15]

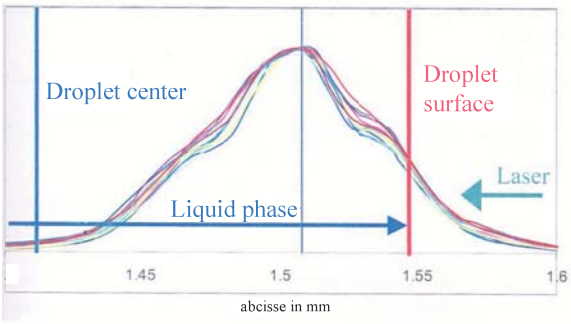

Figure 2.5: Determination of the droplet surface by aid of the inflexion point. Source: [15]

Mie-scattering theory for a droplet, which shall not be detailed in this place, gives the information that a strong maximum appears at a reflection angle of 45° to the tangent of the droplet surface (Figure 2.4) . Consequently, the detected maximum perpendicular to the laser sheet (and therefore in direction of the imaging optics) corresponds to the point where the surface tangent is 45° inclined in respect to this plane. Knowing the position of the droplet center, the droplet surface in laser direction can be derived by geometrical calculations (Figure 2.5). This value for the droplet diameter is now used to correct the blooming-affected PLIF images.
Although this technique provides a good estimation of the droplet surface, several uncertainties are highlighted by B.Frackowiak [4, 15]:

- At a closer look, two maxima, close to each other can be observed in the images of the ethanol droplets. One at the surface, resulting from Mie scattering as described above and another, being a focusing maxima of the beam inside the droplet. Since this effect can not be observed at the fluorescence signals using acetone, a different optical behaviour of the two configurations can be presumed.

- The blooming correction function, expressed by a constant factor, implies that this phenomenon is proportional to the signal gradient. This hypothesis is yet to be proven.

- To apply the proposed correction function, knowledge or a good estimation of the droplet surface temperature is necessary.

These points, together with difficulties to reproduce the acquired results of Orain et al. when using a more sensitive imaging system, motivated Frackowiak to develop a different approach during his thesis:

Masking of the droplets and calculation of the interface

The chosen strategy is partially of experimental, partially of numerical nature. To determine the vapor concentration profiles perpendicular to the droplet stream, the very simple, but effective, action of physically masking the droplets is performed. The mask consists of a blackened paper screen which is positioned by micrometric screws. The position, parallel to the illuminating laser sheet, has to be chosen carefully to neither disturb the flow field around the droplet stream nor to move out of the field depth of the recording CCD-Camera, which would result in a blurred image. Figure 2.6 shows the resulting images for the droplet stream without the mask and for three mask positions. It is visible, that even when the mask covers all of the liquid phase, resident light still perturbs the vapor fluorescence signal. For this reason, this technique delivers results until a distance of two droplet diameters from the surface only. By applying a linear extrapolation scheme this distance can be reduced to one diameter [4].

However, covering the liquid phase also hides the exact droplet positions and therefore the liquid-vapor interface. To place the droplet centers, an image without mask is used, in spite of the overestimated diameters due to blooming. The position of the interface is afterwards calculated by a numerical code: This code calculates the internal laser fluence field inside the droplet and the resulting fluorescence image using Lorenz-Mie Theory and geometrical optics. Results show, that the signal maximum is located at at distance of 5% of the droplet radius inside the droplet. Since this maximum position is unaffected by the blooming, a diameter correction can be directly applied on the bloomed images.
Using these techniques, Frackowiak manages to correct the droplet interface position by $\Delta s = 10-16\%$ (depending on the droplet diameter) in comparison to the classic way using the inflexion point (figure 2.7). The obtained vapor mole fraction profiles are coherent to those from Orain et al. as well as to further numerical simulations.

Employment of Exciplex Fluids

Another way to distinguish between the fluorescence of the liquid and the vapor phase was developed by L.A.Melton in 1993 [29]. In this method, the fluorescent molecule react in an excited state, M*, with another molecule, Qe ('Quencher'), to form a second fluorescent species (MQe)* which is bound in the excited state but not in the ground state.

$$M* + Qe \Leftrightarrow (MQe)* \tag{2.25}$$

This newly formed species is called the 'excited state complex' or 'exciplex'. The emission from the exciplex is shifted to the red with respect to that of M*. Since the reaction between the two species is reversible, it is possible to adjust the concentration of species Q so that the exciplex(MQe)* is the dominant emitter in the liquid phase and the monomer, M*, is dominant in the vapor phase. In this way, the fluorescence signals of the two phases can be separated by their respective spectra. The first exciplex to be used for diesel sprays was a mixture of naph-

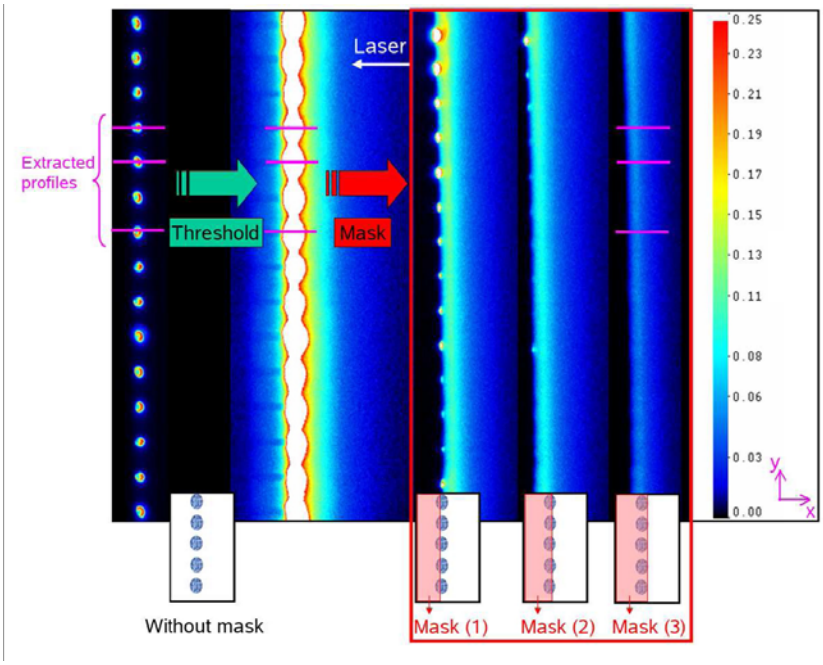

Figure 2.6: Fluorescence signals for increasing masking of the liquid phase

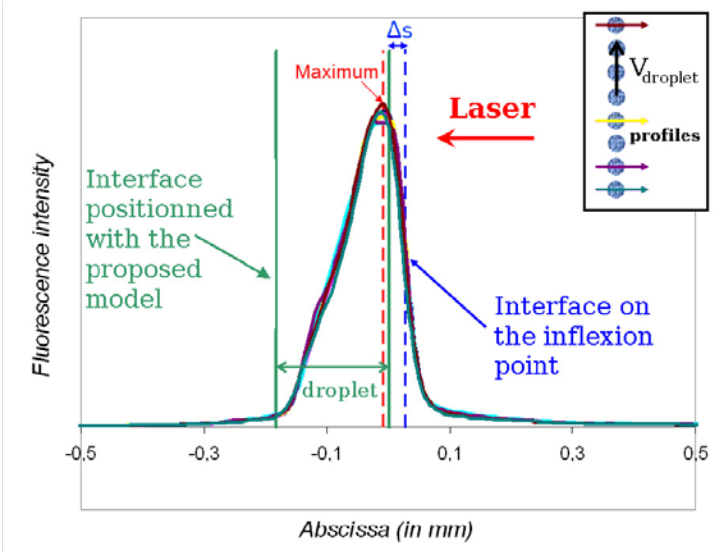

Figure 2.7: Comparison of the interface position for the two techniques. Source both images: [15]

talene (M*) and TMPD[2] (Qe). Their fluorescence spectra are presented in figure 2.8. When these tracers are used in the experiments, we speak of (P)LIEF, (Planar) Laser Induced Exciplex Fluorescence.

Over the years this technique proved to be a robust way to achieve concentration values for both phases in a direct way [30, 1]. But during this development some limitations to this technique

[2]tetramethyl-p-phenylene diamene

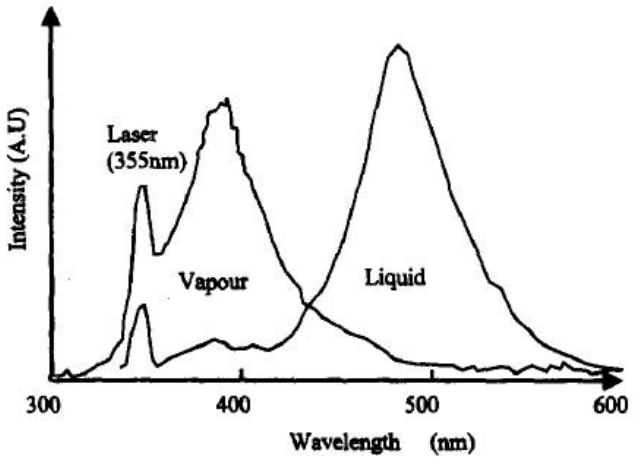

Figure 2.8: Exciplex fluorescence spectra for liquid and vapor phase (Source: [26])

showed too:
Already, there are difficulties to carry out a reliable quantitative analysis using PLIEF. For example, the estimation of the absolute liquid phase concentration requires detailed knowledge of temperature-dependent spectral emission from exciplex dopants in the spray, which is difficult to implement. Secondly, the gas-phase fluorescence is effectively quenched by oxygen. Therefore most experiments have to be carried out in nitrogen environment. A third point is that many components to form exciplexes are toxic and/or carcinogenic, which demands extreme caution at the handling of those substances. Considering the usability of PLIEF in Diesel Sprays, Desantes et al. show further limitations for vapor phase measurements [31]:
They state, that the results in the two phase coexistence zone of a spray can be significant. Exact results for fuel concentration could only be obtained in the fully evaporated zone. As error sources, cross talk of the two fluorescence signals (visible as overlap in the spectral ranges in figure 2.8) and different evaporation rates of the components are identified.

2.2.5 Conclusion

The investigations on the Laser Induced Fluorescence confirm its characterization given at the beginning of this chapter: LIF is a powerful investigation tool with the ability to provide 2D images for several species in reactive or non-reactive two-phase flows. Developments like multi color fluorescence, FARLIF or Exciplex fluorescence have further expanded the choice of applications. For that it represents - together with classic optical techniques such as PIV, LDV, PDPA or Malvern - one of the most frequently used tools to gain experimental information which helps to confirm and ameliorate numerical models.
However, as for every technique, inconveniences due to the basic physical processes involved persist. In spite of multiple attempts to bypass these flaws, the LIF rests sensitive to strong concentration gradients and secondary effects like quenching. Additionally, the high laser powers required for this method pose high demands in acquisition, maintenance and handling of the

experimental tools.

2.3 The Infrared Extinction Method (IRE)

The characterization of Laser Induced Fluorescence nourishes the wish for a complementary investigation technique, covering the 'blind spots' of LIF. This alternative should be insensitive to concentration gradients and influence from ambient species. And, in a time of economic challenges, be cost effective and compact for easy application on existing test rigs.
One solution to these requirements is the employment of laser absorption techniques. Since there is no need to excite molecules, these methods can work at low laser powers, which avoids blooming and quenching effects and allows compact, low cost equipment. For sure, these techniques have their weak sides too. The following chapter presents an absorption technique using visible and infrared wavelengths. After presenting the working principle and the history, the capabilities and the problems of this approach are discussed.

2.3.1 Working principle

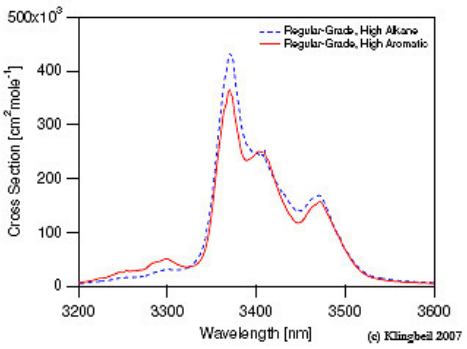

Figure 2.9: Absorption spectrum of standard gasoline

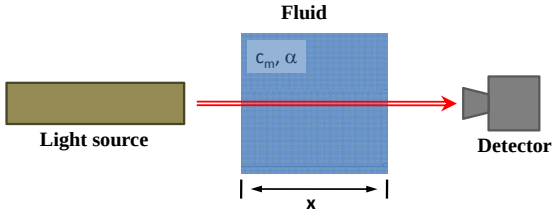

Figure 2.10: Schematic line-of-sight measurement

The Infrared Extinction Method is based on the ability of molecules to absorb energy through transition between its vibrational or rotational levels. It is important to mention, that this is a simple conversion of radiation energy into kinetic energy (thus heat) without any emission of radiation like for fluorescence techniques[3]. In case of hydrocarbons, a strong absorption band can be found in the infrared regime at 3.39[μm] (2945 cm^{-1}) [32, 33]. Figure 2.9 gives an example of the absorption spectrum for standard gasoline. Hence a 3.39[μm] monochromatic laser beam will experience a significant loss of intensity in gasoline vapor while an other beam of different wavelength will be affected very little or not at all. The energy transmitted through

[3]In a typical application of the IRE low energy lasers are employed and the time that a molecule is exposed to radiation is kept very short. For these reasons the heating of the medium can be neglected, allowing to regard this technique as non-intrusive

a medium having a constant vapor concentration c_m follows the Beer-Bouguer-Lambert law [4]:

$$\frac{\overline{I}_{(x)}}{I_0} = e^{-\overbrace{\int_0^l \alpha_{(\lambda,p,T)} \cdot c_{m(x)} \cdot dx}^{K_{vapor}}} \tag{2.26}$$

Knowing the length of the crossed area x and the specific absorption coefficient for the ambient conditions (λ, p, T), the concentration c_m is easily determined. It has to be mentioned, that this value for K_{vapor} is an integral over the full line of sight (see figure2.10). To achieve point results, deconvolution procedures have to be applied. Additionally, equation 2.26 is only valid in a homogeneous one-phase environment.When applied to a multi-phase flow the right hand side of the equation has to be replaced by several coefficients, taking into consideration the number of phases [11]:

$$\frac{\bar{I}_{(x)}}{I_0} = exp\left[-K_{drop-scat}\right] \cdot exp\left[-K_{drop-abs}\right] \cdot exp\left[-K_{vapor}\right] \tag{2.27}$$

The terms for extinction by droplet scattering and droplet absorption can be expressed as:

$$K_{drop-scat} = \overline{C_n} \cdot l \cdot \frac{\pi}{4} \int_0^\infty Q_{sca} \cdot D^2 \cdot \overline{N(D)} \cdot dD \tag{2.28}$$

and

$$K_{drop-abs} = \overline{C_n} \cdot l \cdot \frac{\pi}{4} \int_0^\infty Q_{abs} \cdot D^2 \cdot \overline{N(D)} \cdot dD \tag{2.29}$$

where $\overline{C_n}$ is the line-of-sight averaged number density, $\overline{N(D)}$ the drop diameter distribution and Q_{sca} and Q_{abs} are the scattering and absorption efficiencies, respectively. If we substitute the extinction coefficients in equation 2.27 by their definitions given in equation 2.26, 2.28 and 2.29, we obtain the full radiative transport equation for an absorbing wavelength λ_{abs}:

$$\begin{aligned}\left(\frac{\overline{I}_{(x)}}{I_0}\right)_{\lambda_{abs}} = & \; exp\left[-\overline{C_n} \cdot l \cdot \frac{\pi}{4} \int_0^\infty Q_{sca} \cdot D^2 \cdot \overline{N(D)} \cdot dD\right] \\ & \cdot exp\left[-\overline{C_n} \cdot l \cdot \frac{\pi}{4} \int_0^\infty Q_{abs} \cdot D^2 \cdot \overline{N(D)} \cdot dD\right] \\ & \cdot exp\left[-\int_0^l \alpha_{(\lambda,p,T)} \cdot c_{m(x)} \cdot dx\right]\end{aligned} \tag{2.30}$$

Consequently, the determination of the vapor concentration $c_{m(x)}$ (or, after integration, of its integral value $\overline{c_m}$) requires knowledge of the drop diameter distribution $\overline{N(D)}$, the two extinction

[4] The theoretical limits to this assumption as mentioned, for example, by Swanson et al. [34] have been found to be negligible for the present configuration.

efficiencies Q_{sca} and Q_{abs} and the line-of-sight averaged number density $\overline{C_n}$. The first one can be measured by the use of a laser diffraction technique. The extinction efficiencies are determined by Mie-theory computations, knowing the wavelength dependent refractive index of the drops from literature. The number density may be obtained with an extinction measurement at a non-absorbing wavelength, λ_{na} since it is wavelength-independent and for that case scattering by the drops is the only mode of extinction:

$$\left(\frac{\overline{I}}{I_0}\right)_{\lambda_{na}} = exp\left[-\overline{C_n}\cdot l\cdot\frac{\pi}{4}\int_0^\infty Q_{sca}\cdot D^2\cdot\overline{N(D)}\cdot dD\right] \tag{2.31}$$

As a conclusion we can note, that for determination of the vapor concentration by the IRE following points have to be fulfilled:

- Knowledge of the wavelength-dependent refractive index
- Mie-theory computations for both wavelengths
- A laser diffraction measurement to determine the averaged size distribution
- Two extinction measurements, one at an absorbing, one at an non-absorbing wavelength

This represents a lot of experimental and numerical effort for just one measurement and would render the IRE practically impossible to use for daily research or for industrial application. However, this is the theory for the basic principle of this technique. The next chapter describes the development and refinement of these basics from their discovery to the present day. Anticipating one of the major advancements it can be told, that a way was found to significantly facilitate IRE measurements.

2.3.2 Development of the IRE

Until the recent state of the art, Infrared absorption/extinction techniques have followed a development for more than thirty years. In this timespan an evolution from intrusive probing in soot-laden environments [5] to tunable diode lasers [35] and to new fields like microbiology [14] has taken place. This chapter gives an overview of this evolutionary process. To highlight important steps in development, three phases have been specified: pioneer, evolutionary and applicative phase. For each of the three, key works will be described in detail.

Pioneer phase

The first phase in the development includes publications from the years 1979-1984. It is characterized by works, which discover the potential of infrared to deliver additional information to conventional measurement techniques in a wide range of applications.

M.S.A.Skinner in 1979, is the first one known to the author of this thesis, to employ infra red analysers for concentration measurements [5]. He develops a gas analysis system for coal-fired boiler plants, designed to prevent spontaneous combustion in the coal beds. The **main achievement** of this project is the confirmation that infrared devices are able to do continuous measurement of CO concentration, under industrial conditions. However, there are still strong **differences to our requirements**: The system of Skinner is based on samples, taken by a mechanical probe from the area to be controlled. These samples are filtered,cleaned and dried before passing the detectors. Therefore it is intrusive, non-in situ, averaged over the sample volume and not suitable for multiphase flows.

P.C.Ariessohn et al. propose in 1980 the use of a two-wavelength laser transmissiometer for non-intrusive, in-situ measurement of the size and concentration of coal ash droplets [6]. The idea to employ two lasers of different wavelength is based on the following idea:
The fractional transmittance of a monochromatic beam of light traversing a dispersion of particles of various sizes may be written as

$$Tr = exp^{-\frac{3}{2}\frac{\bar{Q}\cdot C_v\cdot l}{D_{32}}} \tag{2.32}$$

When measuring the transmittance at two wavelengths one may form the ratio $\frac{ln(Tr_{\lambda 2})}{ln(Tr_{\lambda 1})} = \frac{\bar{Q}_2}{\bar{Q}_1}$. For particles with no absorption, the variation of this ratio with D_{32} exhibits a smooth monotonic behaviour for $\lambda_1/3 \leq D_{32} \leq \lambda_2$. Therefore, the determination of the Sauter mean diameter, independent of the concentration, is possible by the transmittance measurements at two wavelengths as long as these bracket D_{32}. Expecting particles between one and three micrometers and following this condition, a He-Cd laser with $\lambda_1 = 325[nm]$ and a He-Ne laser with $\lambda_2 = 3.39[\mu m]$ are chosen.
The **results** of this experiment prove in a convincing fashion that the use of multiple wavelengths permits to obtain loading and the Sauter mean diameter of a particle flow, in-situ and non-intrusively, by simple transmission measurements. Unfortunately, these advances come along with several **inconveniences**: The investigation is done on solid particles without evaporation and absorption of the laser beams. Additionally, since every influence of the surrounding plasma is eliminated during the calibration, a de facto one-phase flow is created. The biggest setback for this approach is the costly calculation of the mean extinction efficiency $\bar{Q}$. To obtain this parameter, not only a size distribution function has to be known but also elaborate Mie scattering theory calculations have to be performed. This relativizes the 'in-situ' characteristic of the obtained results.

A.R.Chraplyvy takes the step to introduce the two wavelength absorption/scattering technique to sprays in 1981 [7]. The goal is to determine the local, time-averaged vapor concentration of a n-heptane spray despite the influence of scattering on the liquid phase. His theoretical considerations lead to an expression similar to equation 2.30. As light sources, two HeNe lasers with wavelengths of 632.8 and 3390 $[nm]$ respectively are chosen. Their beams are superposed by the aid of a beam splitter to allow simultaneous attenuation and scattering measurements. Furthermore, an adaptation of the 'Onion Peeling' deconvolution scheme (details see chapter 5.3.1) to extract the local concentration values from the line-of-sight measurements is presented.

The **main advancements** of this work are: The application of infrared absorption to a two-phase flow, measuring a gas-phase characteristic; the development of a theoretical model how to distinct the attenuation of the vapor from that of the liquid phase; and the introduction of a deconvolution scheme to obtain spatially resolved concentration values from the integral measurement results.
However, there still are some **points to develop further**: Since the whole course of experimental and numerical steps as described at the end of chapter 2.3.1 has to be completed, no effective in-situ measurement is possible. Due to the employed spray analyzer for scattering measurements the spray density had to be kept moderate. Therefore no information of the feasibility of this technique for dense sprays is available. Neither is an error estimation of the process given. A preceding paper to this topic has been published one year earlier by a J.M. Tishkoff as a member of Chraplyvy's research group [36], but will not be considered here due to its lack of detail.

One more publication, which acts as a bridge between this and the next phase of development and shall be therefore briefly mentioned, are the experiments of **Tsuboi et al.** in 1984 [32]. Recognizing the lack of values for the wavelength-dependent absorption coefficient in literature, Tsuboi et al. performed a wide series of shock-tube experiments to determine the influence of temperature on this parameter. Using an infrared laser with 3.392[μ_m] wavelength, they obtain the progression of the decadic absorption coefficient for methane, ethane, propane, n-pentane/hexan/heptan/octan/nonan, iso-octan, methanol, ethanol, butanol, acetone and benzene in a range from 298 to 1100[K] with an overall error range of less than 20%. These results are the basis for many investigations on infrared-extinction in the years to come.

Evolutionary phase

After these first experiments using the - up to this point - new technique of infrared extinction a sudden decline in publication on this theme can be observed. The interest to discover the full possibilities and also the limitations of this approach arises anew in the years 1990-1995, when the two research teams of Adachi et al. in Japan and of Drallmeier et al. in the United States publish a series of experiments which result in significant ameliorations to the IRE. This period, completely dominated by the mentioned authors, can be described as the 'evolutionary' phase of the IRE.

Adachi et al. With the goal to further evolve the technique as presented by A.R.Chraplyvy, M.Adachi et al. present their developments to the IRE technique, named IRES (infrared extinction and scattering) in 1990 [8]. This method consists in using a broadband light source instead of the monochromatic laser beam. Single wavelengths can be separated by narrow band-pass filters as employed earlier in investigations by Cashdollar et al.[37]. But this time the idea behind these modifications to the setup is to avoid the costly Mie-calculation by a 'windowing' approach: Using three narrow filters, one at the main absorption wavelength (3.5 [μm]) and two others at neighbouring non-absorbing wavelengths (3 and 4 [μm] respectively), it is possible to distinguish between vapor and liquid extinction using the following two hypothesises:

- Liquid absorption is negligible. Therefore all the extinction at the non-absorbing wavelengths is due to scattering.

- The scattering amount at 3.5 [μm] can be calculated as the mean value of the transmittances at the other two wavelengths

This way, the part of extinction at the main wavelength due to scattering is known and the vapor concentration can be deducted following Beer-Lambert's law. In this way experiments are carried out for a methanol spray in reacting and non-reacting conditions.
The assumptions above are discussed in an extensive error analysis of this technique. Using several created drop distributions and calibrated absorption coefficients, classical Mie-calculations are performed to compare these high-precision results to the ones obtained using the windowing approach. Considering errors due to the assumptions taken, calibration faults and beam steering due to change of the refraction index the overall error is estimated by 7% for the non-reacting spray and 12% for the reacting spray. However, for very fine particles, liquid absorption was found to be not negligible anymore. For this case, Mie calculations rest mandatory.
The only setback of this approach is the fact that the three wavelengths cannot be analyzed at the same time in the present setup. Therefore, the measurements cannot be considered in-situ and are only practical for stable spray conditions.

Drallmeier et al. are possibly the team who did the most excessive research on the IRE known to the author. In a series of publications between 1990 and 1994 they systematically investigate and ameliorate the technique [9, 10, 11, 38, 39, 40]. Since iso-octane is widely used as mono-composant surrogate for gasoline, it becomes their experimental liquid of choice.
Therefore, as first step the detailed definition of the optical constants at 3.39[μm] for this hydrocarbon is done [9]. A liquid sample cell sealed by a fused quartz prism is subjected to the incident laser radiation. This design suppresses evaporation and prevents index gradients above the liquid surface. With this setup, the evolutions of the real ($'n'$) and the imaginary part ($'\kappa'$) of the refractive index, determining refraction (n) and absorption (κ) of a species, over a temperature range from 296 to 353[K] are measured. The results show, that n remains relatively constant over the investigated temperature range while κ increases by approximately 20%. An error analysis numbers the total errors with 0.05% for n and 3.0% for κ.
Equipped with these reliable values for the extinction coefficients Drallmeier and Peters perform experiments similar to those of Chraplyvy on an evaporating iso-octane spray [10]. Combining the IRE measurements with a PDPA analysis of the vapor phase velocity, results for mean drop size and distribution, optical thickness, vapor concentration and vapor mass flux are acquired. The overall error for the concentration measurements is reduced to under 15% over the spray radius. However, these results are obtained by the classical method, meaning separate scattering measurements and Mie-calculations. Therefore the only progress to earlier works can be found in the slight diminution of the overall error and the determination of the vapor flux.
The third publication in 1994 is, in the author's opinion, the most influential one on the daily-basis applicability of the IRE [11]. Knowing, that the need for costly Mie-calculations is the biggest obstacle for a wider use of the extinction techniques, Drallmeier presents a simplification to the IRE evaluation process.

As shown in equations 2.26 to 2.31, the components of intensity attenuation vary with the employed wavelength. Drallmeier expresses the terms due to the liquid scattering and absorption in terms of optical thicknesses [5], using the indices $'3.39'$ for the absorbing and $'632.8'$ for the non-absorbing wavelength :

$$\begin{aligned} \tau_{drop,3.39} &= \overline{C_n} \cdot l \cdot \frac{\pi}{4} \int_0^\infty Q_{ext} \cdot D^2 \cdot \overline{N(D)} \cdot dD \qquad (2.33) \\ &\text{with} \\ Q_{ext} &= Q_{sca} + Q_{abs} \\ &\text{and} \\ \tau_{drop,632.8} &= \overline{C_n} \cdot l \cdot \frac{\pi}{4} \int_0^\infty Q_{sca} \cdot D^2 \cdot \overline{N(D)} \cdot dD \qquad (2.34) \end{aligned}$$

If the expression at equation 2.33 is substituted into equation 2.30, the following expression for the line-of-sight averaged vapor concentration results:

$$\overline{c_m} = \frac{1}{\alpha \cdot l} \left[-\tau_{drop,3.39} - \ln \left(\frac{I}{I_{0\,3.39}} \right) \right] \qquad (2.35)$$

Introducing the drop optical thickness at the non-absorbing visible wavelength gives us

$$\begin{aligned} \overline{c_m} &= \frac{1}{\alpha \cdot l} \left[-\tau_{drop,632.8} \left(\frac{\tau_{drop,3.39}}{\tau_{drop,632.8}} \right) - \ln \left(\frac{I}{I_{0\,3.39}} \right) \right] \\ &= \frac{1}{\alpha \cdot l} \left[-\tau_{drop,632.8} \cdot R - \ln \left(\frac{I}{I_{0\,3.39}} \right) \right] \qquad (2.36) \end{aligned}$$

Note, that the only term in this equation that depends on the size distribution of drops is the optical thickness ratio $'R'$

$$R = \frac{\int_0^\infty (Q_{ext})_{3.39} \cdot D^2 \cdot \overline{N(D)} \cdot dD}{\int_0^\infty (Q_{ext})_{632.8} \cdot D^2 \cdot \overline{N(D)} \cdot dD} = \frac{\tau_{drop,3.39}}{\tau_{drop,632.8}} \qquad (2.37)$$

Therefore a determination of the vapor mole fraction could be done by two simple absorption measurements at the two wavelengths if $R \to 1$.
Following this theory, Drallmeier determines the limit of the drop size for which this approximation is valid by a Mie scattering code for drop sizes between 1 and 200 $[\mu m]$. Figure 2.11 shows the variation of R for varying refractive indices (real and imaginary parts) and for significantly different log-normal size distributions.

[5] From a mathematical point of view, the 'optical thickness' of an medium represents the probability, that an entering photon reaches the detector on the opposite side. Therefore, the lower the probability, the 'higher' the optical thickness.

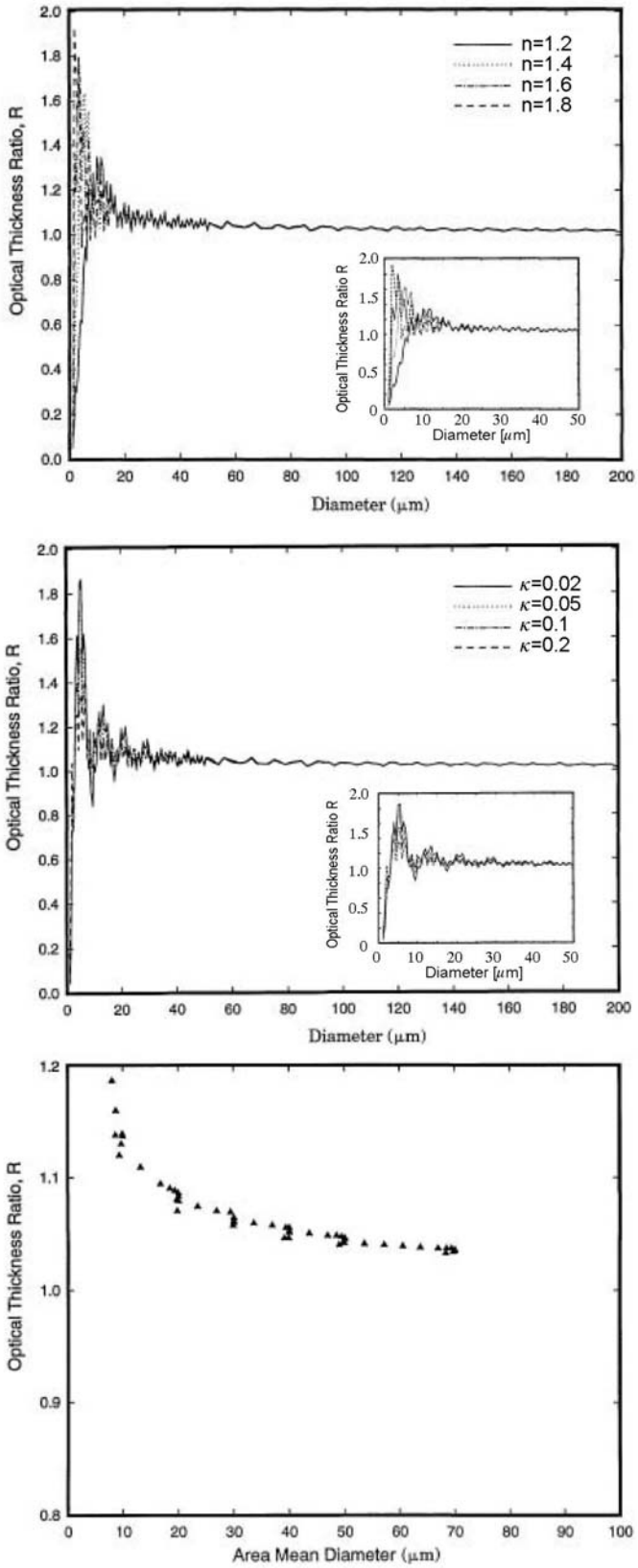

Figure 2.11: Variation in the optical thickness ratio R. Top: for various values of n at κ=0.067; Center: for various values of κ at n=1.44; Bottom: for different log-normal size distributions (Source: [11])

We see, that after heavy oscillations of R for very small droplets, soon a value of ≈ 1.1 is reached at all diagrams. By correlating this ratio with an area mean diameter (amd) given by

$$amd = \left[\frac{\sum N(D) \cdot D^2 \cdot dD}{\sum N(D) \cdot dD}\right]^{1/2} \tag{2.38}$$

a cutoff near $20[\mu m]$ can be set as lower limit for the approximation of R=1, tolerating an error of 10%.
Concluding, this work of Drallmeier showed, that for sprays with an area mean diameter greater than $20[\mu m]$ the infrared drop optical thickness can be approximated by the visible drop optical thickness. As a result, no more separate scattering measurements or Mie calculations are required to determine the line-of-sight vapor mole fraction. This reduces the IRE to two extinction measurements at the employed wavelengths and presents the basis for real-time analysis of sprays with this technique.
Later works of Drallmeier et al. confirm this approach by applying the simplified IRE to various configurations including pressure swirl atomizers [38], calibration sprays consisting of styrene beads [38, 39] and pulsed fuel sprays [39, 40, 41]. Without going into the details of all the publications, it can be said, that for all these applications, good results for fuel vapor concentration and vapor flux are obtained with an overall estimated error of less than 10%. However, Drallmeier et al. state, that these results are obtained for sprays attenuating the visible wavelength less than 40% only! No validations for denser sprays have been made and no specifications concerning the polarization of the laser light are given.

Applicative Phase

The transition to the latest phase in development is hard to distinguish but can be dated , with some exceptions to the year 1996. After the important theoretical advancements of the previous phase, which answered most of the questions on the IRE, the interest shifts to new fields of applications and to more powerful devices for this technique. In terms of fields of application, the IRE is employed in combustive environment [35, 42], LPP test rigs [43, 44], scramjet combustors [13] and even for the detection of aerosols [14]. New devices include the introduction of optical fibers [12, 45, 33], tunable diode lasers [46, 35, 47] or the change of the measurement wavelength until UV[35, 48] .
A great number of applications concerns the employment of the IRE inside piston engines. Representatively, the work of Tomita et al. is introduced. the experiments of Gurton et al., however are highlighted for their unusual choice of the field of application.

E.Tomita et al. apply the IRE technique to a four-stroke spark-ignition piston engine to measure fuel concentration in the vicinity of the spark plugs. The difference to similar works is the way, optical access into the engine is achieved. While earlier experiments used one-cylinder engines especially constructed for optical measurements [49, 50] or at least modified the piston [12], Tomita et al. develop an optical sensor installed in a dummy spark plug. This ultra-compact device is coupled to light source and detector by optical fibers and can be installed into a conventional engine. The first experiments are performed with iso-octane as fuel at near

idling conditions of the engine. Since total evaporation in the vicinity of the spark plugs is expected, only infrared light is recorded at each crank angle. Results show good quantitative behaviour but with a large standard deviation. As possible error sources the presence of liquid droplets, the existence of other absorbing gases and mechanical vibration are investigated. To detect an eventual droplet presence, the optical sensor is modified to visible wavelength and the experiment is repeated. Considering other absorbing gases, the HITRAN database [51] is consulted, verifying the absorption spectra of combustion by-products. These two influences are found to be of negligible magnitude and are therefore discarded. However, a vibration analysis shows an influence of $\approx \pm 7\%$ on the absorption signal. This effect and possible absorption by engine oil vapor are noted as the main error sources for this technique.
As a summary, this work proves the ability of infrared extinction to be employed under realistic conditions. Error sources can be restricted to ambient influences. An unsatisfying point of this setup is the fact that only a zone of practically one phase flow is investigated. A development of the optical probe to process two wavelengths simultaneously would allow the investigation of a less restricted zone.

P.Gurton et al. leave the field of mechanical engineering to employ a variant of the infrared extinction measurements to detect aerosols [14]. The intention of their work is to establish a more reliable set of optical cross sections for a variety of chemical and biological aerosol simulants with the aid of a photo-acoustic system. Their test rig consists of an aerosol chamber and a photo-acoustic measurement cavity equipped with optical access for a tunable CO_2 laser and a highly sensitive microphone. These double configuration is based on the following principle: When laser irradiation is passed through a volume containing aerosols, a part of the light will be absorbed, heating these particles. This heating subsequently results in a pressure rise within the volume. If the laser is now modulated at a known frequency, a pressure wave will result at the same modulation and can be captured by the microphone. Since the power of the acoustic signal is directly proportional to the optical absorption cross section of the particles - independent of the particle shape, the terms for extinction by absorption and extinction by scattering can be separated from the overall extinction of the laser beam.
Gurton et al. performed these experiments for silicone oil droplets, bacillus atrophaeus endospores and kaolin clay, representing chemical, biological and natural background aerosols. The photo-acoustic results for absorption and extinction are compared to those obtained by Fourier transformed infrared (FTIR) measurements conducted earlier on the same setup [52] and to classical Mie-calculations using optical refraction indices found in the literature. Without going into detail it can be said, that for all three classes of aerosol the values for extinction are in good accordance to the FTIR results. The MIE-calculations however, differ strongly for extinction as well for absorption from the experiments. The authors explain these difference by the use of non-ideal optical constants in the calculations and the fact, that these prediction methods assume spherical shape of the particles. This hypothesis is prone to error when the particle size approaches to optical wavelength, which is the case for some of the aerosols tested. Concluding this approach, it can be said that, although this technique evolved in a completely different direction as the classic two-wavelength IRE, it proves the versatility of absorption measurements. The detection limit of 0.001 $kmol^{-1}$ - at in-situ measurements - emphasises the sensitivity that can be achieved by quite simple means.

2.3.3 Conclusion

During the last thirty years of investigation and refinement, the infrared extinction technique has considerably matured in terms of applicability and sensitivity. A repartition of this development into three phases describes the change from an intrusive, soot concentration-measuring technology to miniaturized, non-intrusive measurement of droplet number density, vapor concentration and vapor flux. Especially the simplification found by Drallmeier et al., which renders additional scattering measurements and Mie calculations obsolete, helped to create the characteristics we can associate with this technique today: robust, simple, compact and cost effective.
However, in spite of all the research done, still some aspects exist that limit the usability of the IRE:

1. The IRE still is a point-result, line-of-sight principle that requires extensive measurement runs to scan a given field of interest
2. No investigations to the behaviour of the IRE in the vicinity of strong concentration gradients at phase interfaces, which were identified to be LIF's Achilles heel in chapter 2.2.3, are known to the author. The only mentioning of concentration gradients is due to the error caused by the subsequent beam-steering [8, 38] or when taking boundary layers at the limits of the flow into account [53]. However, these gradients are small compared to a liquid-gas interface.
3. Nearly each detailed publication on the IRE compares the results to calculations or data from scattering measurements. But what is missing in the opinion of the author, is a comparison to other optical measurement techniques which could be used rather complementary than as a replacement. Especially a confrontation to PLIF could be of interest, since the two techniques seem to cover each other's weak spots.

Point one can be solved rather easily by employing high-power infrared lasers which feed an largely expanded beam. Together with a suitable sensor array this setup would allow to take 'negative images' of a region of interest. However, since compactness and low cost are two of the main arguments to use the IRE, such an application should be questioned for its benefits.
Aspect two and three seem to be manageable if the experimental setup is carefully chosen and appropriate fluorescence data is available. Therefore these points were chosen to be investigated in this thesis.

2.4 Choice of the experimental configuration

Having defined our points of interest in an investigation of the IRE, the next step is to decide on an experimental configuration which allows to study these effects. As a reminder, the necessary characteristics are summarized below:

- Presence of zones of strong concentration gradients to study the IRE behaviour
- Presence of zones of smooth concentration gradients for comparison purposes to LIF

- Fluorescence data available for at least a part of the configuration
- Adaptability of the governing parameters
- Stability, to allow a greater number of measurements under identical conditions
- Simple enough to be modeled and simulated without heavy computational cost

In the literature three basic types of configurations can be found to validate optical measurement techniques: Confined volumes [9, 54, 4], droplets equally spaced along a geometrical axis [3, 2, 15, 25] and controlled sprays [39, 40]. Table 2.1 compares these configurations to the characteristics determined above. An evaluation system ranging from ++ (very good) to - - (unsatisfying) is used to express strengths and weaknesses of every option:

	Gradients		Adaptability	Stability	LIF data	Simplicity
	strong	smooth				
Volume	- -	- -	+	++	++	++
Droplets	++	++	+	++	++	+
Spray	-	+	+	-	+	- -

Table 2.1: Comparison of experimental environments

We see that the **Confined volume** has its strong points in stability, simplicity and the availability of comparative LIF data. Although changes in fluid, concentration, temperature and pressure can be achieved very fast, adaptability is not rated at the highest possible grade due to the global nature of all these parameters over the entire volume. The only, but severe weakness of this configuration is the complete absence of concentration gradients (neglecting possible film condensation at the walls). Therefore, the confined volume is not suitable as an environment for our comparative investigations. It presents, however, a perfect tool for calibration purposes. For this reason a system of this kind is used for first tests on our experimental setup under ambient conditions (chapter 4.3.3) and more sophisticated version has been designed for determination of the absorption coefficient for elevated levels of pressure and temperature (Annex A).

The **Controlled spray configuration** represents the test option closest to reality. Usually, the only difference to sprays used in industrial engines is the placement of the injector in a laboratory setup (optical accesses or unconfined spray, vibration isolations, etc.) and the use of monocomposant liquids or particle emulsion as surrogate fuels. Thanks to the mentioned laboratory setup and the well defined surrogate fuels, the adaptability of these systems is satisfying. Concentration gradients are naturally present, but for a line-of-sight integrated technique as the IRE they will appear smooth due to the averaging effect over the length of the beam path. An exception to this behaviour are pulsed sprays with a frequency low enough to allow phase-locked investigation. This solution, however, may interfere with the requirement of stability, since a total uniformity of the pulses can not be guaranteed. Additionally, pulsing the spray makes an already inconvenient point of this choice even worse: the complexity of simulation. Modeling a spray with all its physical effects like atomization, coagulation, evaporation or entrainment of air is the subject of many works today. Even without considering pulsation this effort would

exceed the limits of this thesis. Therefore, using a controlled spray configuration is excluded.

Equally distributed droplets as test environment fulfill all of the requirements to our investigation. If they are aligned along one geometrical axis, we speak of a droplet stream. When using an evaporation liquid, a composition like this includes strong concentration gradients between liquid and gaseous phase and smooth gradients inside the vapor. Harmonizing the droplets in diameter, temperature, velocity and spacing guarantees excellent stability. The adaptability of these parameters is defined by the physical limits of the injector only. Considering the simulation, the computational cost can significantly be reduced by exploiting the axisymmetry of this configuration. The modeling effort is higher than for the confined volume, but still reasonable. And finally, thanks to all these characteristics, this configuration has already been intensively studied in the past, leading, among other things, to detailed comparative LIF data [23, 2, 3, 15, 4]. As a consequence, a stream of harmonized droplets is chosen for this thesis also. Details to the creation and characteristics of the employed droplets can be found in chapter 4.2.3.

As experimental liquid of choice acetone (chemically exact: Propanon C_2H_5OH) is selected. This monocomposant hydrocarbon represents one of the classic experimental fluids for optical measurements. Its low boiling point and density, 359.15 K and 0.79 g/cm^3 at ambient conditions respectively, allow easy evaporation at room temperature. As most of the hydrocarbons, it possesses a strong absorption band in the infrared region around 3.4 μm. An additional advantage poses its good solubility in water and organic solvents. This ability, together with its fluorescence in a visible wavelength when excited, have made it a widely used seeding liquid in (P)LIF experiments. Low toxicity further simplifies the handling. Therefore lots of experimental data for acetone can be found in the literature [23, 2, 4, 55, 8, 56].
Characteristics of acetone that demand caution, however, are its high flammability and the ability of higher concentrations of acetone vapor to create an explosive mixture in air. But thanks to its high volatility a standard ventilation system is sufficient to keep vapor concentrations at a safe level.

Chapter 3

Simulation of the absorption process

3.1 Reasons for simulation

Since no practical experience on the IRE has been obtained in this department yet, the decision to create a simplified numerical simulation of the absorption process parallel to the development of the experimental bench was made. The goal is to support every step of the experiments with numerical predictions or comparative data:

- Even before adapting the test bench to the droplet stream configuration, the amount of absorption that can be expected from a single droplet can be modeled. This information is crucial to determine the maximal acceptable noise level of the setup.

- During the experimental runs simultaneous simulations of the actual configuration give an indication to possible calibration or measurement error. Additionally, the search for optimal experimental parameters can be accelerated by shifting the governing parameters.

- Finally, after conclusion of the measurements, the differences between simulation and experiments can be used, to correct the numeric model and to develop it into a tool of prediction, liberating the experimental rig for new duties.

In this work, mainly the first two points are of importance. The last one is desirable but will be left to successive investigations on this topic.
The most important choice before building the simulations is the one of the droplet evaporation model. Droplet evaporation controls the vapor concentration around the liquid phase and, consequently, the absorption measured. Therefore the choice of an unfitting model to predict the resulting vapor field will render any comparisons to experimental results impossible.

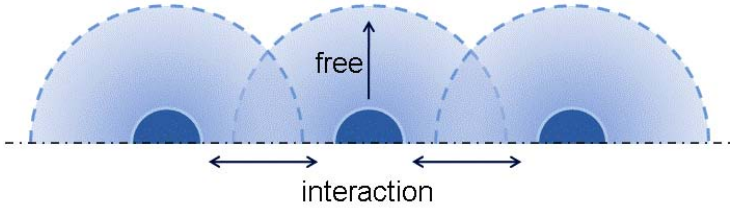

Figure 3.1: Schematic interaction of the vapor fields for aligned droplets

3.2 Choice of the evaporation model

The configuration of an evaporating monodisperse droplet stream can be regarded as radial symmetric around one axis. However, as shown in figure 3.1, spherical symmetry around a droplet can not be supposed due to the interaction with its predecessor and successor. This interaction leads to a non-uniform distribution of the vapor concentration with a much lower decrease in concentration between the droplets than perpendicular to the line of propagation. Because of this effect and the displacement of the droplets with its resulting entrainment of air, a vapor 'tunnel' is formed around the droplet stream.
All these effects make it impossible to use an analytical model to describe the complete vapor distribution around the droplets. Recently at ONERA, B.Frackowiak developed a direct numerical simulation for droplets in interaction [15, 4, 57]. Verified by PLIF measurements, his results on a stream of monodisperse droplets represent our first choice to obtain the required vapor field for the absorption simulation:

3.2.1 DNS computed vapor field by Frackowiak

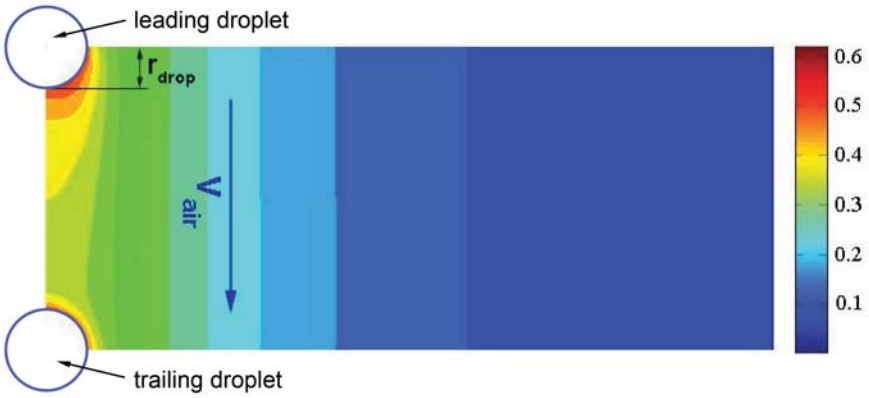

Figure 3.2: Center plane of the vapor mass fraction field for a droplet stream of 238 μm at $T_{drop} = 318.75K$ and $S_D = 3.76$ as calculated by DNS

The approach of B.Frackowiak simulates the droplet stream by two static droplets - reduced to a quarter disc each due to symmetry - placed in an air current which flows parallel to the rotational axis. It consists of a Navier-Stokes solver for the liquid phase two-way-coupled to a

FLUENT simulation of the surrounding air current.
The physical effects taken into account include the Stefan flow, causing a widening of the boundary layer around the droplet and the influence of the Marangoni effect on the temperature distribution of the droplet originally calculated by a Hill-Vortex model.
Since a detailed description of the liquid-phase model in this context would be too elaborate, only the main assumptions taken shall be mentioned[1]:

Main hypotheses of the liquid phase model:

1. Incompressible liquid → constant liquid density
2. Droplets rest spherical in the flow (low Weber numbers)
3. Thermodynamic equilibrium at the droplet interface
4. No gas is soluted in the liquid phase
5. Radiative transfers between droplet and environment are neglected
6. The gas phase is quasi-stationary → immediate adaptation of heat and mass flux to local boundary conditions at each instant.
7. The diminution of the diameter due to evaporation is neglected

The resulting vapor mass fraction distribution as presented in figure 3.2 shows the expected non-uniformity around the droplets. This difference can be highlighted by extracting linear profiles from this field. Figure 3.3 compares a profile taken between two droplets along the axis (red) to one in perpendicular direction (blue). The exact positions of the profiles are given in the insert:

The differences in concentration level and shape are clearly visible. While the two profiles start at the same concentration level the horizontal/radial one decreases steadily, nearly adopting a negative exponential shape, whereas the vertical/axial one rests at high concentrations. Only the influence of the air flow, creating a wake after the leading droplet and compressing the vapor at the leading edge of the trailing one, keeps it from forming an 'U'-shape at a mass fraction level between 0.6 and 0.42.
The results for the radial profiles are validated through PLIF measurements performed by the same author for two droplet stream configurations. The initial parameters of these two cases are given in table 3.1.

	D_{drop}	T_{drop}	T_∞	v_{drop}	p_∞	$Y_{1,s}$
Case I	238 μm	45.6 $°C$	23.5 $°C$	8.3 m/s	994 $mbar$	0.822
Case II	173 μm	22.4 $°C$	22.4 $°C$	7.87 m/s	999 $mbar$	0.43

Table 3.1: Parameters of the two DNS configurations

[1]For the complete list of hypotheses, including those that are merely of numerical signification, please refer to the thesis of B.Frackowiak [15]

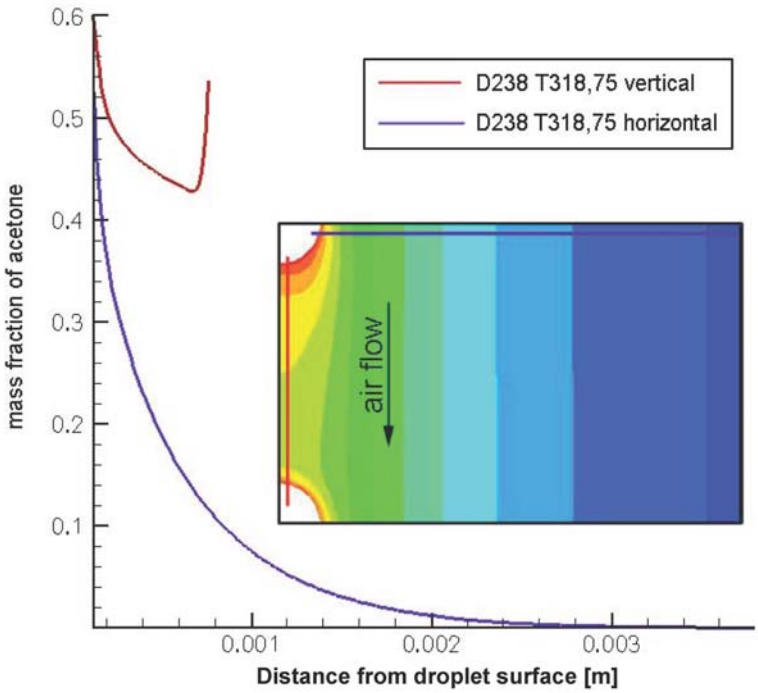

Figure 3.3: Horizontal and vertical mass fraction profiles for a droplet stream of 238 μm at $T_{drop} = 318.75K$ and $S_D = 3.76$ at $t = 5ms$

Especially for the heated case I, a very good agreement between numerical and experimental data can be observed (figure 3.4). For the configuration of smaller droplets at ambient temperature the model predicts a slightly higher concentration level that can be found experimentally. The author explains this by numerical uncertainties at lower temperature gradients. Due to the problems of PLIF when dealing with strong concentration measurements, as mentioned in chapter 2.2.3, no comparative data for the axial profiles is available. However, regarding the high accuracy of the horizontal results, the model of B.Frackowiak can be regarded as a reference point for the extinction measurements to be performed.
Unluckily, this high level of detail in this model comes with very high computational costs. For this reason, the vapor fields only for the two cases mentioned above are available. While a comparison of the IRE to these configurations may be sufficient to validate the technique, it is not optimal to have such limitations.
Therefore, an analysis of the simplifying assumptions of this model is performed, to obtain an idea how this elaborate model can be approximated by simpler, more flexible approaches:

Looking at the list of hypotheses at the beginning of this chapter, we see, that most of the assumptions are recognizable as the ones taken for the classic 'isolated droplet' simulation by the D^2-law (chapter 2.1.1). The main differences between this standard configuration and the actual model are the presence of an air current around, the interaction between the droplets and the non-existence of spherical symmetry. The last point was already clearly observed looking at the differences between radial and axial vapor mass fraction profiles. However, a combination of two separate replacement models, one for each direction, may still be capable to emulate this

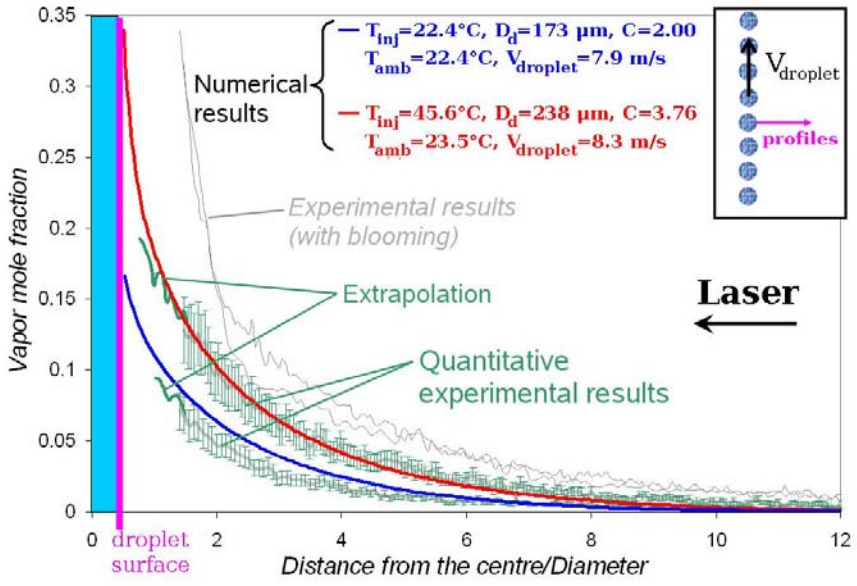

Figure 3.4: Experimental validation of the horizontal profile for two configurations. Source: [4]

behaviour.
Radial direction: Supposing the droplet stream was given enough time to fully develop the observed quasi-static vapor tunnel the influence of the air current on the radial vapor distribution can be regarded as small. The same can be said for the interaction between the droplets if the spacing is sufficiently large since there are no neighbouring droplets in radial direction. With these two additional assumptions the resemblance to the 'isolated droplet' model becomes very close. Therefore, the decision is taken, to attempt a simulation of the results in radial direction by the use of this approach.
Axial direction: Unlike to the situation in radial orientation, the influence of air current and interaction can not be neglected along the axis. This discards the use of the same model for this direction. However, when neglecting the wake of the leading droplet, an evaporation model developed by N.Doué and C.Laurent, taking the interaction between droplets into account, looks promising to deliver comparable results.
A short description of these replacement models as well as the comparison to the data from B.Frackowiak is given in the following chapters:

3.2.2 Comparison to the 'isolated droplet' model

The 'isolated droplet' model corresponds in its characteristics to the one described in chapter 2.1.1. The main assumption taken are:

- Spherical, monocomposant droplet
- No agitation of either liquid or surrounding gaseous phase

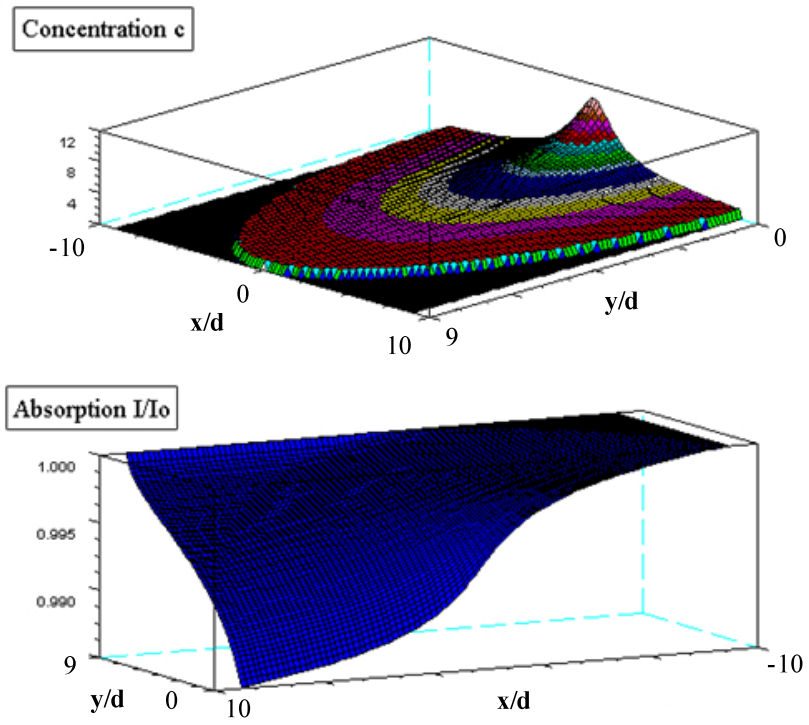

Figure 3.5: **Top**: Simulated vapor field: cut through the center plane; **Bottom**: Attenuation of incident energy by this field

- Constant temperature inside the vapor field
- Concentration on the droplet surface equals concentration under saturated conditions
- State of thermodynamic equilibrium already reached

Under these conditions, the problem becomes stationary and therefore independent of time. The resulting equation for the local mass fraction depends only on the radial position r and on the pressure and temperature at the droplet surface,which define the saturated mass fraction $Y_{1,s}$. With D_{drop} signifying the droplet diameter it can be expressed as below:

$$Y_{1,r} = 1 + (Y_{1,s} - 1) \cdot exp\left[\left(1 - \frac{D_{drop}}{2 \cdot r}\right) \cdot ln\left(1 + \frac{Y_{1,s}}{1 - Y_{1,s}}\right)\right] \tag{3.1}$$

Results for the vapor field calculated by this relation and the absorption by this distribution when interacting with an infinite laser beam at 3.39 μm are shown in figure 3.5.

The comparison of this model to the direct numeric simulation is done for both droplet stream configurations mentioned. For each case, the respective saturated vapor mass fraction was calculated using the local temperature at the droplet surface and the time given, as determined by B.Frackowiak.

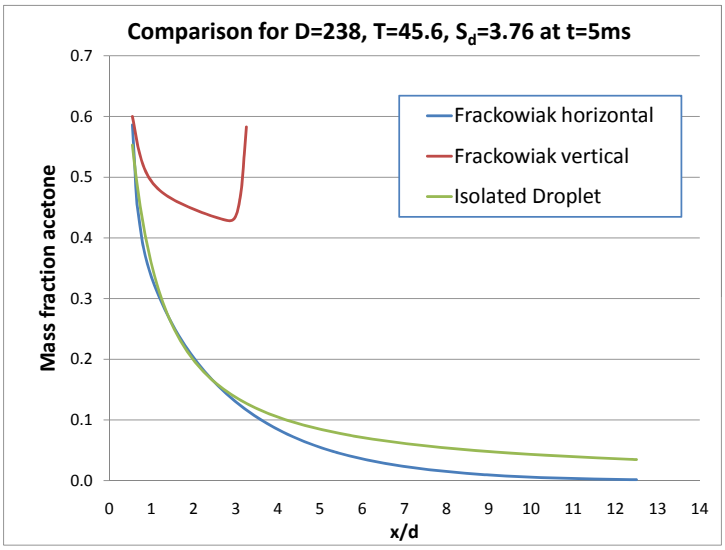

Figure 3.6: Comparison for a droplet at $D_{drop} = 238\mu m$, $T_{Drop} = 318.75K$, $T_\infty = 295.15K$, t= ms

As shown in figures 3.6 and 3.6, the two approaches show good agreement in the direct vicinity ($x/d < 1$) of the droplet.
For the case of the **heated droplets** with $D_{drop} = 238\mu m$ and $S_D = 3.76$ (figure 3.6) the differences remain small until $x/d \approx 3$. The slight overestimation of the D^2-model in the first part of this region ($1 < x/d < 2$) can be explained by the higher radial convection due to the Stefan flow in the DNS simulations. In the next section, at $2 < x/d < 3$, the exact opposite can be observed. A reason for this behaviour can be found in the interaction between the droplets which elevates the local concentration values in comparison to the isolated configuration. However, since the spacing in this case is relatively large compared to the diameter, this effect rests small in the present case. At radial distances greater than three droplet diameters the predicted concentrations are much higher for the isolated model than for the numerical simulations. This can be explained by the influence of the air flow which enhances the convectional vapor transport away from the droplet.
When looking at the comparison for the **droplets at ambient temperature**, with $D_{drop} = 173\mu m$ and $S_D = 2.0$ (figure 3.7), the behaviour at medium distances to the droplet ($x/d < 4.5$) is quite different. From the droplet surface until the limit of this region the 'isolated droplet' model constantly underestimates the vapor mass fraction. An explanation for this effect may be the combination of lower temperature and closer spacing than in the heated case. While the lower temperature gradient to the surrounding air diminishes the radial convection, the closer spacing renders interaction effects dominant. The latter effect is also visible when regarding the red axial profile. Already the level of concentration at the droplet surface is significantly higher than in radial direction. And different to the first case at wider spacing, nearly no wake effect can be observed since the vapor field from the succeeding droplet keeps already interferes upstream.

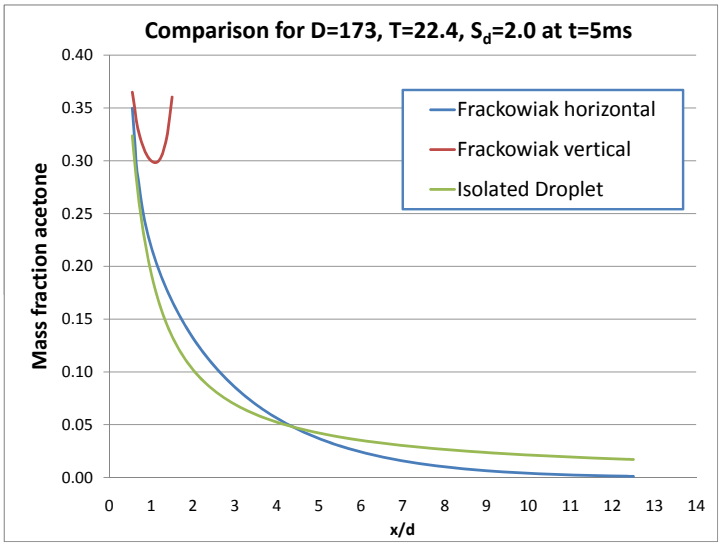

Figure 3.7: Comparison for a droplet at $D_{drop} = 173\mu m$, $T_{Drop} = 298.15K$, $T_\infty = 295.15K$, t= ms

3.2.3 Axisymmetric model with interaction

The evaporation model of N.Doué and C.Laurent was originally developed as a tool to study the evaporation of multicomposant droplets [58, 55]. The part adapted to our purposes is based on the principle of the Discrete Composant Model. Similarities of this concept to the 'isolated droplet' are found in the assumption of spherical symmetry of the whole system and the uniformity of the physical parameters in the liquid and in the vapor phase.
However, some important features distinguish it from the former model: First of all, the gas phase is regarded only as quasi-stationary. That means that all the transfer processes adapt themselves instantaneously to the new boundary conditions at each time step. This renders the whole model time-dependent, including the diminution of the droplet diameter, which is not neglected as in the other two models. Furthermore, the convective effect of the expansion of the boundary layer by the Stefan flow is taken into account and the temperature gradients in the droplet are calculated by a Hill-vortex model[2].
For the case of the monodisperse droplet stream, the interaction between the droplets is expressed by an additional coefficient in the diffusion term which depends on the velocity, temperature and droplet spacing. For the vapor mass fraction of a monocomposant droplet, μ at a given moment 't' and radius 'r' following expression can be written:

$$Y_{1,r} = 1 + (Y_{1,\infty} - 1) \cdot exp\left[-\frac{\dot{M}}{4\pi\rho_{drop}D_{drop}} \cdot \left(\frac{1}{r} - \frac{1}{R_{f,M}}\right)\right] \tag{3.2}$$

With $\dot{M}$ signifying the total mass flow, ρ_{drop} the droplet density and D_{drop} the droplet diameter. $R_{f,M}$ is the radius of the diffusion boundary layer and is defined as:

[2] a full list of the assumptions and features is given in [55]

$$Y_1 \left(r = R_{f,M} \right) = Y_{1,\infty} \tag{3.3}$$

This carefully chosen compromise between physical accuracy and small computational cost is the main advantage of the Discrete Composant model. It promises closer results to reality without sacrificing the possibility to investigate multiple configurations in a short time. However, the model still uses the hypothesis of spherical symmetry. The influence of this assumption on the vapor field has to be investigated, especially considering droplet interaction which will be regarded as uniform over the whole sphere.
Unfortunately, when comparing this model to the one from B.Frackowiak, total discrepancy of the results was observed. Closer investigations showed, that these are due to differences in the calculation of the physical properties. Since this represents the very basics of the model an adaptation to our need would be nearly equivalent to rewriting the model itself. Therefore the attempt to replace the calculation of the axial vapor concentration profile by this spherical symmetric approach was stopped.

3.2.4 Conclusion

A search for numerical evaporation models to be implemented in the absorption calculation was performed. Due to the non-uniformity of the vapor field around a stream of monodisperse droplets, this prediction can not be done by a simple analytic approach. A Direct Numerical Simulation on the same configuration, done by B.Frackowiak, was found to be sufficient exact to act as reference. However, due to its complexity only a very limited number of configurations is available. To avoid this constraint, an investigation to replace this simulation by multiple simpler and more flexible models has been done.
For the vapor concentration in radial direction, which is less affected by interaction, a comparison to the classic 'isolated droplet' model has been performed. Results show good accordance in the vicinity of the droplets but differ strongly at greater distances. Therefore this approach can not be used as an actual replacement. However, the differences at low and medium distances from the droplet are small enough to employ it for qualitative predictions on new configurations.
No simplified model was found to emulate the axial distribution, affected by co-flow and interaction between the droplets. An attempt to adapt a model developed by Doué and Laurent had to be abandoned due to differences in the basic conception of the model whose correction would have required more time than available until the date of this report.
Finally, the decision has been made to adjust the experiments to the available data from B.Frackowiak and to obtain comparable results this way. The 'isolated droplet' model will be used for qualitative comparisons only.

3.3 General assumptions for the absorption simulation

To simplify the calculation process, and therefore reduce computation time and resources, several hypotheses have to be made. Table 3.2 below gives an overview of these simplifications. Some of the assumptions will be modified in during the development of the simulation code. These

are marked by commentaries.

Droplet	Beam
Spherical droplets	Cylindrical beam;Gaussian energy distribution [1)]
Static, spherical vapor field [2)]	No diffraction at the interface
T constant inside the vapor field	Beam centered on droplet
Droplet as 'intensity hole' [2)]	Beam moves, droplet static
[1)] modified for deconvolution(details see chapter 5.3	[2)]dependent on the evaporation model

Table 3.2: Simplifying assumptions of the simulation

It is important to note, that this simulation already implies the simplification of the IRE technique presented by Drallmeier et al. as discussed in chapter 2.3.2! Only by using these assumptions the giving up of diffraction calculations can be rectified. Additionally, it is sufficient to perform the simulation for the Infrared wavelength only, since there is no visible absorption in the vapor phase. For that, the results of the Infrared-only simulation can be compared to the experimentally determined difference between the two wavelengths.

3.4 Algorithm

3.4.1 Beam intensity profile

Basis for the simulation of the beam is a square 2D-Matrix with the dimensions $[u, v] = \left[-\frac{D_{beam}}{2}; \frac{D_{beam}}{2}\right]$. As size for the spatial step a tenth of the droplet diameter is chosen. Given a beam diameter of $1mm$ this results in a [42x42] matrix for a droplet of $238\mu m$ and in a [58x58] matrix for a droplet of $173\mu m$.
The values for the intensity profile are added in a two-step mechanism. First, all cells in the corners of the matrix - which are beyond the beam diameter - are set to zero:

$$I\left((u,v), \sqrt{u^2+v^2} > \frac{D_{beam}}{2}\right) = 0 \tag{3.4}$$

As a second step the remaining cells are filled using an analytical expression of the desired profile. For the case of the Gaussian-shaped intensity profile the following expression is used:

$$I\left((u,v), \sqrt{u^2+v^2} \leq \frac{D_{beam}}{2}\right) = \frac{2}{\pi \cdot w^2} \cdot \exp^{-2 \cdot \frac{u^2+v^2}{w^2}} \tag{3.5}$$

'w' expresses the width of the laser beam. Figure 3.8 shows an example of the resulting normalised intensity profile.

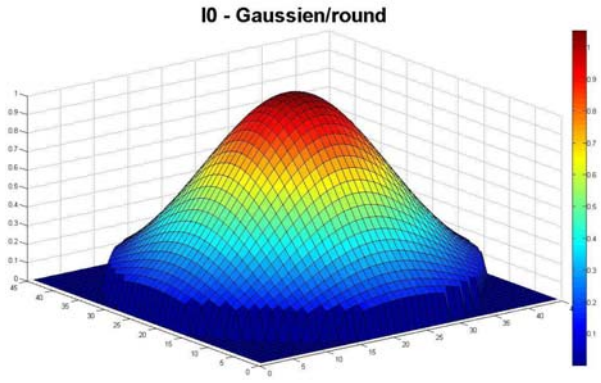

Figure 3.8: Computed Gaussian intensity profile

3.4.2 Droplet and surrounding vapor field

The creation of the droplet/vapor field matrix corresponds widely to a 3D-version of the process described for the laser intensity profile. However, the details differ strongly:
The basic matrix is of a cubic format with the dimensions $[x, y, z] = \left[-A_v \cdot \frac{D_{drop}}{2}; A_v \cdot \frac{D_{drop}}{2}\right]$. The factor A_v describes the expansion of the vapor field around the droplet and depends on the droplet diameter and temperature. B.Frackowiak determined its value to be between 9 and 12 [15]. Consequently, for a droplet of $238\mu m$ only slightly over room temperature ($A_v = 9$), we arrive at a matrix of 181^3 cells.
The second difference is the repartition into multiple zones for the concentration values. For the laser intensity a two-zone concept - outside equals zero, inside is filled - was sufficient. For the droplet we have to distinguish four zones:

1. Outside the vapor field
2. Inside the vapor
3. Between droplet surface and center region
4. Droplet center region

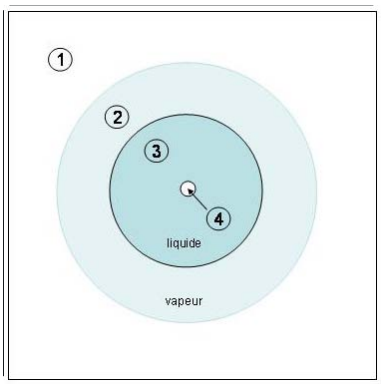

Figure 3.9: Zones for concentration calculation

For the zones one and two a similar algorithm as for the laser profile is used, but employing expression 3.1 for the concentration distribution. The distinction between zone three and four is necessary because of the refraction of the incident beams inside the droplet. Geometrical optics calculations show that every (infinitely small) beam which enters at a distance greater

than $D_{drop}/200$ from the droplet center will be refracted in a way that it does not reach the collimation lens of the setup - and thus the detectors - anymore[3]. As a consequence, the detector will see the droplet as an 'intensity hole' (zone 3 $\rightarrow c_{m(x,y,z)} = 0$) with an illuminated center of high concentration (zone 4 $\rightarrow c_{m(x,y,z)} =>>$).

As a last step, the resulting 3D matrix is summed up in the z-direction to obtain a corresponding 2D-matrix. This compression facilitates the superposition of concentration- and laser matrix in the next step.

Changes for the advanced evaporation model

In the case of the pre-calculated vapor field no computation of the concentration values is necessary anymore. Vapour fields are provided by B.Frackowiak in the TecPLOT^{TM}'.plt' format for the two cases shown below:

	Diameter μm	Temperature $[^{circ}C]$	Spacing $[D_{drop}]$
Case I	238	45,6	3,76
Case II	173	22,4	2,00

Table 3.3: Characteristics of the provided vapor fields

To adapt these files to Matlab, they have to be preconditioned in TecPLOT: First, the originally unstructured mesh has to be interpolated into a Cartesian grid using the same spatial increment as discussed above. Then, the values can be saved as '.dat' files and imported directly in Matlab. It has to be noted, that the separation of the liquid phase into two zones is not performed for this case! Results from the simulation using the 'isolated droplet' model show, that the influence of the center peak is negligible. Therefore, all the droplet cells are filled with a very high concentration value to simulate the total extinction in this region.
Figure 3.10a shows an example of the vapor field as imported into Matlab. We see, that it is a 2D matrix, showing only half of the droplets (since the field is regarded to be axisymmetrical) and that it is not centered on a droplet but on the space between. Since the region of higher concentration trailing the droplet does not reach farther than half of the droplet spacing, following steps can be performed to adjust the matrix to our needs:

1. Vertical cut of the matrix at the center and switching of the two halves $\rightarrow$ centered on droplet
2. 360° rotation $\rightarrow$ 3D-matrix. See figure 3.10b
3. compression in z-direction

The final result is a 2D matrix corresponding to the one created for the simplified model. For details of the steps above please refer to Annex B.

[3]Only 1^{st} order beams are taken into account

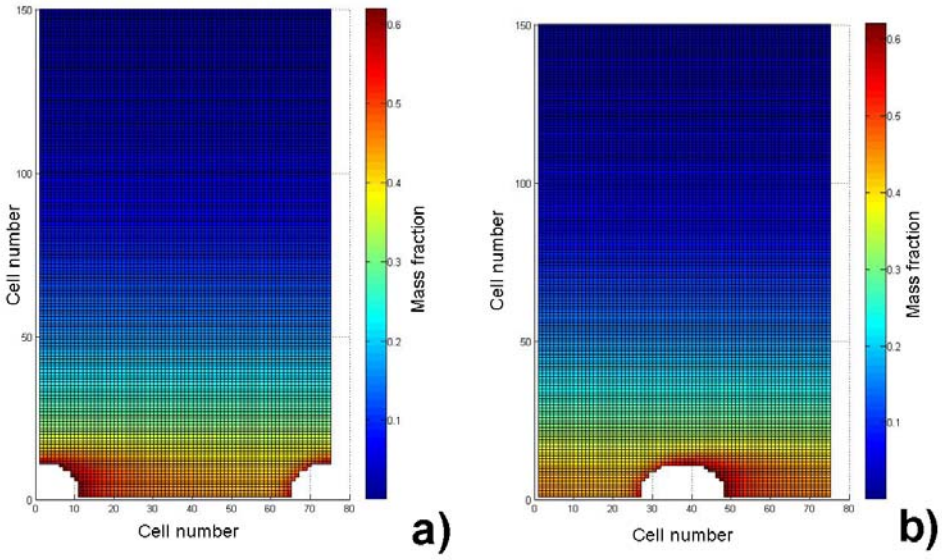

Figure 3.10: Provided vapor field a)after import b)center plane after adjustments

3.4.3 Superposition of beam and vapor field

The intersection of beam and droplet stream in the real experiment is modeled by a stepwise superposition of the laser intensity matrix and the respectively compressed vapor concentration matrix. For this purpose, a displacement vector is introduced. A vector is sufficient, instead of a matrix, because the movement of the beam follows only one direction, along one of the main coordinates. The length of this vector $'h'$ is $\left[-(A_v+1)\cdot\frac{D_{drop}+D_{beam}}{2};(A_v+1)\cdot\frac{D_{drop}+D_{beam}}{2}\right]$. This assures, that the movement starts and ends without superposition of the two matrices. Figure 3.11 illustrates the real and the simulated overlap.

The concentration matrix is locked at the origin of $'h'$. The beam matrix advances stepwise from the negative border towards the positive.

Now, for each step $(h_i))$ each cell of the beam matrix is checked, if it superposes with a cell from the concentration matrix. This is done by a comparison of distances. If the absolute position of of the cell is smaller than the radius of the vapor field, no absorption occurs and the original intensity value is kept:

$$\overbrace{\sqrt{(h_i-u_n)^2+(z_c-v_m)^2}}^{\text{absolute position}} > \frac{A_v\cdot D_{drop}}{2} \tag{3.6}$$

$$I_{(u,v)} = I_{0(u,v)} \tag{3.7}$$

Note: The term $'z_c'$ defines the distance of droplet center to beam center perpendicular to the movement direction. For the position of the beam centered on the droplet it is set to zero.

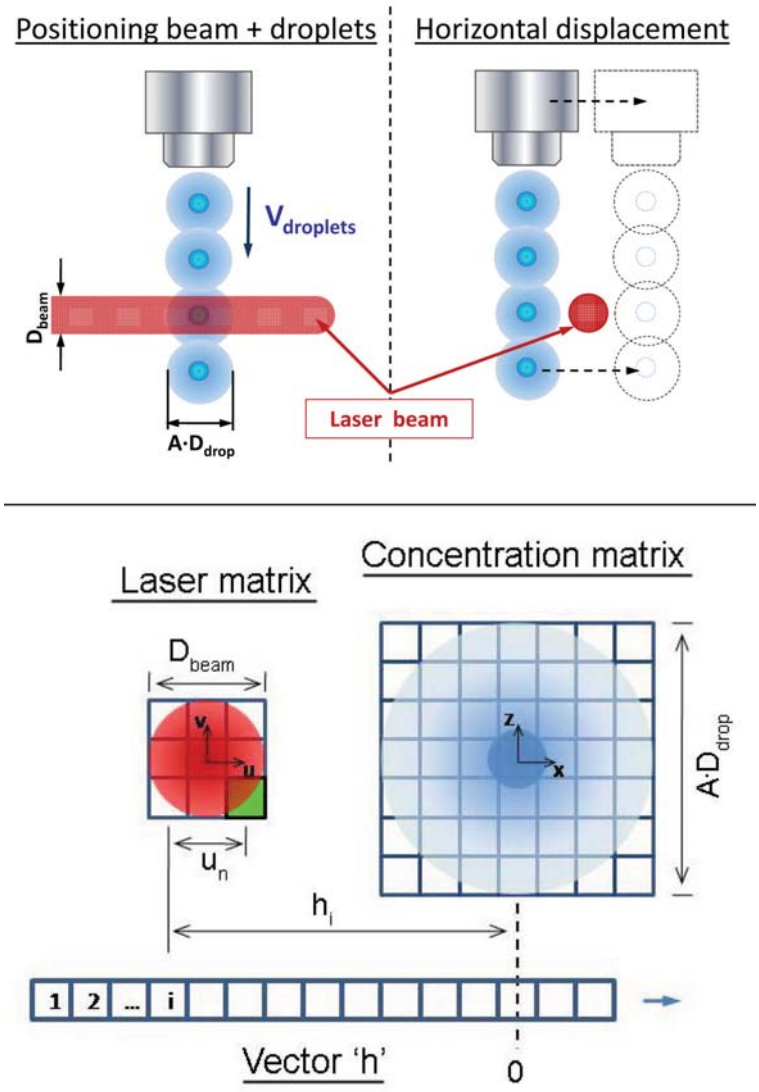

Figure 3.11: Overlap of beam and vapor field. Top: experiment; Bottom: simulation

An expansion of this expression to calculate all the possible positions between beam and droplet demands the introduction of a second displacement vector, perpendicular to $'h'$. This has been done for test purposes. However, for comparison to measurement results only one position - corresponding to the experimental conditions - is necessary. For that comparisons shown in this work will restrict themselves to one position ($z_c = 0$, if not mentioned differently).

If an overlap is detected, the corresponding vapor concentration value $c_{m(x,y)}$ is determined. The new intensity value is calculated following Beer-Lambert's law:

$$I_{(u,v)} = I_{0(u,v)} \cdot 10^{-\epsilon \cdot c_{m(x,y)} \cdot \Delta x} \tag{3.8}$$

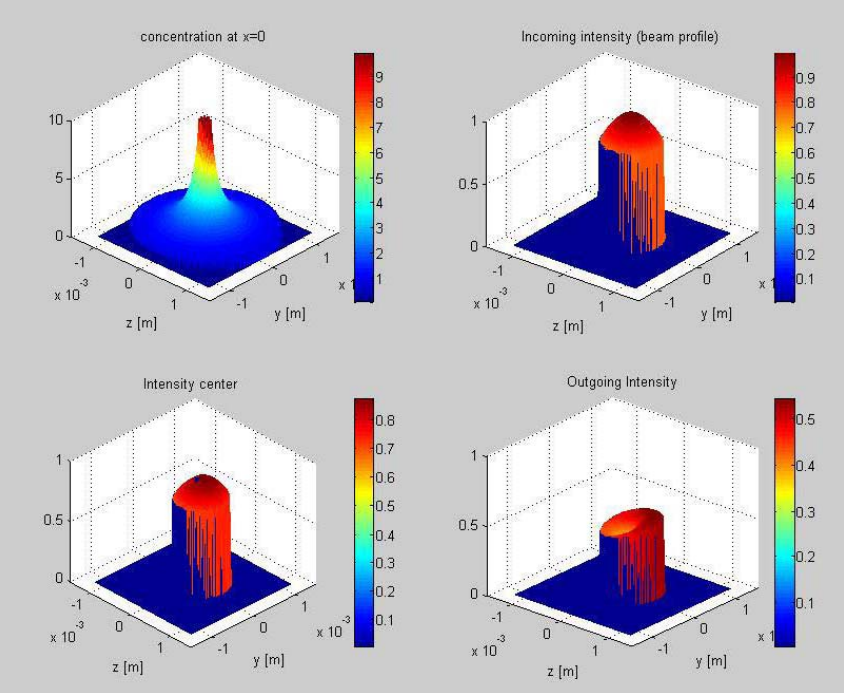

Figure 3.12: 3D model of the attenuation of laser intensity

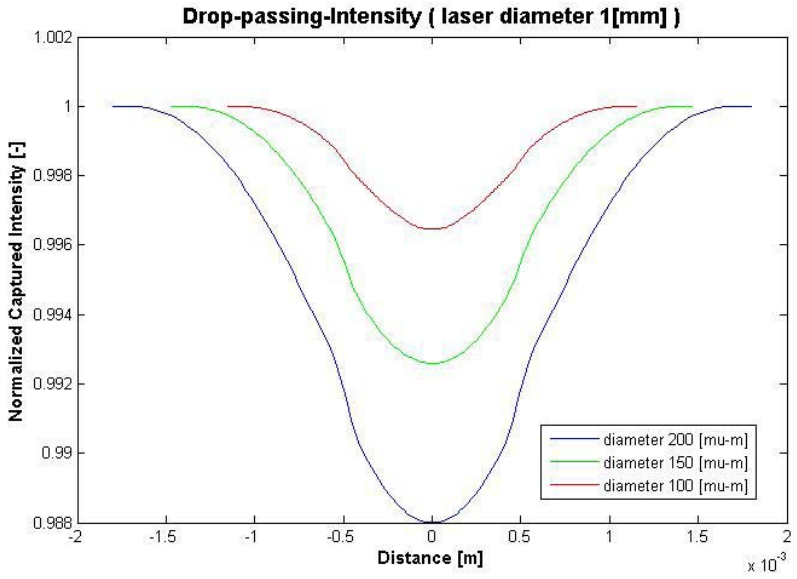

Figure 3.13: Global laser intensity while traversing a droplet

At the end of each step the intensities of all of the beam cells are summed up into one value (corresponding to the detector in the experimental setup) which is stored. Figure 3.12 demonstrates the attenuation of the laser beam when traversing the vapor field. The top row presents a cut through the center plane of the vapor concentration (left) and the initial Gaussian beam profile(right). In the bottom row, the remaining laser intensities midways through the vapor field (left) and after the completed traverse (right) are depicted. The beam is placed off-center to the vapor field for better visualization of the absorption effect. Neighbouring figure 3.13 shows the propagation of the integral value for several droplet diameters.
The noticeable bend in the lower third of the shapes shows the influence of the droplet, forming the discussed 'intensity hole'. However, for heated droplets the augmentation of evaporation renders the vapor field dominate and hides this effect. An important point is the low level of absorption predicted by this simulation! Since the expected signal diminution is smaller than 2% of the emitted radiation, great care has to be taken to avoid ambient influences on the setup as well as signal noise.
Other factors that are supposed to influence the bell-like shape of these curves are the superposition of the spherical concentration field with the circular beam shape and the Gaussian energy profile of the beam. To quantify these effects, tests have been performed:

3.4.4 Test of the influence of the beam energy profile

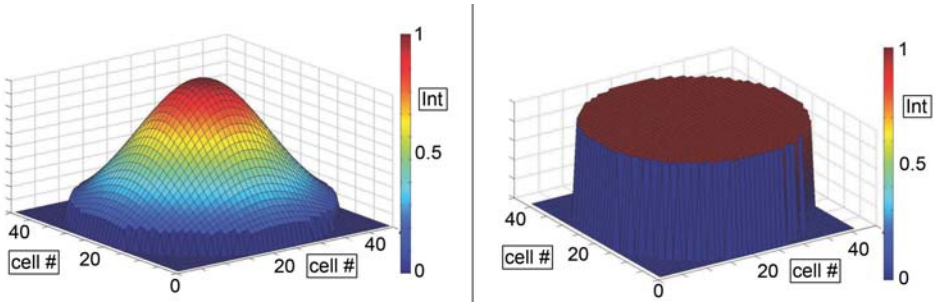

Figure 3.14: Gaussian and flat beam used for test purposes

To isolate the influence of the beam energy profile a series of tests has been performed: For three types of vapor fields - a volume of constant concentration, the field of the isolated droplet model(chapter 3.2.2) and the field calculated by B.Frackowiak (chapter 3.2.1) - the absorption was calculated two times, once with a beam carrying an Gaussian energy profile and the second time with a beam of constant energy. Figure 3.14 presents visualizations of these beam models. For the case of isolated droplet and DNS vapor field, the droplet providing the fields was chosen with a diameter of $173\mu m$ and a temperature of $295.15K$. Ambient conditions are $p_0 = 101325Pas$ and $T_0 = 293.15K$. Figure 3.15 shows the results of the test series. Since the vapor field of B.Frackowiak takes the interaction between the droplets of a droplet stream into account, two profiles exist for this case. One, between two consecutive droplets (designated 'vertical') and another perpendicular to the stream (designated 'horizontal').

We see in those normalized images, that the difference in absorption between Gaussian and

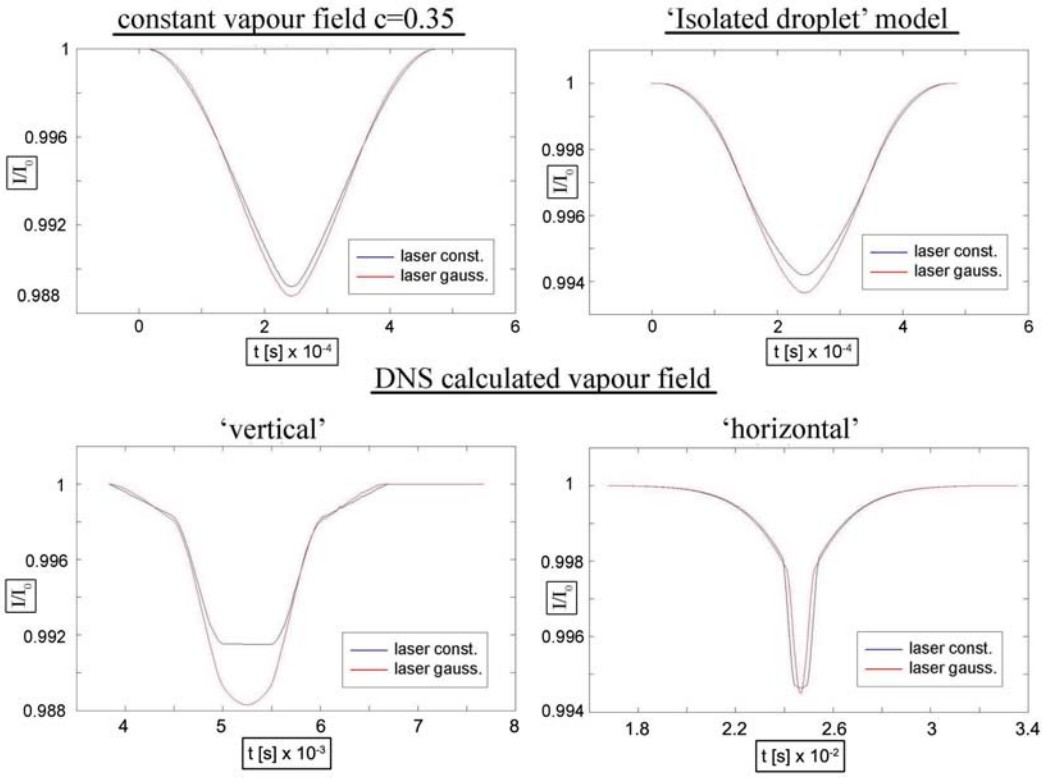

Figure 3.15: Beam energy profile influence on absorption for several vapor field models

flat energy profile is visible but - except of the vertical profile of the DNS calculated field - very small (less than 2% of the amplitude value). Therefore, for most of the test cases simulations of the absorption process can be done using approximated beam intensity profiles without risking unreasonable results.

3.4.5 Test of the influence of the beam shape

The influence of the beam shape is important inasmuch as the intersection of a cylindrical beam with a spherical droplet field poses a challenge for geometrical investigations. Especially for algorithms like deconvolution (chapter 5.3.1) a simplification of either of the two geometries can be desirable. The quantification of the shape influence was done using the CFD calculated vapor field only, since it proved to be the most sensitive to changes in the beam characteristics. Figure 3.16 presents the four profiles - Gaussian-round, half-Gaussian square, flat-round and flat-square - used in this test series. To keep the results clear, only two profiles at a time are compared. Figures 3.17 and 3.18 show the results of the simulations. The characteristics of the DNS droplet field are the same as mentioned in chapter 3.4.4.

This time the deviations seem more significant as for the intensity profile comparison. Again, the biggest difference can be observed for the simulation between the droplets. This was to be expected, since this configuration represents the case with the smallest extent, making it

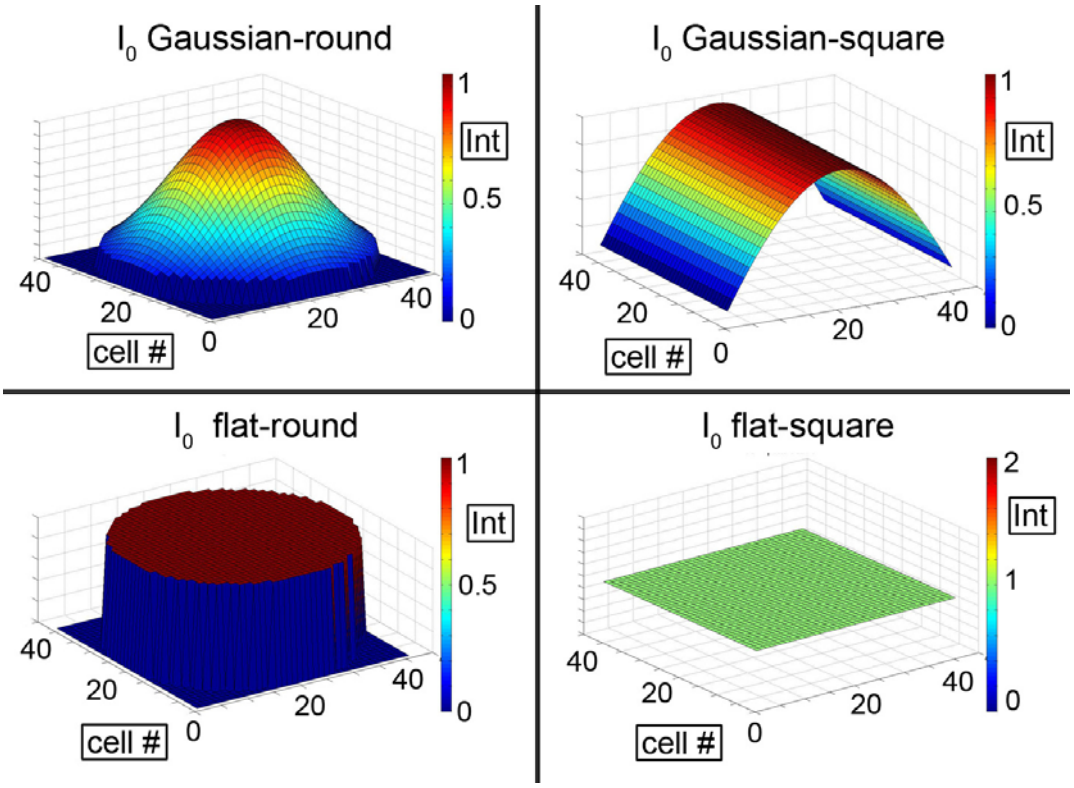

Figure 3.16: Beam test profiles. From top left to bottom right: Gaussian-round, Gaussian-square, flat-round, flat square

sensitive to changes in the beam which has nearly the same size a one droplet spacing. More interesting is the fact, that a change of the beam geometry influences strongly the width of the resulting signal perpendicular to the stream. Since this curve is composed of 'vertical' results at multiple radial positions, a change in this shape signifies a miscalculation of several positions. Looking at the radial coordinate of these positions we see, that most of them are situated at, or near the droplet/vapor interface. Expressed differently: A simplified beam geometry influences exactly the zone which is of the most interest to our investigations. Therefore, a change of beam shape is not recommendable.

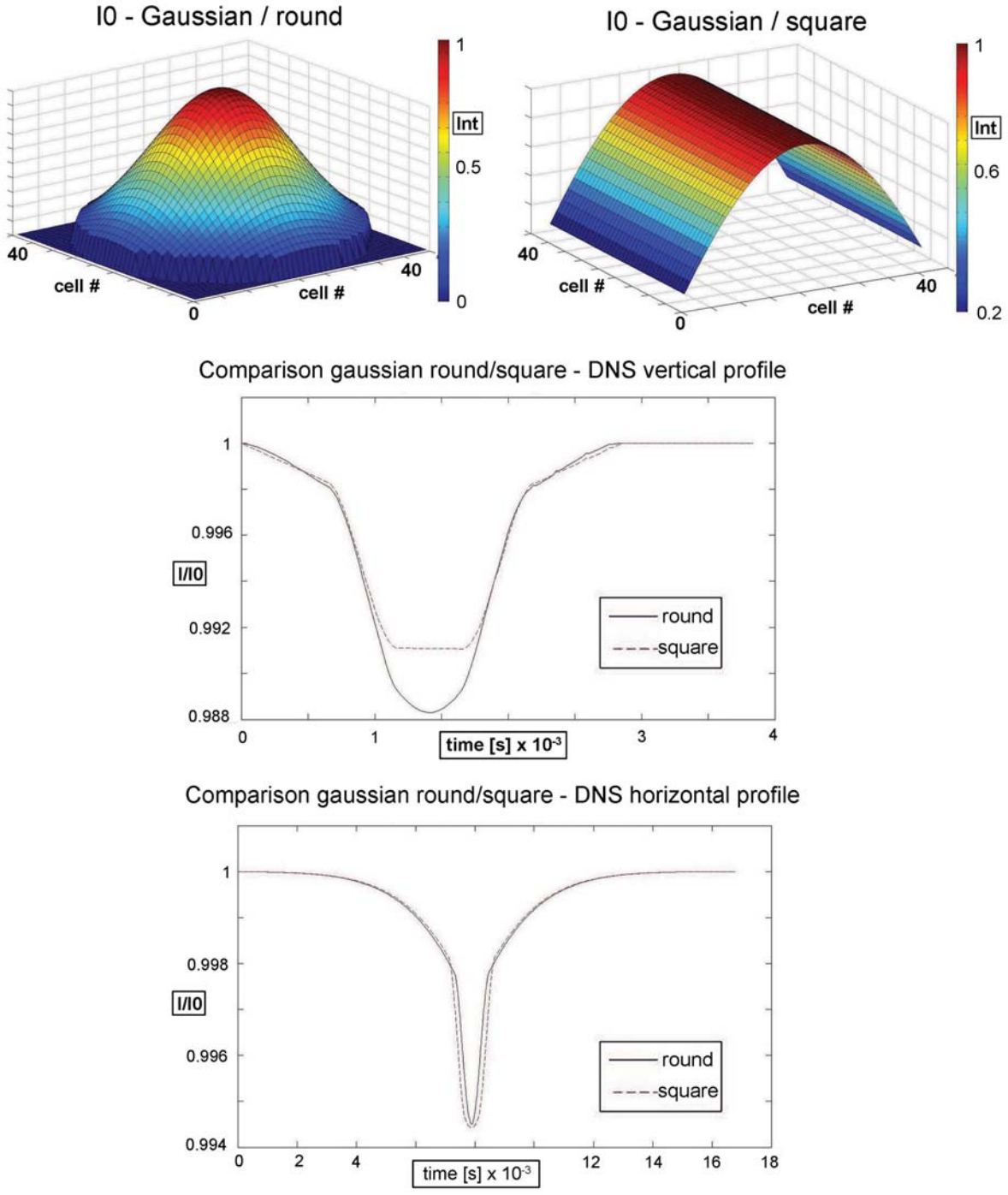

Figure 3.17: Comparison of round and square Gaussian profiles

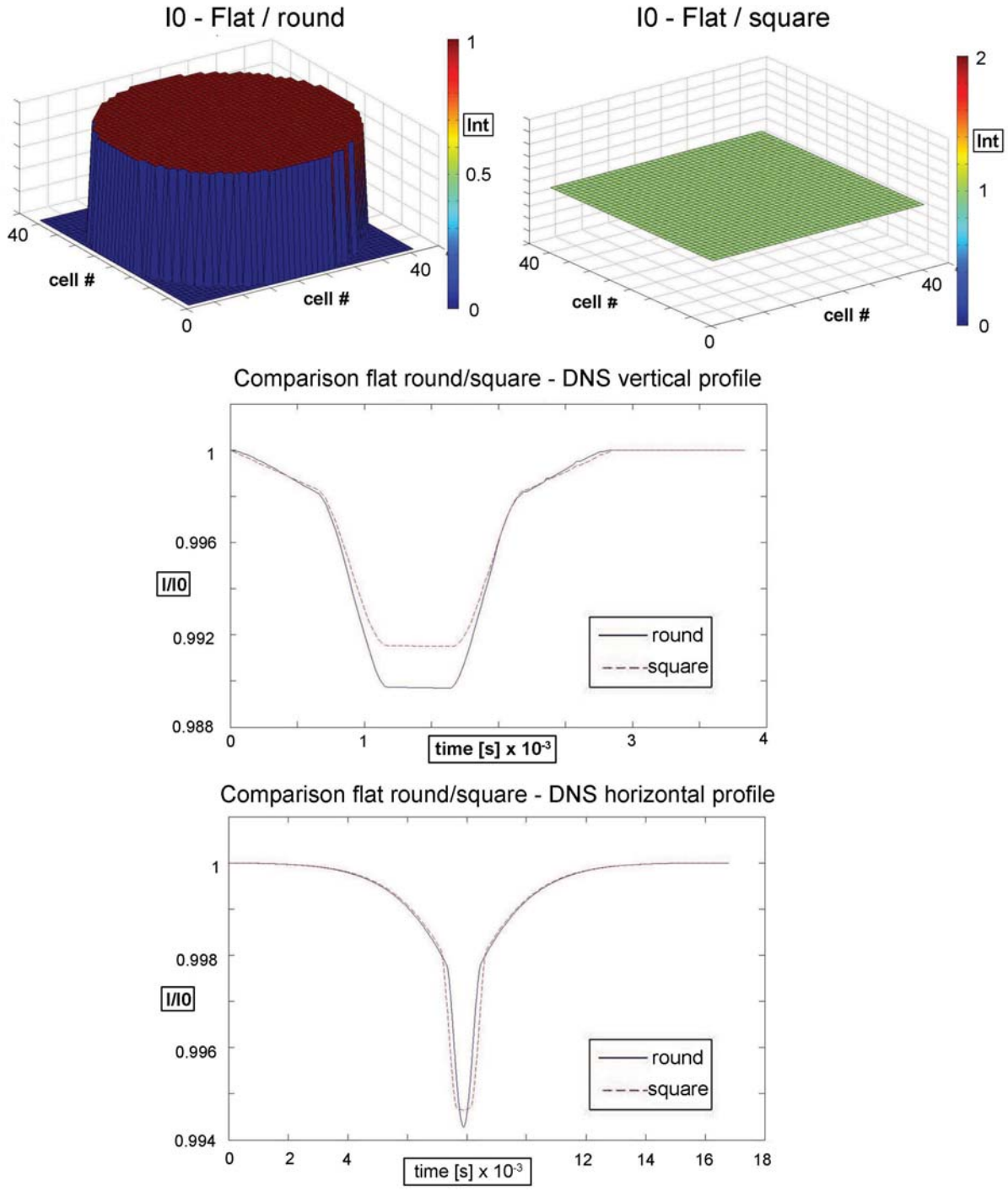

Figure 3.18: Comparison of round and square flat profiles

Chapter 4

Experimental devices

4.1 Requirements to the test rig

In chapter 2.4 the decision to employ a stream of monodisperse droplets as experimental configuration has been made. The goal of this chapter is to define a way to include this choice into a setup for extinction measurements. For various reasons, which will be detailed below, the following requirements to the setup can be defined:

- Simultaneous measurement at two wavelengths
- Temporal resolution of the signal
- High rate of acquisition
- Easy access to all components
- Flexibility through modular conception
- Mobility

The first three points represent demands that origin in the IRE technique or the choice of monodisperse droplets:
Simultaneous measurement at the two wavelengths is not strictly necessary for extinction measurements, if the investigated medium rests stable in its characteristics. In this case, a simple change or tuning of the light source suffices to obtain the desired data. But, even when neglecting aperiodic ambient influences, which can alter this stability, one can no longer speak of real in-situ measurements. Since this is one of the goals set for this thesis, the employment of two wavelengths at the same time is essential.
Temporal resolution and high acquisition rate are connected to the choice of the monodisperse droplets. Since droplet velocities are expected to be in the order of seven to eight m/s, the resulting duration in which a droplet passes the laser beam is one to 1.5 milliseconds . Therefore, a temporal resolution of at least one kHz is necessary to distinguish a droplet signal from the

spacing between[1].
The latter three requirements are of practical nature only:
Easy access to all components and modular conception are demanded to keep maintenance simple and to have the possibility to upgrade the system without reconstructing the whole rig. Additionally, this setup is envisaged not to serve only for academic purposes, but it will also fulfill an educational role, helping students to understand the principles of extinction. Therefore, an 'open' display of all of the components is preferable to a 'black-box' system as it is required for industrial applications. Difficulties that result from this choice are discussed in chapter 8.
As a last point, mobility is desired for future use of this technique. Some spray or evaporation systems at ONERA, that would be interesting to investigate using the IRE, are permanently installed in large test benches. As a consequence, an additional investigation technique has to be installed there. Possessing a mobile and compact infrared rig will facilitate this task enormously.

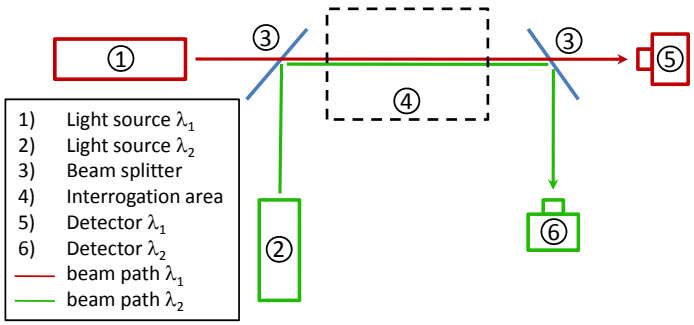

Figure 4.1: Layout of the classical IRE setup

A literature survey on IRE test rigs used so far had the surprising result that since the first introduction of simultaneous extinction measurements by A.R.Chraplyvy and D.C.Hammond [7, 59] in the 1980s, the basic experimental layout has practically stayed the same. Figure 4.1 shows a scheme of the classic conception consisting of a straight line-of-sight measurement branch for one wavelength and an U-shaped addition for the second wavelength. The superposition and separation of the two beams is realized by the aid of two semi-transparent mirrors which act as beamsplitters.
Only three publications, Adachi et al. in 1990[8] ,Drallmeier et al. in 1994[40] and Klingbeil in 2007 [33], propose changes to this arrangement:
As already described in section 2.3.2, Adachi et al. use a broadband light source and an array of narrow band-pass filters instead of the laser/beam splitter combination. Although this makes the setup more flexible in terms of wavelength and, according to the authors, cheaper, a simultaneous measurement of two selected wavelengths could not be realized. Additionally, wavelength-dependent energy fluctuations of this light source are mentioned.
Drallmeier et al. modify 'the other end' of the system by replacing the two independent detectors with one sandwich-type sensor of own manufacturing. This measure economizes one beam splitter, assures the same path length for the two laser beams and renders the setup narrower, making it easier to insert in existing test benches. However, this sensor type is not produced industrially and therefore hard to come by. Furthermore, it would prevent a change of one of

[1]supposing that the distance between droplets is greater than the beam diameter

the wavelengths for other applications if desired.
The third proposition of Klingbeil concerns the use of optical fibers to connect light sources, investigation area and detectors. The results of this approach are an extremely flexible and highly miniaturized system. Also disturbances on the laser intensity along the beam paths are limited to the easily quantified influence of the optical fiber. The way of superposing and separating the two beams by optical couplers is discussed in detail by the authors. But again, once installed, the choice of laser wavelengths is limited to the spectral range transmissible by the fiber material.

After comparing the alternatives, the decision was made to use the classic layout for our experiments. The concept of Adachi et al. lacks the possibility for simultaneous measurements and is therefore not suitable to our demands. The sandwich-type detector of Drallmeier et al. is out of question too, since it is not commercially available. Employing optical fibers may be a good idea in general. But while Klingbeil performed his experiments at an infrared wavelength of 1.5 μm - where optical fibers are easily obtainable - a research for the use at greater wavelengths proved difficult. The only optical fibers found for wavelengths of 3.36 μm or greater are not only limited to lengths below one meter, but would have significantly exceeded the designated budget.
The detailed choice of components and their characteristics was done following the recommendations by Hassa and Giuliani. Their investigations in the frame of the LOPOCOTEP project [43, 44] represent one of the most recent studies using this type of infrared extinction setup.

4.2 Detailed Description Of The Test Rig

As mentioned above, the layout of the test rig is similar to the one of Hassa et al. used in the LOPOCOTEP project. Therefore it consists of a straight arrangement for the infrared beam which is connected to an U-shaped assembly for the visible branch of the setup. Figures 4.2+4.3 shows a scheme and a photograph of the bench.

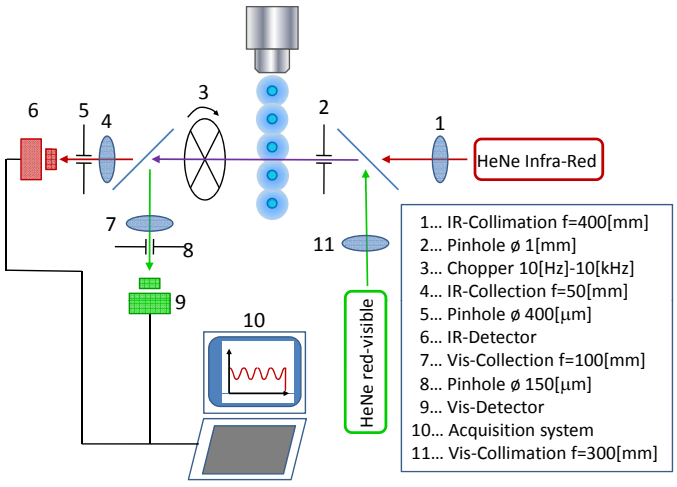

Figure 4.2: Scheme of the test rig

Figure 4.3: Assembly in the droplet configuration

In this section, a detailed description of the main components from laser source to data acquisition is given. Further technical specifications for all of the components described below can be found in Annex **??**.

4.2.1 Laser sources

The two continuous He-Ne lasers from Thorlabs,Inc. are the principal components of the setup. Table 4.4 presents some technical specification for both models, H339P2(Infrared) and HRP050(visible-red).

	H339P2	HRP050
Wavelength $[nm]$	3392	632,8
Polarization	linear > 500:1	
Power $[mW]$	2	5
Initial beam diameter $[mm]$	2.02	0.8
Operating Voltage $[VDC]$	2800	2400
Operating Current $[mA]$	6,5	5,25
Length $[mm]$	533,4	425,5
Diameter $[mm]$	44,5	

Figure 4.4: Technical data of the laser sources

Figure 4.5: Thorlabs H339P2

These Lasers have been chosen for their known good stability over longer intervals of use, their economy in maintenance as well as in acquisition and their compact design. However, intensive preheating is necessary to achieve all of the above characteristics. Further descriptions on this point can be found in chapter 4.3.1 below.

4.2.2 Detectors

The tasks of converting the incoming radiation into electric signals is fulfilled by two wavelength-specific detectors. Due to usability, cost and the higher S/N ratio, photodiodes are chosen over photomultiplicators. The main selection criterion was high sensibility at the respective laser wavelength. Suitable models for both wavelength are provided by Hamamatsu Inc. Figure 4.6 shows their spectral responses.

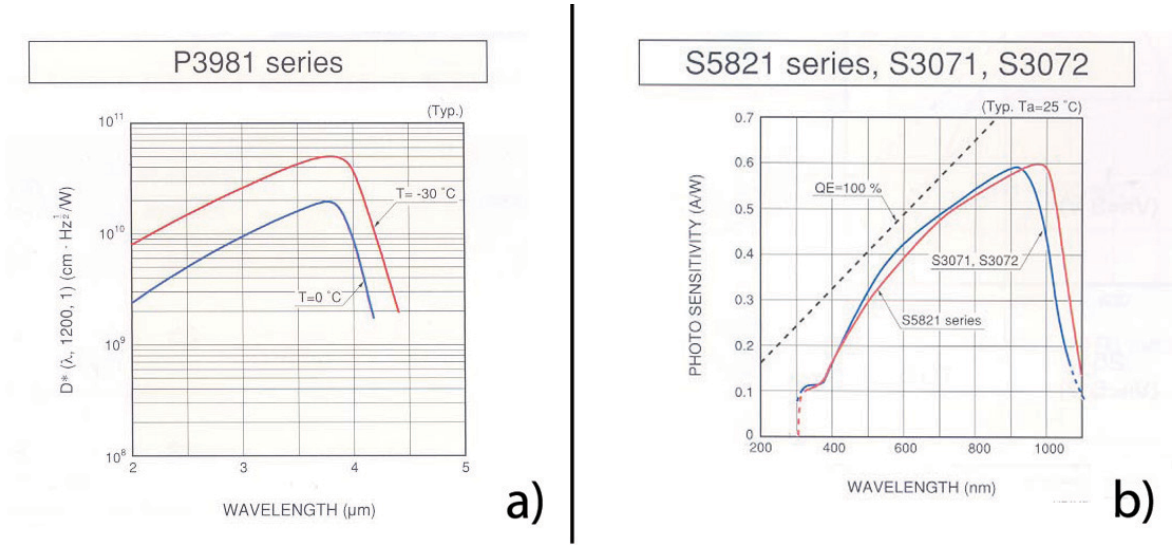

Figure 4.6: Spectral response of the employed photodiodes. a) IR; b) visible

Visible wavelength: The visible detector is a Si-type photodiode, model S5821-02. It operates at ambient temperature with an output signal of 0,42 $[A/W]$ and an optimal spectral range from 600 to 900 $[nm]$. Due to the low power output of the laser, the diode is connected to an integrated low-noise preamplifier/evaluation circuit type C9052 of the same company. The transimpedance (or 'amplification') is $15[kV/A]$.

Infra red: To measure the amount of infrared radiation a PbSe-photoconductive detector, type P3981 is employed. Its output signal reaches a maximum at an optimal wavelength range between 3 and 3,7 $[\mu m]$. To minimize thermal noise it is embedded in a thermoelectric heatsink which keeps the operating temperature at -30 $[°C]$. At this configuration $D^*_{(500,1200,1)} = 6,5 \cdot 10^9 [cm\sqrt{Hz}/W]$ was measured by Blackbody calibration. Again, due to the low laser power, a pre-amplifying device follows the diode.

4.2.3 The monodisperse droplet injector

The piezo-ceramic injector (see figures 4.7 and 4.8 above) is the main experimental device for this work. Its task is to provide a stream of calibrated droplets with the same size, velocity

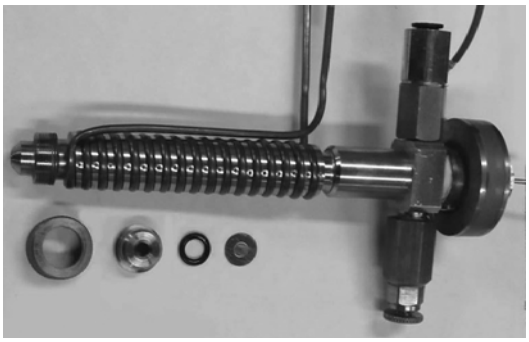

Figure 4.7: Injector Components

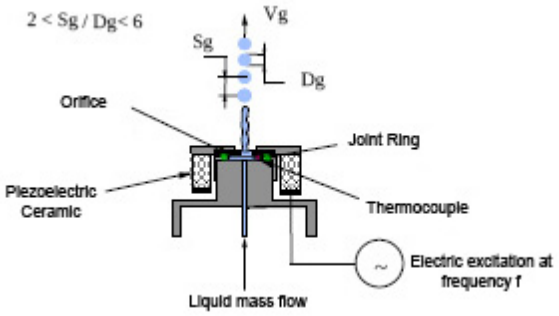

Figure 4.8: Cross cut: Working Principle

and spacing parameter $C = \frac{S_D}{D_{drop}}$ at a given distance from the orifice. This is assured by the following working principle:
A piezo-electric ceramic, driven by a frequency generator, creates a mechanical Rayleigh instability at the excitation frequency f_{ex}. This instability propagates through the injector body and is transmitted to the liquid which passes a calibrated orifice plate. Inside the liquid, the instability is growing until it results into disintegration of the jet, forming a droplet. Each electrical impulse on the ceramic will create one droplet. Therefore the droplet frequency is equal to the excitation frequency and adjustments on the latter influence the droplet spacing directly.
In the present experiences, orifices of 100 and 50$[\mu m]$ in diameter are used. This allows to obtain droplet diameters around 200 and 100$[\mu m]$ respectively. All presented results were acquired in a distance from the orifice of 35 to 50 $[mm]$. The spacing parameter is set to comply with the frequency of the ceramic and the velocity with the pressure in the fuel reservoir. The decrease of the droplet diameter in the stream due to evaporation is ignored [4].

Characteristics of the liquid jet

The characteristics of the droplet jet can be derived from the equation of mass conservation as was shown by B.Frackowiak [15]:

$$Q_l = \frac{4 \cdot \pi}{3} \frac{D_{drop}^3}{8} \cdot f_{ex} \tag{4.1}$$

$$\text{or } D_{drop} = \sqrt[3]{\frac{6 \cdot Q_l}{\pi \cdot f_{ex}}} \tag{4.2}$$

Mass flow conservation permits to include the droplet velocity:

$$Q_l = \frac{\pi}{4} \cdot \Phi_0^2 \cdot V_{inj} \tag{4.3}$$

$$\text{and for that } D_{drop} = \sqrt[3]{\frac{3 \cdot \Phi_0^2 \cdot V_{inj}}{2 \cdot f_{ex}}} \tag{4.4}$$

If we neglect the loss of kinetic energy due to the orifice and the droplet formation, the droplet velocity V_g is equal the injection velocity V_{inj}. Therefore, the droplet spacing can be expressed as:

$$S_D = \frac{V_{inj}}{f_{ex}} = \frac{V_{drop}}{f_{ex}} \tag{4.5}$$

$$\text{leading to } D_{drop} = \sqrt[3]{\frac{3 \cdot \Phi_0^2 \cdot S_D}{2}} \tag{4.6}$$

The ecxitation frequency for the ceramic should be chosen from a range defined by the Rayleigh theory:
The optimal wavelength for maximum jet disintegration is $\lambda_{opt} \approx 4.51 \cdot \Phi_0$. The resulting optimal droplet diameter is $D_{drop} = 1.9 \cdot \Phi_0$. The optimal frequency for which the longest coherent structure of the droplet stream is dependent on injection velocity and orifice diameter only is therefore:

$$f_{opt} = 0.198 \frac{V_{inj}}{\Phi_0} \tag{4.7}$$

In theory, only one stable frequency per injection velocity and orifice diameter exists. However, experiment shows that multiple quasi-stable frequencies exist, but their number is small and is is not possible to obtain droplet spacings greater than $C = 5$. In either case, it is recommendable to verify the monodispersity of the droplet at these additional frequencies.

Verification by shadowscopy

Figure 4.9: Shadowscopy: camera and extended objective

Figure 4.10: Droplet image by shadowscopy (Source both images: [15])

This control of the monodisperse characteristics, before and during the acquisition runs, is achieved by aid of a shadowscopic device. It consists of a classic video camera with a frame rate of $25[Hz]$, a control monitor and a stroboscope. The latter is synchronized to the injector excitation frequency to 'freeze' the droplets on the camera image. Its light is homogenized by an

opaque plate in front of the lamp. To achieve a sufficient zoom factor, the camera is equipped with a extended objective. Figures 4.9 and 4.10 show this objective as well as an example of the acquired droplet images.

4.2.4 The signal chopper

Task of the signal chopper is to enhance the temporal resolution of the setup by providing a stable and uniform reference signal used as main trigger source for the setup. This signal is created by a rotating chopping blade placed in the beam paths. The model chosen for the present experiments is the optical controlled chopper MC1000A from Thorlabs Inc. Its output is TTL/CMOS compatible with voltage range of 0-5 $[V]$ at 200$[\Omega]$ impedance. The chopping frequency can be altered from 1$[Hz]$ to 6$[kHz]$ depending on the slotted blade mounted. At the experiments described in this document the standard 10-slot blade, allowing chopping frequencies from 20$[Hz]$ to 1$[kHz]$ is employed.

4.2.5 Data acquisition and transfer

The transfer, conditioning and storage of the pre-amplified signals is assured by three-component National Instruments acquisition system. It consists of a connector box, which bundles the incoming signals, the acquisition hardware, for digitalization and conditioning, and the acquisition software to control the hardware parameters and to store the processed data.

The connector box: To connect the experimental signals to the PC-system a connector box type NI BNC-2090A is employed. Sixteen analog input BNC connectors provide access for sixteen single-ended or eight differential channels. In this work the second option is used to further eliminate signal noise. The channels were calibrated by a stabilized tension generator for a range of $\pm$ 10 $[V]$ with an average error of less than 0.1 [%]. For transmission of the signals to the acquisition card inside the PC two 68pin connectors are available.

The acquisition hardware: As data acquisition (DAQ) device the NI 6289 PCI card of National Instruments M-Series was chosen. It allows to scan up to 32 analog input channels at 500k $[samples/second]$ maximum at 18 bit. Timing resolution is 50$[ns]$ at an accuracy of 50 $[ppm]$ of the sample rate. In the present experiments, the acquisition rate was kept below 250$[khz]$ for three channels simultaneously to avoid buffer overflow at data storage.

The acquisition software: The last element in the acquisition chain is a Labview^{TM}-based software tool which allows the experimenter to control the main acquisition parameters and to store the data. Figure 4.11 shows the User Interface of this program. Special attention has been paid to the clear and effective layout dominated by the control screen on the right. This screen displays the signals chosen for acquisition by the triggers on its left, allowing to detect signal perturbations at every moment of the experimental run. Input fields for acquisition frequency, duration and data path(not visible in the image) complete the controls. A modular layout of the

source code has been chosen to facilitate the implementation of additional acquisition channels. The acquired data is stored in the Labview-native .tdms format. This file structure is optimized to store a maximum of values and their metadata in smaller files than the regular text formats. Conversion tools for most of the great software packages (including MS Office and Matlab) are provided.

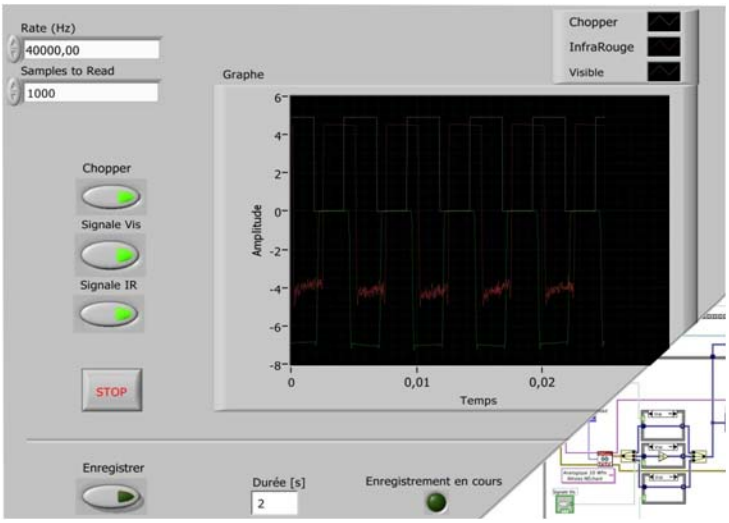

Figure 4.11: User Interface of the acquisition software

4.2.6 Other optical elements

Apart from the main components as laser sources and detectors, several lenses, mirrors and pinholes are situated in the beam paths. They fulfill an important role as collimators, splitters, to redirect or to resize beams. For uniformity, and therefore better control of the system, all elements are of the same brand. Due to logistical advantages product of Melles-Griot were chosen. Focal lengths and diameters follow the recommendations by Hassa et al. as mentioned at the beginning of this chapter.

Lenses: In total there are four external lenses in the setup, two for each wavelength. Lenses at the 'visible' branch of the bench consist of BK7 while the material for the infrared wavelength is CaF_2. Table 4.1 gives an overview of the technical data. Enumeration of the lenses corresponds to the positions in figure 4.2.

Because of the significant difference in wavelength of the two lasers, it proved difficult to find a suitable universal lens material. Therefore no lenses are used while the two beams are superposed. This fact strongly limits the beam control after diffracting elements such as pinholes. While this effect plays a minor role in spray investigation, its a strong influence on the investigation on the droplet stream!

Position	1	11	4	7
Material	CaF_2	BK7	CaF_2	BK7
Diameter $[mm]$	25	25	25	25
Focal length $[mm]$	50	300	50	100
Function	Collim. IR	Collim. vis.	Focal. on pinhole 5	Focal. on pinhole 8

Table 4.1: Characteristics of the employed lenses

Semi-transparent mirrors: The two semi-transparent mirrors act to superpose the two laser beams before the experimental area and to separate them afterwards. Made from silicon they are transparent to the Infrared beam while totally reflecting the visible wavelength. To enhance the transmission, an IR-anti-reflective coating is applied.

Pinholes: The list of optical elements used concluded with three precision mounted pinholes. One, with a diameter of $1[mm]$ is placed right in front of the experimental area. Its purpose is to equal the diameters of the superposed beams. This is necessary since for one reason, the beams are already emitted at different diameters and for a second, cover different distances until they reach the pinhole. For that, divergence changes the diameters even further. However, a pinhole creates diffraction dependant on the wavelength of the passing radiation. This effect was found to have an influence on the measurements (see chapter 4.4).
The other two pinholes, with diameters of 150 and 400 $[\mu m]$ respectively, act, each in combination with a focusing lens, as 'shields' for the photodiodes. They are placed right in front of the detectors and keep any ambient or reflected radiation from influencing the measurements. Only the measurement beams, which are focussed precisely on the respective pinhole, arrive at the detector. This measure has proved to be very efficient even when high-power flashlights or stroboscopes are used next to the running setup.

4.3 Preliminary Tests And Error Sources

With the test rig completely mounted several basic tests are performed. The goal is a functionality-check of the components working together. For this purposes the test cases are kept as simple as possible. First the characteristics of the HeNe Lasers, being the main components, are determined. After that, the interaction of the optical elements along the beam path is observed. The test row is concluded by a simplified absorption experiment, verifying the whole setup.

4.3.1 Determination of the Laser stability

Verifying Laser stability and knowing necessary preheating times is indispensable for successful measurement runs. A even more precise alternative would be the addition of power meters to the setup. However, this is not desirable for our case, since this would mean and additional energy loss to the already low-energy power sources.

To achieve the power output, a simple measurement with an oscilloscope over a time is performed until the laser arrives at maximal power. The visible Laser shows very fast preheating times (<1 minute to achieve maximal power) and good stability right after ignition. However,the infrared one needs approximately 20 minutes to arrive at 100%. Figure 4.12 shows a synthesis of the power measurements. But even after this preheating time, small, low frequency power fluctuations of ≈ 5% can be observed at the positive flank of the chopped signal. An average of another 10 minutes was measured until their disappearance.
As a conclusion of the stability tests, a preheating time of at least 35 minutes is recommended for the infrared Laser source. The visible laser was found to be ready to use after less than one minute.

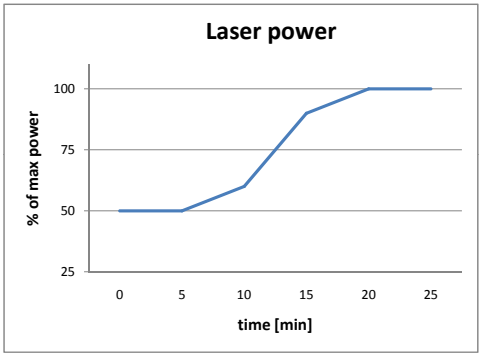

Figure 4.12: Laser power vs. preheating time

4.3.2 Verification of the beam profiles

The next objective to validate was the intensity repartition - or "'the profile"' - of the laser beam. In theory the beam intensity should follow a Gaussian relation like the following:

$$I_{(x)} = I_0 \cdot exp\left(-\beta \cdot x^2\right)$$

x being the distance to the beam center and β an arbitrary parameter.
This profile can be disturbed by defects in the optical elements (scratches on the lenses,...) or by refraction due to a parallax in the alignment of laser beam and pinholes. Taking into consideration that the average diameter of this beam is 1[mm] in comparison to ≈ 200[μm] of the droplets to be observed, knowledge of the true repartition is of the highest importance.
A simple setup can be used to perform the measurements (see figure 4.13):

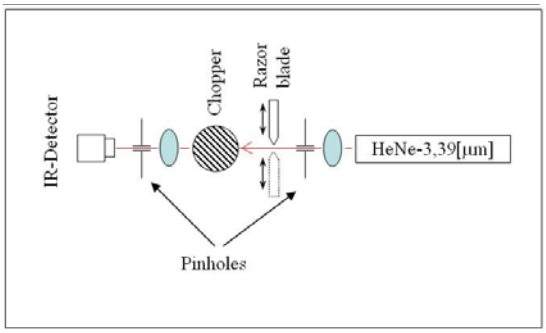

Figure 4.13: Scheme of the setup

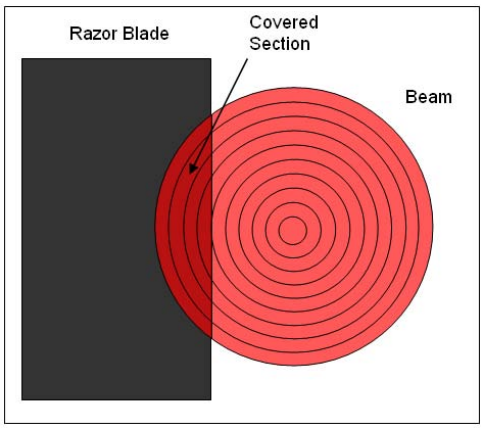

Figure 4.14: Covered section using the onion-peeling-model

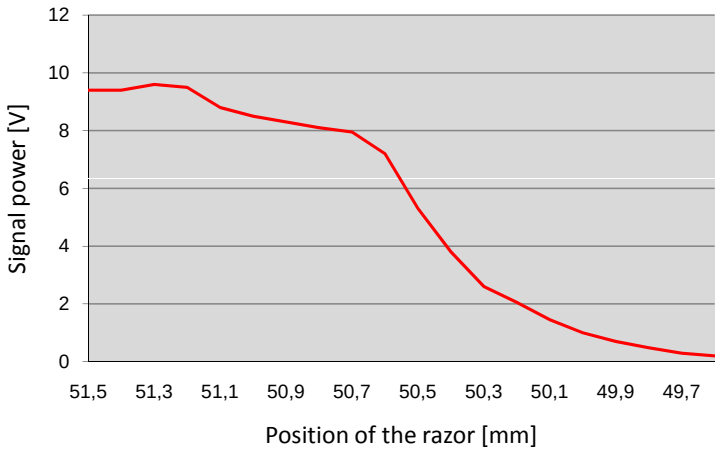

Figure 4.15: Diminution of energy when moving the razor blade

A black painted razor blade mounted on a micrometric sledge is inserted into the beam path. By advancing the blade from one side to the other it obstructs an increasing part of the laser beam from reaching the detector. The resulting diminution of energy is traced in figure 4.15. However, this curve represents the integral diminution. To develop a radial profile, an adaptation of the classic Onion-peeling scheme [59, 7] is used:
Implying an axisymmetric beam, the loss of energy at the detector can be compared to the masked cross-section. Since the movement and the loss of energy are not measured continuously, the beam is divided into concentric rings. The width of these rings is accorded to the step size of the advancing razorblade. In these rings, the energy level is unknown, but considered to be constant. Now the covered area can be "'translated"' into rings covered:

$$A_{seg} = r^2 \cdot arccos\left(1 - \frac{h}{r}\right) - \sqrt{2 \cdot r \cdot h - h^2} \cdot (r - h) \tag{4.8}$$

This is the expression for the complete covered area with r being the ring radius and h the distance between r and the edge of the blade (see figure 4.14). The masked surface of each ring involved can be calculated by the formula above subtracting the surface of the neighbouring ring closer to the centre:

$$A^{h_k}_{ring_j} = A^{h_k}_{seg_j} - A^{h_k}_{seg_{j+1}} \tag{4.9}$$

This is done for all positions of the razor blade (h_k) moving from the outside to the center. In that way the share of each ring for each position can be determined. At the same time the loss of energy can be tied to the share of rings involved. Again, moving from the outside to the center a coefficient for each ring is found, which signifies the relation between energy loss and surface diminution → the "'energy value"' of the ring.
In that way, the desired beam profile can be traced. The following figure shows the results for a distance of 740$[mm]$ between razor blade and the pinhole, determined by the aid of Microsoft

Excel:

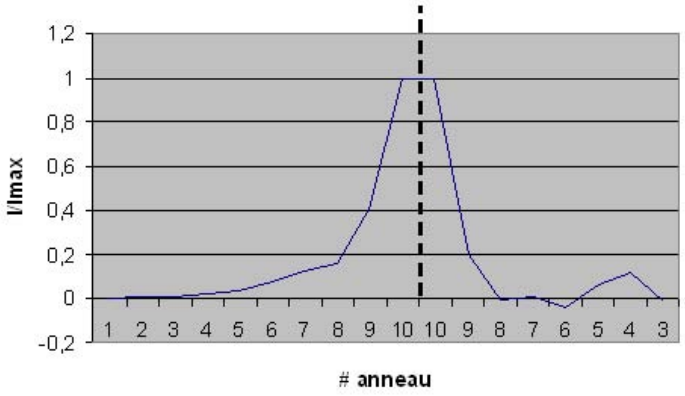

Figure 4.16: Intensity profile 'From right to left'

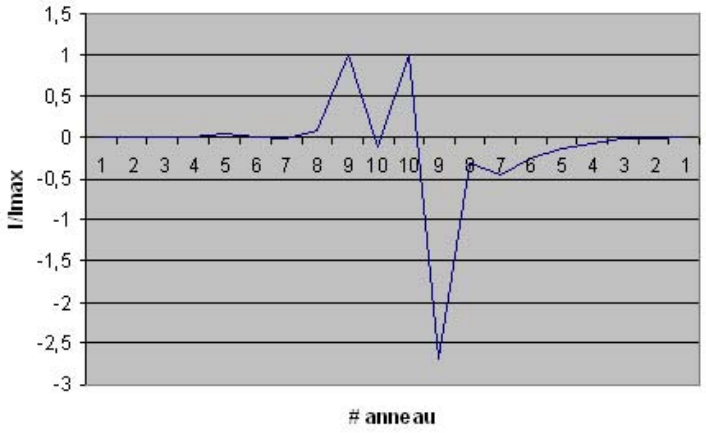

Figure 4.17: Intensity profile 'From left to right'

When looking at the measurements from "'right to left"' it is clearly visible that the determined intensity repartition resembles a Gaussian profile until the beam center is reached. After that the results start to vary strongly. An explanation might be that the whole setup is very sensitive towards ambient vibrations. These disturbances gain importance when the overall intensity becomes lower.
Another explanation would be a bad alignment of the laser beam and the pinhole located at the beginning of the measuring distance. To check this possibility the same measurement was done starting from the other side of the beam (from "'left to right"'). The result is presented in figure 4.17.
This time the heavy distortions appear at the side with heavy intensity while the right half is more similar to the desired result. The negative values are a result of the calculation which uses the coordinates from "'right to left"'. The maximum negative value of more than two-times maximum energy is due to the normalization process which uses the maximum at the "'positive"' side. Altogether this proves the assumption of bad alignment.
To investigate the propagation of the beam along the axis the measurements above are repeated at several axial positions:

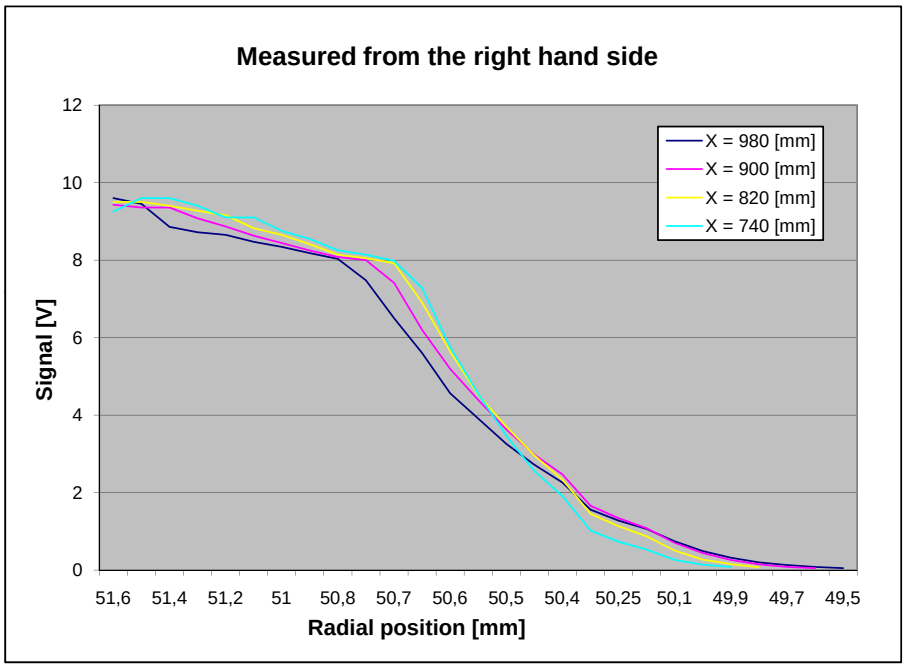

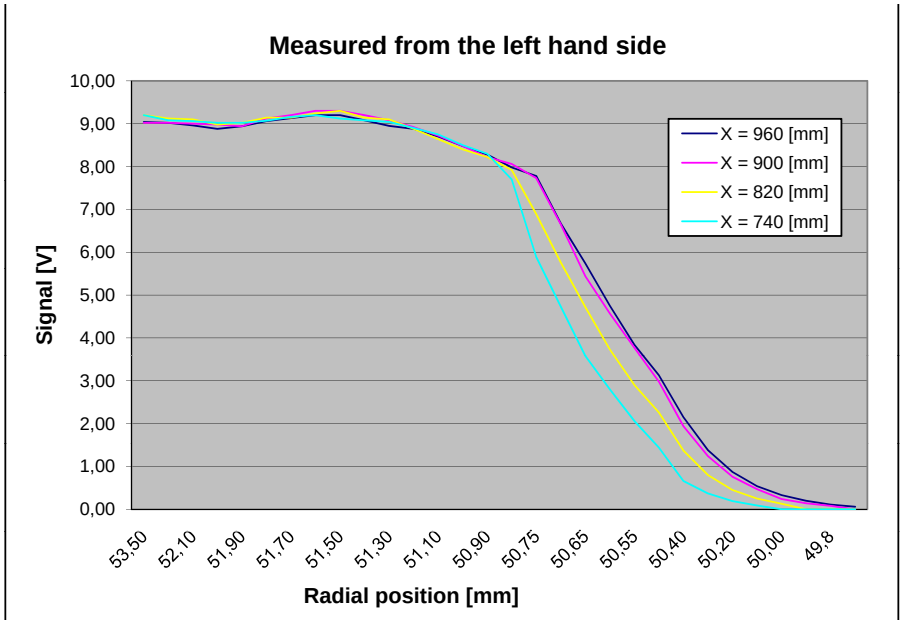

Figure 4.18: Beam profiles at several axial positions measured from both sides

As expected, the profile flattens at greater distance from the pin-hole. But again it is obvious that the measurements made from the opposite direction (see figure 4.18(b)) suffer from distortions. For example between the positions 53 and 51,30 a weak up-and-down is recognizable. This is an indication for refraction rings. These rings are still visible after the realignment of beam and optical elements but at very small amplitude. Considering the low absolute energy level of the Gaussian beam in this region, this effect can be regarded as negligible and the assumption of a Gaussian distributed laser intensity, although quite narrow, is confirmed.

4.3.3 Absorption in a fixed volume

For these first runs only one of the two laser sources is activated at a time. This is necessary to determine the extinction along the way for each wavelength separately.

As test object a square box made of quartz-glass is employed (see figure 4.19). The inner distance between the walls (thus the waylength of the laser beam later on) measures 50[mm] and the wall thickness 2[mm]. To avoid refraction losses the positioning of the front wall has to be carefully adjusted to a 90° direction in respect to the laser beam.
In this manner the losses caused by the empty test box are measured by less than 2% for the beam at 3,39[μm] whereas heavy reflection for the visible laser is observed. This is a little bit surprising, since the box was originally designed for UV-applications and thus for an even shorter wavelength. The fact, that the box walls are not perfectly flat may be the reason for this behaviour. Since the UV-applications before used a laser sheet, these perturbances might have been neglible then.

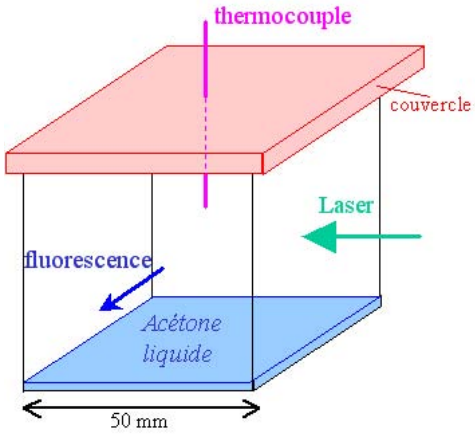

Figure 4.19: Quartz-glass test box

The easiest way to achieve a determined vapor concentration is to saturate the air inside of the test box. For this purpose enough acetone to leave the ground covered by liquid is dispersed. After closing the box and waiting for twenty minutes the mixture inside can be regarded as saturated and homogeneous.
When putting this vapor-filled box into the infrared beam path a diminution of the collected signal by 75 percent ($\frac{\overline{I}}{I_0} = 0,25$) can be observed.

Calculation

The calculations for this test case are rather simple. The starting equation is Beer-Bouguer-Lambert's absorption law:

$$\overline{I} = I_0 \cdot e^{-\int_0^l \alpha \cdot c_m \cdot dx} \tag{4.10}$$

with α representing the absorption coefficient, c_m the molar vapor concentration and $\mathbf{x}$ the way. Since we consider the vapor concentration to be invariant over the full path length equation 4.10 can be simplified:

$$\frac{\overline{I}}{I_0} = e^{-\alpha \cdot c_m \cdot l} \tag{4.11}$$

Another small change to the formula has to be made since only the decadic absorption coefficient ϵ could be found in literature. This change consists only of replacing α by ϵ and the e-base by a decadic base:

$$\frac{\overline{I}}{I_0} = 10^{-\epsilon \cdot c_m \cdot l} \tag{4.12}$$

Since $\epsilon = 1,1 \cdot 10^4 [\frac{cm^2}{mol}]$ and $l = 50[mm]$ are constant (for this temperature and ambient pressure), the only thing left to do is to determine the molar concentration at saturation point. Knowing the saturation pressure of acetone at 298[K] $p_{sat} = 24.580[Pas]$ the equation for ideal gases can be employed:

$$c \equiv \rho = \frac{p_{sat}}{R_m \cdot T} \tag{4.13}$$

The resulting concentration equals $c_m = 9,921 \cdot 10^{-12} [\frac{mol}{m^3}]$.
Completing equation 4.12 with the values found, a theoretical absorption of the Infrared beam of $\frac{\overline{I}}{I_0} = 0,28$ results.
Considering, that no fine calibration of the setup had been performed so far, this good accordance of theoretical and experimental result proves the functionality of the chosen setup.

4.4 Refinements On The Rig

The test row described confirms the basic functionality of the setup but shows also the potential for refinements of the rig. Although the determined absorption levels are in coherence with theory, the signal is not as stable as desired. Especially the sensitivity to ambient vibrations, which resonance in the main supports and cause displacements between the optical elements, makes reasonable measurements impossible and must be reduced. Additionally, a notable expansion of the laser beams due to diffraction can be observed after the first pinhole.
This section describes the adjustments to the rig which were chosen as reaction to these problems.

4.4.1 Shock damping system

Since sensitivity to ambient vibrations of is identified to be a major influence on the droplet signal's stability, a mechanical decoupling of the test rig is necessary.

Following the basic physics of dynamic systems, the solution of adding extra mass to the test rig in combination with the introduction of adjusted damping elements between rig and base is chosen. To add mass, the wooden board of the leveled experimental table is removed and replaced by a 780x1450x50 $[mm]$ slate of polished marble. Using the density for standard marble blocks $\rho = 2900[kg/m^3]$, the weight gain can be estimated by $150[kg]$ in comparison to the original board. To effectively decouple this load from the vibrations in the stands, four Newport SLM-3A pneumatically adjustable elastomer supports are fixed at the corners between the marble and the stand. By changing the pressure of the internal air chamber of the supports, a wide range of frequencies to be blocked can be chosen.

Figure 4.20: Elastomer shock damping support (Source: Newport)

Test after the installation show a clearly reduced response of the test rig to ambient vibrations. While continuous sources of lower amplitude such as running generators in the building or bypassing traffic are completely filtered, heavy shocks like door slamming or falling object are still transmitted to the optical elements, however, are quickly damped.

4.4.2 Quantification of the beam expansion

As mentioned in the last chapter, an expansion of the - visible - beam due to diffraction at the pinhole can be observed. However, for deconvolution of the measurements results, the hypothesis of a constant beam-cross-section in the investigate zone is absolutely necessary to keep the calculations simple and fast.
To verify if this assumption can be maintained, the theoretic diffraction is calculated by the relation for circular aperture diffraction:

$$sin\Theta = \frac{\mathcal{M} \cdot \lambda}{d} \tag{4.14}$$

or for the displacement

$$y \approx D \cdot \frac{\mathcal{M} \cdot \lambda}{d} \tag{4.15}$$

Equation 4.15 is using the 'approximate' sign since the assumption for small angles $tan\Theta \approx sin\Theta \approx \Theta$ is implied. Table 4.21 shows the calculated first diffraction minima ($\mathcal{M} = 1.22$) for both wavelengths at multiple distances:

distance \ λ	632.8[nm]	3.392[μm]
475 [mm]	1.73	4.94
260 [mm]	1.40	3.14
45 [mm]	1.07	1.36

Figure 4.21: Calculated beam diameter in [mm]

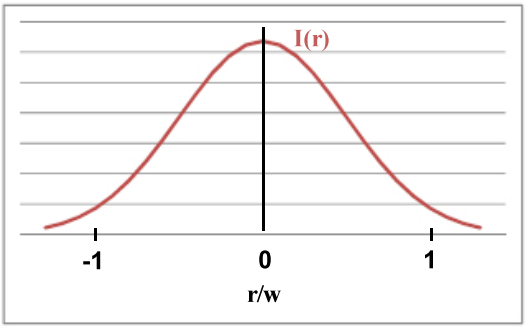

Figure 4.22: Gaussian intensity distribution

The distances in the table above represent the center of the experimental zone (260[mm]) as well as the smallest (45[mm]) and largest (475[mm])distance of the droplet injector to the pinhole which is technically possible . These theoretical values[2] are confirmed experimentally for the visible wavelength. We see, that the expansion of the beams is important. Especially in the Infrared, the distance between the pinhole and the object to be investigated has to be kept as small as possible!
As a consequence, the injector has been moved as close as possible for the experiments. The small size of the droplet and its surrounding vapor field ($\approx 3[mm]$ when heated) allow to contain the assumption of a cylindrical beam. Considering the difference in beam diameter between the two wavelengths at this position, a value of 1.15[mm] is chosen for both. An estimation of the maximal error due to this simplification can be done using the general equation for energy distribution inside a Gaussian repartition as shown in figure 4.22:

$$I_{(r)} = \frac{2 \cdot P}{\pi \cdot w_b^2} \cdot e^{-2\frac{r^2}{w_b^2}} \tag{4.16}$$

with $I_{(r)}$ being the intensity at a given radial position, P the beam power and w the beam width. In our case, the beam power rests constant - since we still regard the full beam - but the width changes with $w_{b-2} > w_{b-1}$. The biggest difference in intensity can be expected in the droplet center at position $r = 0$. Therefore, equation 4.16 can be written as:

$$P = \frac{I_{1(0)} \cdot \pi \cdot w_{b-1}^2}{2} = \frac{I_{2(0)} \cdot \pi \cdot w_{b-2}^2}{2} \tag{4.17}$$

leading to

$$I_1 = I_2 \cdot \frac{w_{b-2}^2}{w_{b-1}^2} \tag{4.18}$$

As a consequence, beam intensity will be overestimated at the beam center by 40% for the Infrared beam and underestimated by 15% for the visible wavelength.

[2]Online Java-applets for diffraction calculations can be found at: http://hyperphysics.phy-astr.gsu.edu/HBASE/PHYOPT/diffracon.html

Chapter 5

Signal Processing

The acquisition chain provides us with experimental values for each measurement point and a calibration file for each series (see chapter 4.2.5). To process this acquainted experimental data into comparable form, an evaluation routine in Matlab has been developed. The first part of this code allows to determine the quality of the measurements by calculating the mean amplitude and the root mean square (RMS) of the data for each measured position. Additionally, a shape correction matrix, which will be applied on the droplet signals later on, is created. The second part extracts an averaged droplet signal and compares it to the results of the theoretical simulation as presented in chapter 3. Finally, the deconvolution of the data is performed to obtain comparable results to the PLIF measurements. Figure 5.1 shows a block diagram of these operations which are detailed in the following sections. A double-framed box indicates output values. Blue boxes indicate operations performed on the calibration data only, orange ones concern only the measurement data while green boxes use information of both files. Batch processing of multiple measurement files linked to the same calibration is possible. In this case the orange and green steps will be performed according to the number of input files.
Since Matlab is treating all data in the form of matrices, the expressions 'matrix','row' and 'column' will be used when operations are discribed.

5.1 Determination of Amplitude and RMS

This step is done for the calibration signal file only. Its purpose is to determine the initial energy level of the beams and the stability - expressed by the RMS - of the signal. While the former confirms the quality of the alignment of all the elements, the second value serves as an indicator for ambient influences such as vibrations or signal noise.
The incoming signal is of TTL shape, non-centered at zero. It consists of three data columns: time and the energy values for the visible and the infrared channel. Since the desired values are of statistical nature and time independent, the following procedures are applied on the two energy channels only. At first, a mean value of the signal is computed. Then, the data is split into two matrices, one containing all the values larger than this average and the other containing all the values below. These two matrices undergo the following process for three iterations:

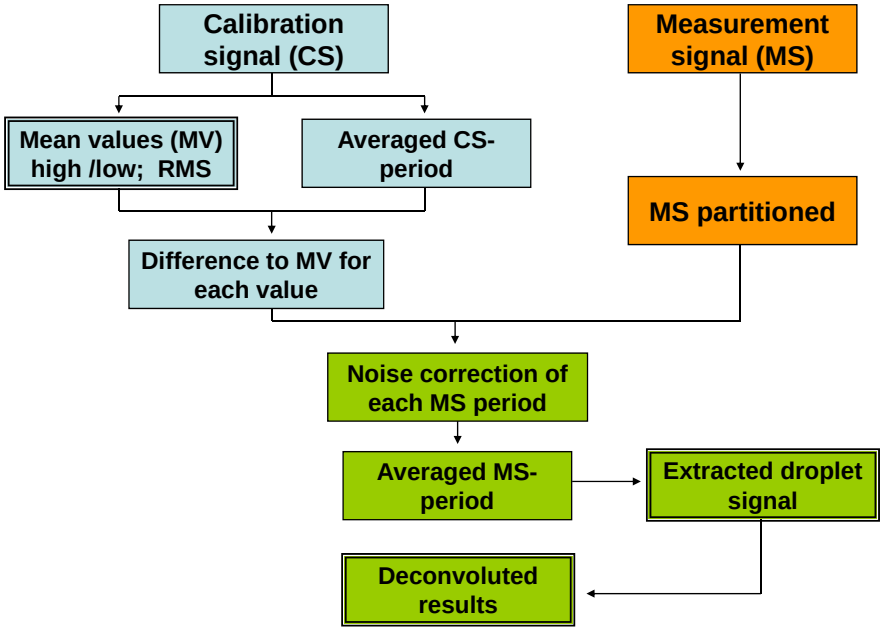

Figure 5.1: Block diagram of the evaluation routine

1. Deletion of all zero-elements of the matrix to obtain the true number of entries.[1]

2. The mean positive and negative value of the signal is obtained by an arithmetic averaging of the form below:

$$\bar{x} = \frac{\sum_{i=1}^{n} x_i}{n} \tag{5.1}$$

3. Using these mean values, the two RMS are calculated as follows:

$$\sigma = \sqrt{\frac{1}{n-1} \sum_{i=1}^{n} (x_i - \bar{x})^2} \tag{5.2}$$

4. As a last step, it is verified for each value of the data matrices if its difference to the respective mean value (positive or negative) is inside the chosen confidence interval:

$$|x_i - \bar{x}| \leq |f \cdot \sigma| \tag{5.3}$$

'f' represents the shape factor of the confidence interval and can be chosen at the start of the program. If the above condition is fulfilled, the value is accepted to the next iterative step. Otherwise it will be discarded.

[1]Since the signals are not zero-centered and the precision of the values is 8 digits behind the comma, no falsification of the true value by this measure has to be feared.

After the third iteration, the mean amplitude $Amp = \bar{x}^{(3)}_{pos} - \bar{x}^{(3)}_{neg}$ and the Root Mean Square $RMS = \sigma^{(3)}_{pos} + \sigma^{(3)}_{neg}$ are computed and shown on the screen. This allows the user to terminate the process at this point in the case of insufficient signal quality.

5.1.1 Creation of a shape correction matrix

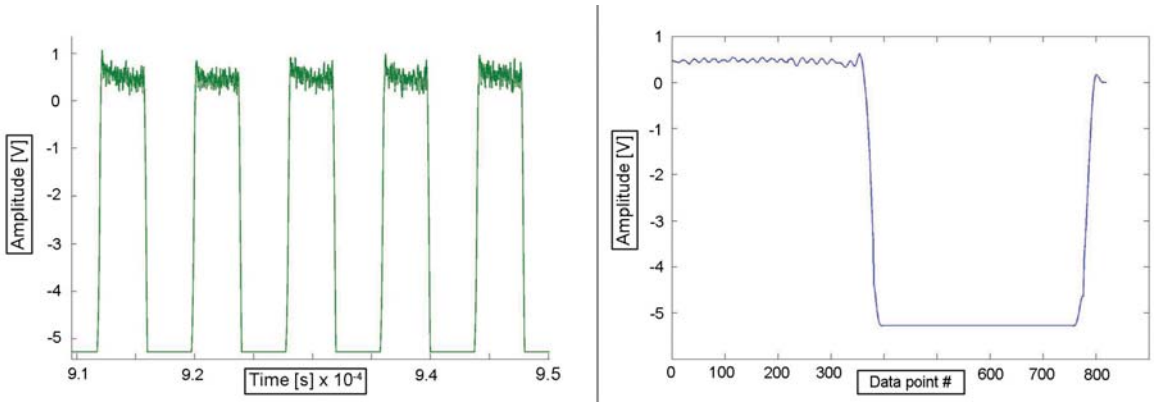

Figure 5.2: Signal shape correction **Left:** sample of the incoming signal, **Right:** corrected mean period

Due to the characteristics of the pre-amplifiers, the stored TTL signals often resemble rather Trapezoids than the ideal square signal (see figure 5.2 a)). Together with some unavoidable signal noise, these systematical deformations would significantly alter the results of the droplet measurements if not removed. For this reason, a correction matrix is created out of the statistical values given by the calibration data. All steps described below are performed for each data column - except the time line - of the measurement files:

5.1.2 Preparation of the experimental data

The correction matrix will be extracted from the average deformations over all the chopper periods. For that the first step is to obtain an averaged chopper period. Since the recording trigger is not sufficiently exact to start the data acquisition for every measurement at the same chopper position, the signal will contain parts of a chopper period at the beginning and/or the end. To assure a smooth averaging, these fragments are removed as described below:

1. The first maximum after the first rising flank of the signal is identified and its position saved.
2. The first maximum after the rising flank of the second chopper period is identified and its position saved.From these two positions, the number of data points per chopper period 'n_p' is computed.
3. Now the length of the whole signal is divided by this value to obtain the number of complete chopper periods per signal, 'C_{ps}'.

4. As a last step all values before the first identified maximum and after position $n_p \cdot C_{ps}$ are discarded.

The result of this procedure is a signal only containing whole chopper periods of data. Knowing the length of one period it can easily be averaged to obtain a mean chopper period signal.

5.1.3 Determination and application of the correction

To determine the necessary correction the 'positive' and 'negative' average values as used for the calculation of the signal amplitude in the chapter above are employed. Each point of the mean chopper period is compared to its respective average value. The difference for each position is stored in a separate matrix, the 'shape correction matrix'.
The correction of a noisy signal period can now be achieved by element wise subtraction of this matrix. An example of the result is shown in figure 5.2 b).

5.2 Extraction of droplet signals

After having obtained all the necessary information from the calibration file, the actual extraction of the droplet signals from the measurement files. Figure 5.3 gives a schematic view of the extraction process described in detail further below:

5.2.1 Preliminary actions

The preconditioning of the measurement data is effected in the same manner as described earlier for the calibration file. The only difference consists in the shape correction of each chopper period before (!) the averaging. The combination of averaging and shape correction assures a maximum suppression of random and systematical signal deformation. These procedures are illustrated by the images from top left to bottom left in figure 5.3.

5.2.2 Harmonization of the droplet signals

Before a single droplet signal can be extracted by another averaging process (transition image bottom left→ bottom right in figure 5.3) the droplet signals have to be harmonized. Since the acquisition happens at frequencies of several hundred kilohertz, already small variations in droplet spacing or droplet velocity cause different numbers of acquisition points per droplet signal. This is unfavorable for the envisaged averaging. Therefore a reconstruction of the droplet signals by interpolation is performed.
Since the characteristic bumps caused by the droplets only appear on the positive flank of the TTL signal only this part will be processed. The first step is the identification of all the maxima in this selected region. Apart from an easily distinguishable peak caused by the amplifier at the beginning of the flank, these maxima represent the number of droplets that passed the laser

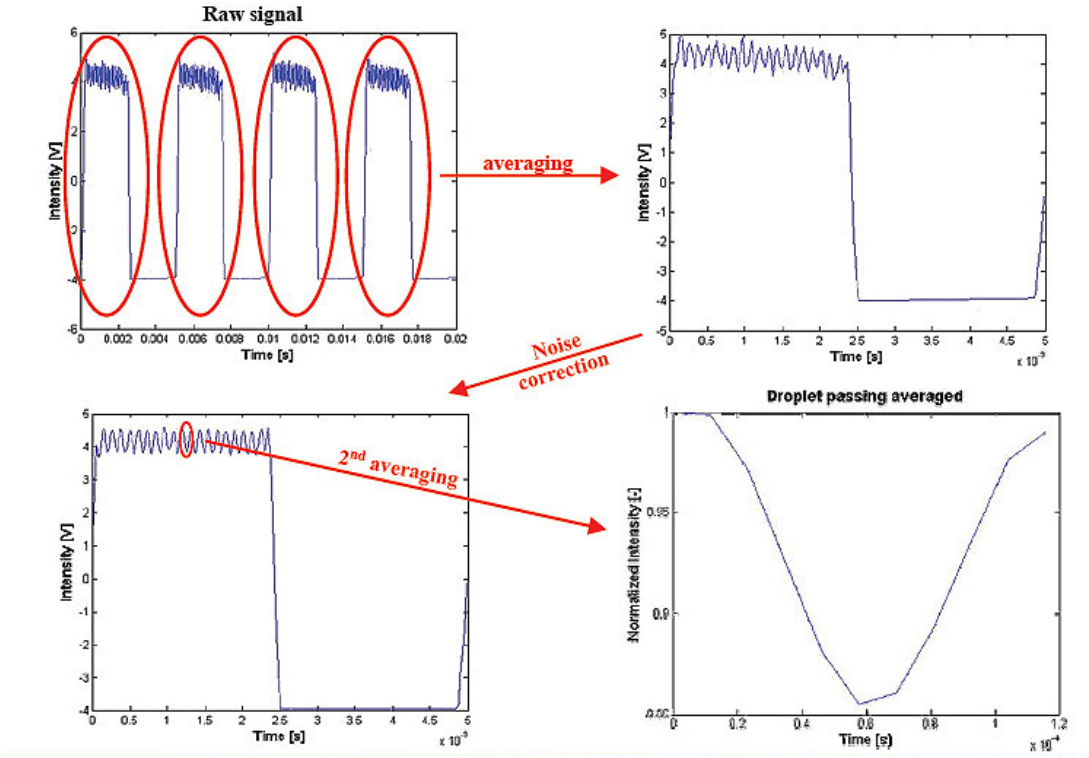

Figure 5.3: Scheme of the droplet signal extraction

beams during a chopper period. For that, the effective time between the passing of the first and the last droplet in this period can be calculated as the time difference between the last and the second maxima:

$$T_{pass} = t_{nmax} - t_{n2} \tag{5.4}$$

With this information and the known acquisition frequency the theoretical average number of acquisition points per droplet signal can be derived:

$$np_{th} = \frac{T_{pass} \cdot f_{acq}}{n_{max} - 2} \tag{5.5}$$

Because of the small alteration mentioned in the preface of this section the value for np_{th} is no integer. To harmonize the number of acquisition points per droplet signal, the next higher integer to this value is selected as number of reconstruction points.

$$np_{new} = int\,(np_{th}) + 1 \tag{5.6}$$

$$\Delta t = \frac{T_{pass}}{np_{new} \cdot (n_{max} - 2)} \tag{5.7}$$

Δt represents the time difference between two reconstruction points. With its aid the new points are uniformly repartitioned in the droplet signal. The value of these points is computed

by linear interpolation between the neighbouring acquisition points. Figure 5.4 shows a scheme of this process.

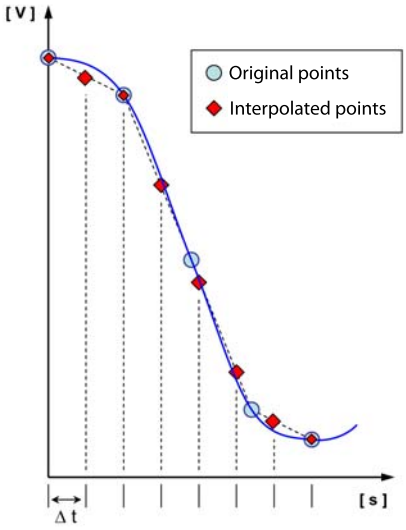

Figure 5.4: Reconstruction of the droplet signal

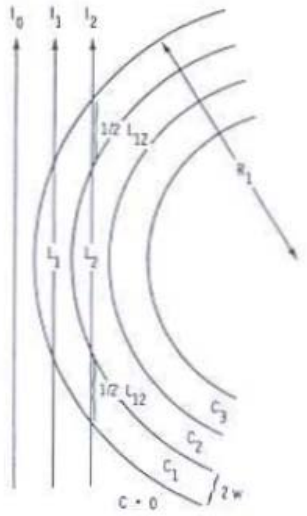

Figure 5.5: Repartition of the vapor field (Source: [7])

As a last step the reconstructed droplet signals are averaged to obtain a mean signal which can be compared to the theoretical results (see chapter 3).

5.2.3 Comparison to the simulation

The simulation of the respective experimental case is embedded in the program as a function. At the starting point, the main calculation parameters such as beam diameter, temperatures and droplet characteristics are passed on from the experimental data. The simulation result is returned as a single matrix ready to be compared to the experiments. It has to be noted, that, since the simulation only computes the case of the droplet passing exactly at the beam center so far, the comparison to different experimental positions will lead to wrong results! On the other hand, this fact can be used to verify the alignment of the injector. Examples for the comparison of the simulation to experimental results can be found in chapter 7.1.

5.3 Spatial deconvolution

Since the IRE is a line-of-sight-type technique, the obtained results are integrated over the whole length of the measured area. To get spatially resolved results, deconvolution procedures have to be applied to the data. One of the classic deconvolution schemes for axisymmetrical geometries such as sprays or spherical objects is the 'Onion-peeling-scheme' as presented by Hammond 1980 [59]:

5.3.1 The classic 'Onion-peeling'-scheme (OPS)

This technique represents a basic Abel transformation as described in detail in **??**.Its idea is to divide the (axisymmetric) spray/vapor field into concentric rings of equal width w in which the concentrations are assumed constant (Figure 5.5). A series of line-of-sight measurements on various radial positions, $I_1 ... I_n$ can be deconvoluted to provide local concentrations with a resolution of $\approx w$. The system of equations can be developed the following way:

$$c_{m-1} = -\frac{1}{l_1 \cdot \alpha} \ln \frac{I_1}{I_0} \tag{5.8}$$

$$c_{m-2} = -\frac{1}{l_2 \cdot \alpha} \left(\ln \frac{I_2}{I_0} + \alpha \cdot l_{1,2} \cdot c_{m-1} \right) \tag{5.9}$$

$$\dots$$

$$c_{m-n} = -\frac{1}{l_n \cdot \alpha} \left(\ln \frac{I_n}{I_0} + \sum_{i=1}^{n-1} \alpha \cdot l_{i,n} \cdot c_{m-i} \right) \tag{5.10}$$

The lengths l_{in} can be determined trigonometrically. In the end we obtain a system of n equations for the n unknown local concentrations. These can be solved beginning from the outermost ring until the center.
To validate this reconstruction technique two test cases, a straight cone and a half-ellipsoid, are investigated (figure 5.6).

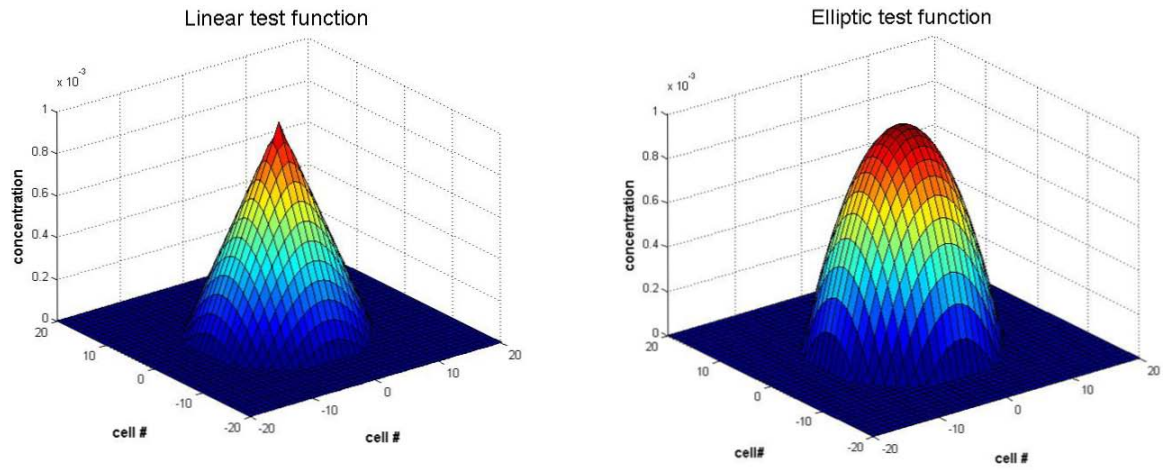

Figure 5.6: Test cases for the Onion-Peeling scheme

These geometries both consist of continuous curves which are rotated around an axis perpendicular to the base plane. For this reason it is simple to extract one of these generating lines and to compare it to the deconvoluted results.
As a first step, the test functions are implemented as a vapor matrix in the absorption simulations as described in chapter 3.4. The width of the laser beam and the step-size are chosen to equal one cell-width of the matrix, leading to one 'measurement' per cell. Figure 5.7 shows the resulting absorption profiles for both test cases:

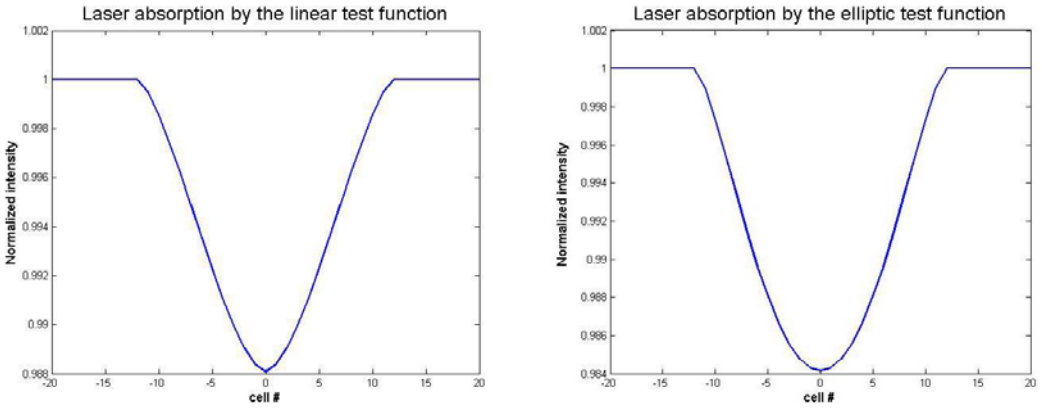

Figure 5.7: Absorption profiles of the test cases

The similarity of these two curves indicates, that the main influences on the shape are the axisymmetry of the concentration field and the circularity of the beam. However, clues for the different test cases can be found in the straighter flanks for the linear case (cone) and the higher absorption due to the higher volume of the elliptic case.
These curves represent the basis for the following deconvolution process. Due to axisymmetry only the left half of the absorption profiles is used for reconstruction.

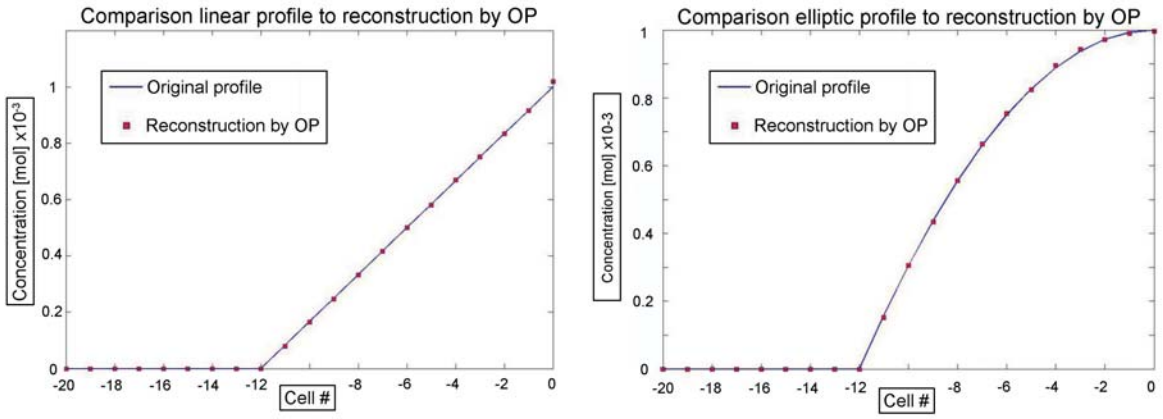

Figure 5.8: Comparison of the reconstructed values to the original profiles

As we can see in figure 5.8, there is very good accordance between the original profiles and the values obtained by Onion-Peeling. Especially for the linear profile of the conical test-case, errors are only detectable right after the beginning of the cone (cell '-11') and at its top (cell '0'). While the former one is very small and can be neglected, the latter is quite important. This is due to the fact, that the top of the cone represents a singularity. Such sudden changes of the concentration gradient can cause the Onion-Peeling scheme to oscillate heavily before reaching the true level.
A smoother occurrence of this effect can be observed at the results for the elliptic test case: The value at cell '-11' shows the same underestimation of concentration as in the linear test case. After stabilization in the range from '-10' to '-6' the gradient of the profile increases. At the

same time, the reconstructed values begin to oscillate slightly around the original values (cell '-5' to '-1'). Due to the smooth top of the ellipsoid this effect is dampened again and unlike the conical case, an exact value for the center position is obtained.

Conclusion of the comparison:

The Onion-Peeling scheme has been tested on a conical and an elliptic test case. Results show good accordance to the original values except at singularities. Additionally a tendency of the OP to oscillate at stronger concentration gradients has been observed. However, due to the small amplitude of these oscillations and the fact, that in typical vapor concentration profiles no singular points occur, is this technique chosen to deconvolute our line-of-sight integrated results. The advantages of this technique are obvious: Its a simple and robust mathematical model that allows deconvolution at a resolution down to one beam diameter at very low computational cost. On the other hand, there are two main inconveniences: Errors, that occur at every measurement, are summed up in the direction of the center. This often leads to relevant uncertainties for the core values of the investigated field. Second, this simple system of equations is only valid using two major assumptions: perfect axisymmetry of the spray/vapor field and a beam diameter that is much smaller than the spray diameter $D_{beam} << D_{spray}$. If the second condition is not fulfilled, the choice of a single traversing length is physically not legitimate anymore and, additionally, the intensity profile of the beam has to be taken into account! An attempt to expand this technique to situations where $D_{beam} \approx D_{spray}$ is described in the next section.

5.3.2 Application of the OPS on the droplet stream

As mentioned in the last section, the biggest difference in deconvoluting the results of a droplet stream to those of a spray configuration is the relative size of the laser beam. In the present experimental configuration, the vapor tunnel measures between 9 and 12 droplet diameters in radius, which result in $\approx$ 2.1 and 2.9 mm or 1.5 and 2.08 mm for droplets of 238 and 173 μm diameter respectively.

Principle and assumptions

1. cylindrical beam with Gaussian energy distribution
2. fully developed vapor tunnel without axial fluctuations around the droplets $\rightarrow$ concentration profile varying in radial direction only
3. vapor tunnel approximated by a cuboid with one symmetry plane along the droplet propagation axis.

Assumption one is justifiable since the droplet stream is placed right after a pinhole which smoothes the beam profile. Point two can be accepted for the horizontal vapor profile, since the deconvolution will be performed until the distance of one droplet radius from the axis only. In

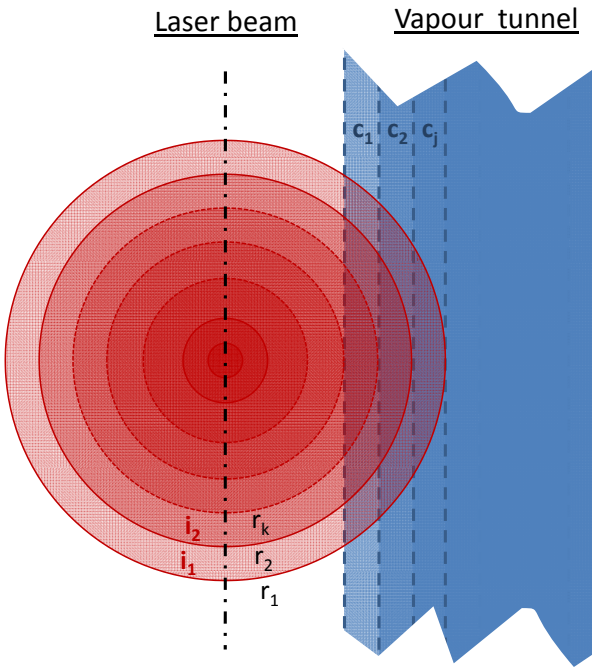

Figure 5.9: Scheme of the deconvolution system after the simplifications

this region, the vapor concentration is already very uniform in axial direction, as we can observe at the vapor fields calculated by B.Frackowiak (chapter 3.2.1).
The third simplification, is a very strong assumption and significantly different from the real configuration. However, it is absolutely necessary to avoid very difficult geometric calculations: In reality, the step wise superposition of the laser beam and the vapor tunnel corresponds to the geometric intersection of two perpendicular cylinders. Therefore, the counterpart to the absorption length in the classic OP scheme becomes a volume, confined by surfaces of the 4^{th} order. Additionally, the partitioning of both cylinders and the fact, that each intersection volume has to be recalculated for each step of superposition has to be taken into account. This sums up to very delicate and costly calculations.
Figure 5.9 shows that by applying all off the simplifications mentioned above, this problem can be reduced to the calculation of 2D surfaces. The following chapter describes the development of this simplified '2D-Onion-Peeling-Scheme'.

Local energy values of the partitioned laser beam

Similar to the repartition of the vapor field into concentric rings of equal concentration in the classic OP-scheme, the laser beam is segmented into rings of equal intensity. To determine the amount of intensity per ring - or, later on, of the intersection of ring and vapor field - the infinitesimal intensity '$int_{(r)}$' is introduced. It represents the intensity of an infinitely small surface element at position r. When assuming a Gaussian distribution of the beam intensity, $int_{(r)}$ depends on the total beam intensity, 'I_0', r and the beam width 'w_b':

$$int_{(r)} = \frac{2 \cdot I_0}{\pi \cdot w_b^2} \cdot e^{-2\frac{r^2}{w_b^2}} \tag{5.11}$$

As the intensity value is assumed to be constant over the width of each ring, a mean value for $int_{(r)}$ inside these limits can be simply multiplied by the ring surface to determine its intensity value.

$$I_k = \overline{int_k} \cdot A_k \tag{5.12}$$

The same procedure can be applied to obtain the respective intensities for the intersection surfaces of vapor tunnel and beam:

Determination of the intersection surfaces

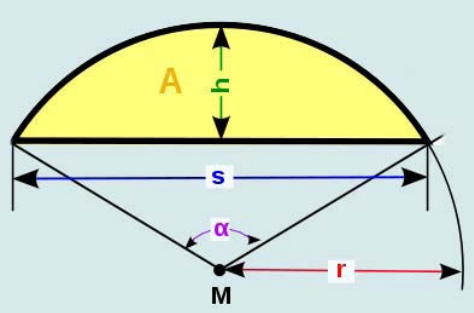

Figure 5.10: Circular segment

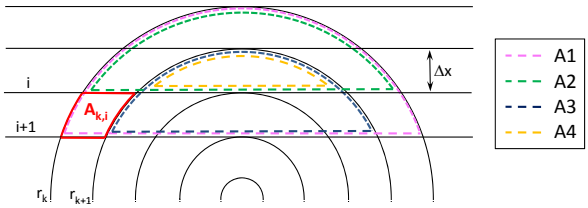

Figure 5.11: Determination of non-centered surfaces

The intersection of a disc and a square greater than the disc diameter results in a circular segment as shown in figure 5.10. Its surface can be expressed, depending on radius and height only:

$$A_{seg} = r^2 \cdot \arccos\left(1 - \frac{h}{r}\right) - \sqrt{2 \cdot r \cdot h - h^2} \cdot (r - h) \tag{5.13}$$

In our case, all the centered intersection surfaces - except for the center disc - are calculated using this expression. The first index indicates the ring, which contains this surface, and the second stands for the position of the intersection:

$$A_{k,k} = r_k^2 \cdot \arccos\left(1 - \frac{\Delta x}{r_k}\right) - \sqrt{2 \cdot r_k \cdot \Delta x - (\Delta x)^2} \cdot (r_k - \Delta x) \tag{5.14}$$

The non-centered surfaces can be obtained by subtracting several of these segments. Figure 5.11 illustrates the development of the following general expression:

$$\begin{aligned} A_{k,i} &= \overbrace{A_{seg}\left(r_k;(k-i+1)\cdot\Delta x\right)}^{A1} - \overbrace{A_{seg}\left(r_k;(k-i)\cdot\Delta x\right)}^{A2} - \\ &- \underbrace{A_{seg}\left(r_{k+1};(k-i+1)\cdot\Delta x\right)}_{A3} + \underbrace{A_{seg}\left(r_{k+1};(k-i-1)\cdot\Delta x\right)}_{A4} \end{aligned} \tag{5.15}$$

Using these two expressions all surfaces on the right hand side of the beam can be calculated until the last intersection position before the beam center. To determine the remaining areas, centered on the vertical symmetry line of the beam, the above equations have to be modified. The term 'K' indicates the total number of rings, in which the beam has been divided, and is therefore a constant. Consequently, $A_{K,K}$ describes the surface of the innermost disc, contrary to $A_{k,k}$ used above, which only indicates a surface centered on the horizontal axis:

$$\begin{aligned} \frac{A_{K,i}}{2} &= A_{seg}\left(r_i;(K-i+0.5)\cdot\Delta x\right) - A_{seg}\left(r_i;(K-i)\cdot\Delta x\right) - \\ &- A_{seg}\left(r_{i+1};(K-i-0.5)\cdot\Delta x\right) + A_{seg}\left(r_{i+1};(K-i-1)\cdot\Delta x\right) \\ A_{K,K} &= r_K^2\cdot\pi \end{aligned} \tag{5.16}$$

Due to symmetry, the surfaces on the left hand side of the beam are equal to their respective counterparts on the right hand side. As a consequence they are not calculated separately.

Algorithm of deconvolution

Knowing the local intensities and the possible intersection surfaces, an expression for the total beam intensity after absorption, '$\bar{I}$' can be developed. At partial intersection with the vapor tunnel, some surfaces will be subjected to absorption following Beer-Lambert's-law, while other rest unaffected. For the initial state of only one step of intersection (j=1) we can write, using the same system of indices as above:

$$\bar{I}^{(1)} = int_1\cdot e^{-\alpha\cdot c_1\cdot l}\cdot A_{1,1} + int_1\cdot(A_1 - 1_{1,1}) + \sum_{k=2}^{K} A_k\cdot int_k \tag{5.17}$$

The first term on the right hand side of the equation represents the part of ring 1 subjected to absorption by the outermost concentration of the vapor tunnel,c_1. The unaffected part of ring one is described in the second term and the sum indicates the intensity of all the inner rings with their respective local intensities.
When advancing one position, two rings intersect two concentration levels, resulting in three affected surfaces:

$$\begin{aligned} \bar{I}^{(2)} &= int_1\cdot\left(e^{-\alpha\cdot c_{m-1}\cdot l}\cdot A_{1,2} + e^{-\alpha\cdot c_{m-2}\cdot l}\cdot A_{1,1}\right) + A_1 - (A_{1,2}+A_{1,1})) + \\ &+ int_2\cdot\left(e^{-\alpha\cdot c_{m-1}\cdot l}\cdot A_{2,2} + A_2 - A_{2,2}\right) + \sum_{k=3}^{K} A_k\cdot int_k \end{aligned} \tag{5.18}$$

Continuing this scheme, we arrive at following general expression for $\bar{I}^{(j)}$:

$$\bar{I}^{(j)} = \sum_{k=1}^{j} int_k \cdot \left(A_{k,k} + \sum_{n=1}^{j-k+1} \left[A_{k,j+1-n} \cdot e^{-\alpha \cdot c_{m-n} \cdot l} - 1 \right] \right) + \sum_{k=j+1}^{K} A_k \cdot int_k \tag{5.19}$$

The equation above leads to a quadratic system of equations with j equations for j unknowns,c_{m-n}. Since only one solution per unknown exist, it can be easily solved to obtain the wanted concentration profile of the vapor tunnel.
Strictly speaking, equation's 5.19 validity ends when the superposition reaches the center of the laser beam. Although the further surfaces and local intensities are equal to their counterparts in the first half of the beam, the system of indices has to be changed to avoid invalid expressions (p.ex.: K=6, j=7 $\rightarrow$ k=1..7 $\rightarrow$ A(7,7) does not exist since $k \overset{!}{\leq} K$). However, this change is not trivial because of the linkage between j,k and n.
A simple solution for this problem is to expand the range of the affected variables by mirroring the symmetrical values:

$$A_{(1..K)} = [A_1, A_2, \ldots, A_K] \Longrightarrow A_{(1..2 \cdot K-1)} = [A_1, \ldots A_{K-1}, A_K, A_{K-1}, \ldots, A_1] \tag{5.20}$$

In this way, equation 5.19 can be used until the whole beam diameter is superposed with the concentration field (j = 2K-1). If the vapor field is even wider, so that the beam enters completely ($j > 2k-1$), the indices to be finally modified. In this case, the expressions for the two sides of the beam rest as described above but for two changes:

$$\sum_{k=j+1}^{K} A_{2k-j} \cdot int_k = 0 \tag{5.21}$$

$$int_{[1:j]} \rightarrow int_{[(j-2K+1):j]} \tag{5.22}$$

The first alteration is the elimination of the last sum. This step is not absolutely necessary to keep the system functioning, but since all the values in the sum equaled zero if the beam is completely inside the vapor field, this term is not necessary anymore. The second correction ensures, that the absorption is calculated with the right concentration values. With these two modifications, the system of equations is valid until the outermost ring of the beam reaches the droplet surface. For further cases no investigations have been made.

Application on test cases

Considering the assumption of a square vapor field, the test functions have to be modified accordingly. Figure 5.12 shows the resulting test concentration profiles for the 2D deconvolution

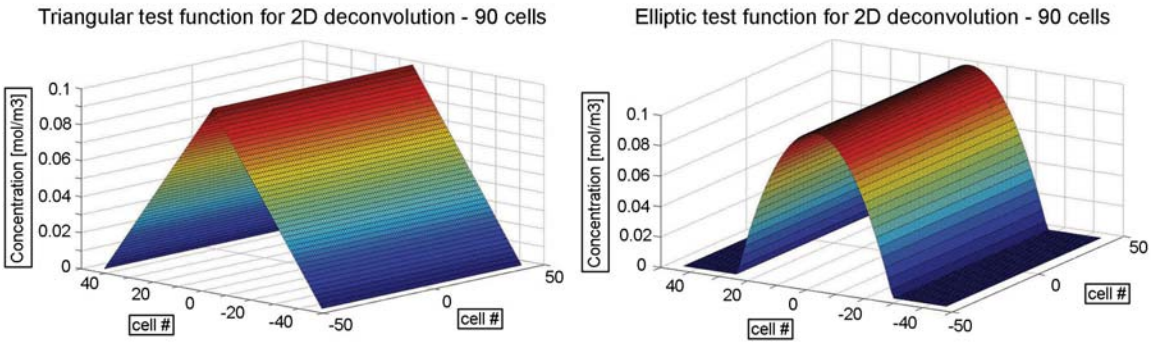

Figure 5.12: Test cases for the 2D deconvolution. **Left:** Triangular test case; **Right:** Elliptic test case

at a resolution of 90 cells per dimension. Again, a triangular and a elliptic profile are chosen. This time, the steady slope of the first test profile is set to start directly at the border of the simulation. The goal of this change is to investigate, if the oscillating behaviour observed at the regular OP-scheme appears at concentration gradients, which start right from the beginning, too. Since this algorithm is more complex as the 1D-case, the influence of grid resolution is also investigated. For this reason, additional test profiles of the same shape were created using 20 and 200 cells per dimension.

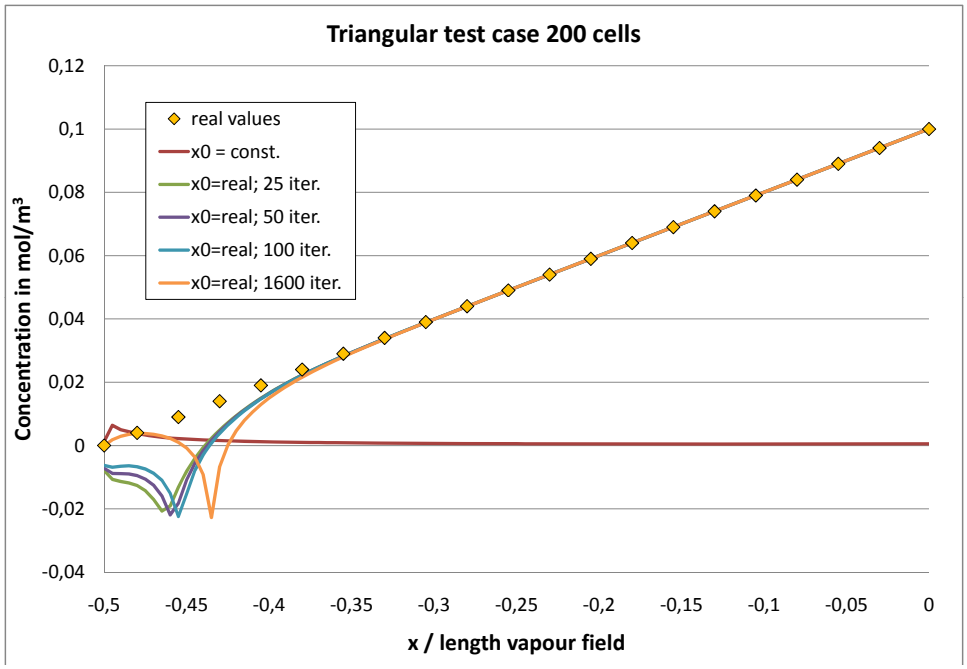

Figure 5.13: Deconvoluted results for the Triangular test case at 200 cells per dimension

The first comparison is done on the highest spatial resolution of 200 cells per direction. For the triangular case, presented in figure 5.13, we observe a good agreement of the deconvoluted

concentrations to the original values in the last two thirds of the profile. The left hand side, from to border until position -0.4 is dominated by some kind of transient effect of the algorithm, resulting in a sharp negative peak. Since the computation does not yet converge at the low number of 50 iterations originally chosen,the number of iterations is successively increased from 25 to 1600 to determine, if this disturbance is due to numerical residues. The development of the profile indicates a narrowing of the peak for a higher number of iterations. At the same time the estimation of the first concentration value ameliorates. However, the point where the true values are achieved stays the same. It has to be noted, that in spite of the high number of iterations, this is still no convergent solution! A possible reason for this lack of convergence is given later in this chapter. Because of the high computation time, no investigations beyond these 1600 iterations are done yet.
An even more important influence on the results of this deconvolution approach than the number of iterations is the choice of the initial concentration values. The results discussed above are all obtained with an array of initial concentration values with a difference of less than one percent to the respective true ones (therefore labelled 'x0=real' in the graph). For every other tested combination of initial values the iteration process lead to convergence far off the true profile. The dark red line labelled 'x0=const.' gives an example of the results if the initial concentration profile is given by the same value for every position. This asymptotic approximation to zero can be observed for every constant value between zero and one, with the height of the initial peak being the only difference.

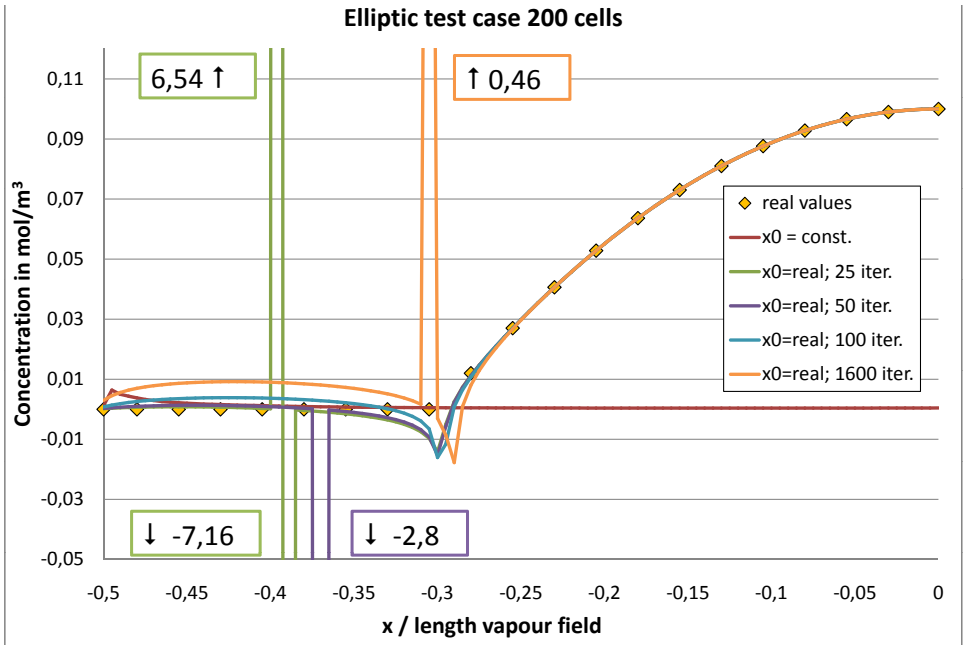

Figure 5.14: Deconvoluted results for the Elliptic test case at 200 cells per dimension

The elliptic case, presented in figure 5.14, shows similar behaviour. However, it can be observed, that the peak described before, seems to be connected to the sudden change in concentration rather than to a transient effect at the beginning of the iterative process. Therefore,

it represents the 2D-counterpart to the oscillations identified at the classic OP scheme. This error also influences the results in the outer regions of the concentration field. Right (inside, spoken in terms of the vapor field) of the peak the deconvoluted results show good agreement with the real ones. On the left hand side, however, significant errors appear as heavy oscillations (25,50 and 1600 iterations) or propagate until the outermost value (100 and 1600 iterations).
In case of initial concentration values different from the profile which is to be expected, the same behaviour as for the triangular case appears (red line).

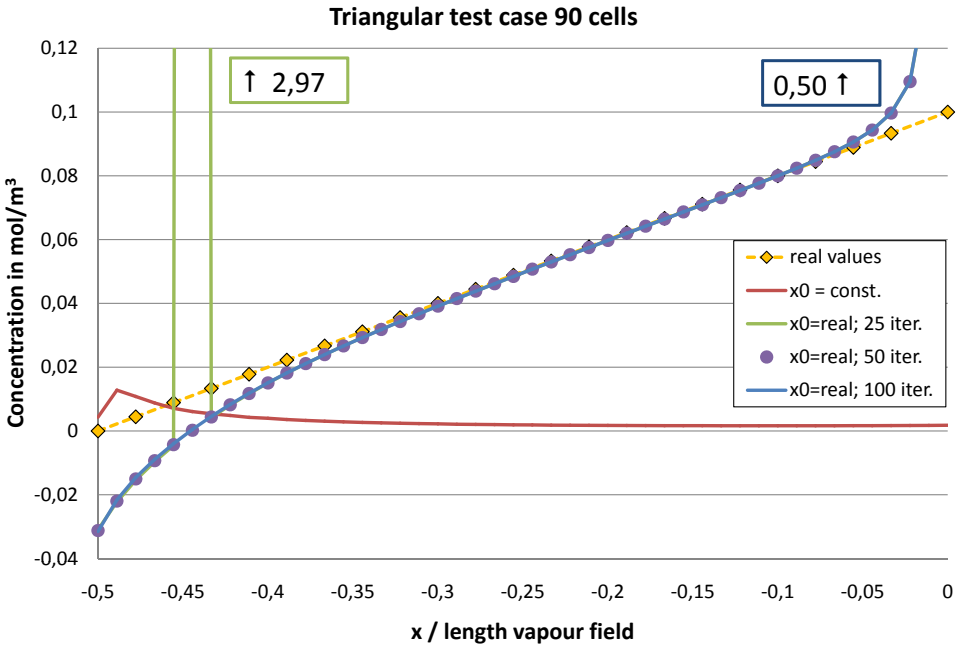

Figure 5.15: Deconvoluted results for the Triangular test case at 90 cells per dimension

Further comparisons are made for the same two test cases at 90 and 20 cells per dimension respectively. The influence of the reduced spatial resolution is found to be significant, as shown for the Triangular test case in figure 5.15. Severe differences to the true concentration values appear at the border and the center of the vapor field for all numbers of iterations. Only the intermediate region is well reconstructed by the deconvolution scheme. At this lower resolution, the numerical oscillations, caused by the change in the concentration gradient, already dominate the two edges. Also isolated error peaks appear at lower numbers of iterations.
These effects suggest that the number of 90 cells is just below the application limit for this technique on the present test case. The results for the elliptic test case at the same resolution and for both cases at 20 cells per dimension confirm this assumption (figure 5.16). In these latter configurations, the number of cells is not large enough anymore to dampen the oscillating effects, leading to iterative results that have nothing in common with the true repartition of concentration. The fact, that for 20 cells only a small difference in shape rests between the results for the two test cases, shows, that this development is entirely due to inaccuracies of the algorithm.

Main source for this defective behaviour is the determination of the local beam energy values

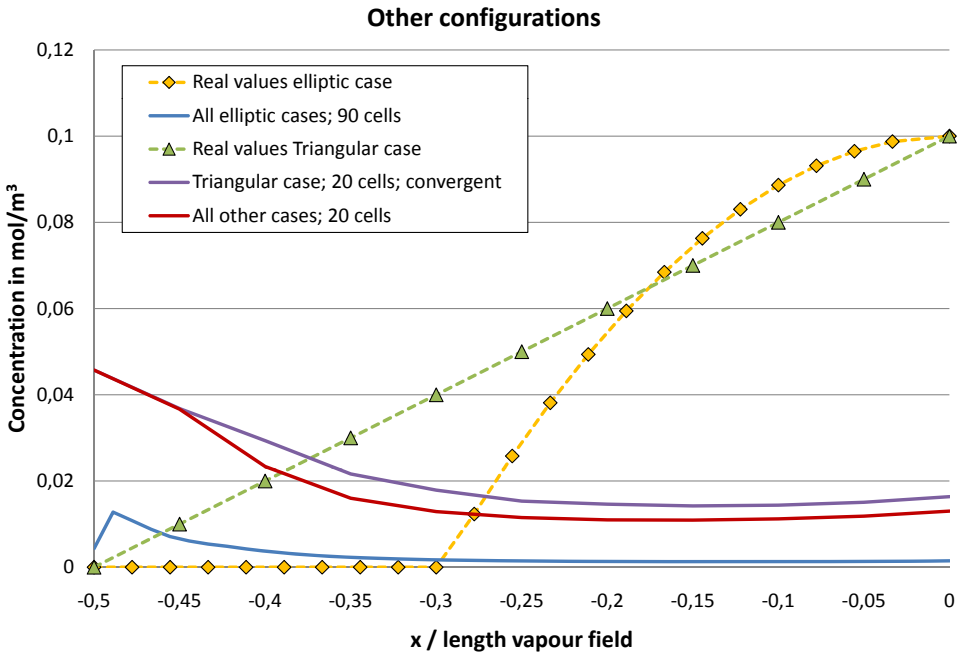

Figure 5.16: Deconvoluted results for other cases at lower cell numbers

int_k. Since the Gaussian energy distribution has to be discretized into rings of a given width, each local value differs from the real integral over the Gaussian profile (figure 5.17). The result is a difference in the beam energies determined by summation of these values and the true one, employed to calculate the absorption profile which is deconvoluted. In the present test, a high number of cells corresponds to a small ring width and vice versa. Therefore, the errors for each intensity get the more important, the lower the cell number. Tests show, that for the Triangular test case a minimal number of 110 cells, and 150 cells for the Elliptic test case respectively, are recommended to obtain reasonable results (Initial concentration values close to the real ones assumed!).

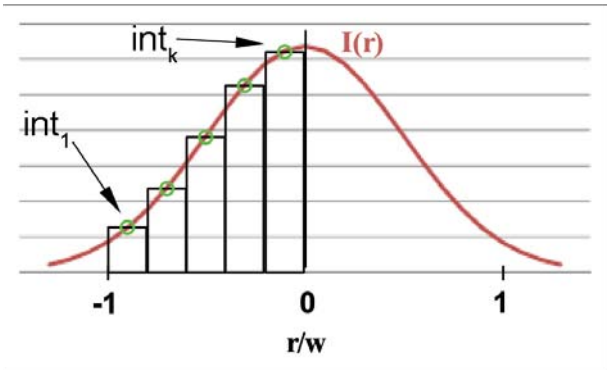

Figure 5.17: Discretization of the beam energy

Regarded from the experimental point of view, each ring/concentration value represents one measurement position. This makes the practical application of this deconvolution scheme in the present state very time consuming and difficult. Especially for the present experiments, a repartition of the laser beams (diameter 1.15 mm) into at least 110 cells would result in a distance of approximately $10\mu m$ between the measurement points. To achieve this accuracy, a high precision mechanical displacement system is necessary and a large number of measurements per positions would have to be made to account for natural fluctuation of the droplets due to turbulences in the entrained air flow.

Chapter 6

Application On A Spray Configuration

6.1 Motivation for the application on a spray

Despite its many points of interest for the development of the Infrared Extinction Technique, the monodisperse injector is a strictly academic configuration. For results closer to industrial conditions, an application on a fuel injector system, or an confined or unconfined conic spray is desirable. In fact, most of the authors dealing with the IRE, start directly at spray configurations, also because of the advantages concerning the deconvolution of the integral results as described in chapter 5.3 [7, 8, 46, 10, 38, 39, 44, 33]. Although the main subject of this thesis rests the application of the IRE on monodisperse droplets, complementary results on a known spray configuration are of interest for the development of the test rig.

Simultaneously to the development of the IRE another optical measurement technique for spray characterization, Global Rainbow Refractometry (GRR) is investigated at ONERA. A team around Bodoc and Wilms refines this technique, experimentally as well as through numerical simulation, to characterize open and confined sprays in detail. Since their experimental setup, consisting of PDA and GRR, is capable of investigating the liquid phase of a spray only. Therefore, a possibility to complement their experimental data with information on the vapor concentration was met with interest.
The following chapter is an extract of the works of Bodoc et al. [17, 16, 60]. It covers the basic principle of the investigation technique used, describes the experimental setup and presents the results for spray parameters that are relevant for the collaboration with the IRE technique. For further details please refer to the sources given in brackets above.

6.2 Spray characterization

6.2.1 Setup and measurement techniques employed

Rainbow refractometry consists in analysing interference patterns diffused by a laser lighted droplet. The rainbow phenomenon appears when a droplet crosses an incident parallel light beam (sunbeam or laser beam). In the nature the rainbow phenomenon occurs when the human observer looks at the rain, with the sun shining at its back (Figure 6.1 left). Two rays can be defined. The first connects the observer and the cloud of droplets, while the second relies the sun and the same cloud of droplets. The magnitude of the angle between these two rays is a function of the droplets refractive index (temperature) and size distribution. As for the different colours in the rainbow, they are the expression of the dependence of the refractive index on the wavelength of the incident light. In laboratory, a laser replaces the sunlight beam and different experimental set-ups can be developed to investigate isolated droplets, monodisperse droplet streams and polydisperse sprays (Figure 6.1 right).

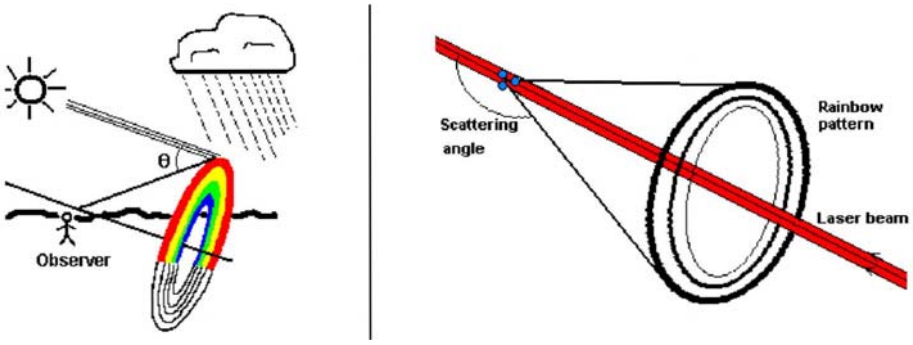

Figure 6.1: **Left**: Natural rainbow; **Right**: monochromatic rainbow formation under laboratory conditions

When a single droplet is concerned (Standard Rainbow Refractometry technique) the backward diffusion pattern is mainly created by the superposition of two interference patterns: the Airy fringes and the ripple structure (Figure 6.2). The last results from the optical interference between the once internally and once externally reflected light. The angular position of the 1st order rainbow depends especially on the droplet refractive index (and consequently its temperature) and the droplet shape.

Applied to a cloud of droplets, the technique is known as Global Rainbow Refractometry (GRR) or Global Rainbow Thermometry (GRT). The basic principle of the GRR technique is the summation of the rainbow signals corresponding to droplets of different shapes, dimensions and temperatures. In order to perform measurements on these parameters, and to combine them with velocity informations, an experimental setup was developed at ONERA (Figure 6.3).

The polydisperse spray is generated with an ultrasonic atomizer. The size distribution and the spray expansion are controlled by the amplitude and frequency of the exciting generator,the

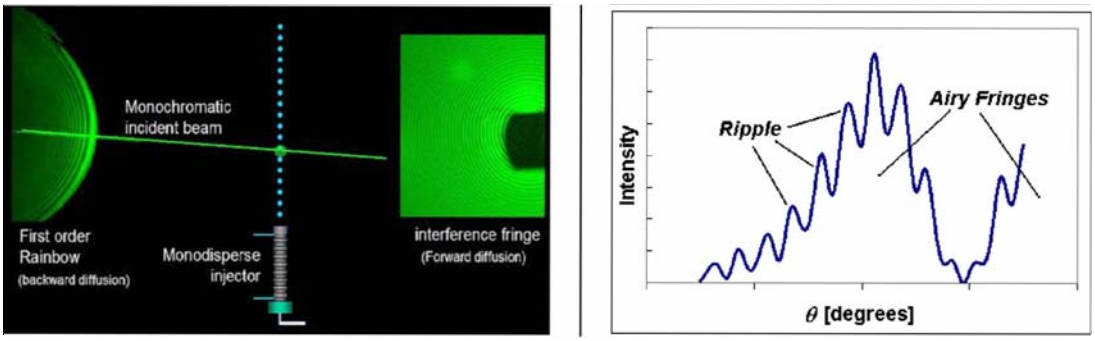

Figure 6.2: Scattered light around an individual droplet

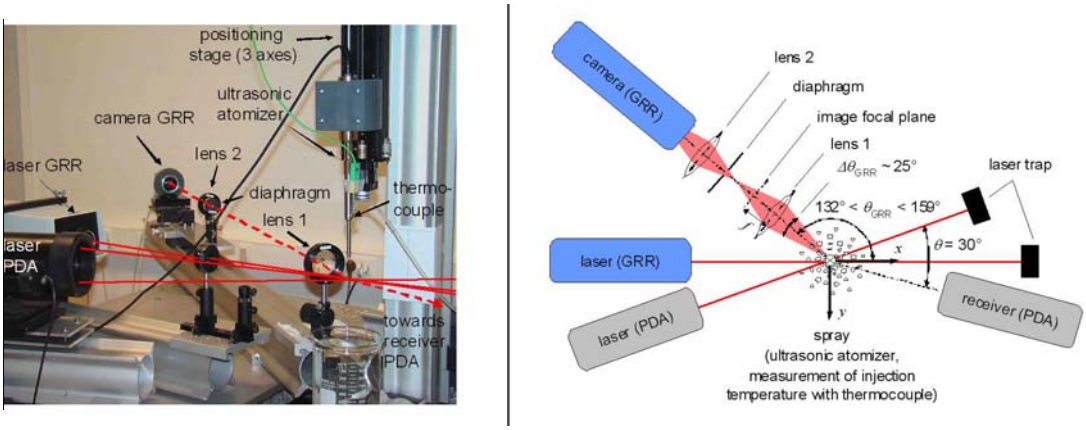

Figure 6.3: Photograph and top-view of the experimental setup

liquid flow rate and the chosen injector head. A thermocouple, disposed into the atomizer, close to the nozzle, measures the liquid temperature. To measure the diameter and axial velocity of each droplet a commercial PDA system is used. The PDA receiver is placed in forward diffusion at 30° angular position. The scattered light at this position is dominated by the first order refraction for a parallel polarization. For the GRR technique, a HeNe continuous laser, delivering a power of 30 mW is used. The droplets in the probe volume are illuminated by the incident laser beam. The light scattered by the droplets is submitted to an optical Fourier transformation through the first lens of the optical system. In this way, in the focal plane of the first lens, the scattered light intensity is expressed only as a function of the scattering angle and is independent of the droplet position in the probe volume. The image of the optical Fourier transformation is reproduced by the second lens on the CCD linear sensor. A diaphragm placed in the image plane of the first lens gives the possibility to control the dimension of the probe volume. The optical arrangement can be rotated in order to allow the measurement of a large range of angles. For a successful measurement of the temperature by GRR technique, a relation has to be found between the pixel number and the angular position of the scattered light intensity. This was realised by the use of the same incident laser beam, reflected by a mirror disposed in the probe volume. The mirror is fixed on a micrometric rotating plate. The reference angular position is done by superposition of incident and reflected laser beams. Afterwards, the position of the illuminated pixel is recorded for different angular positions of the scattered light.

A 3rd order polynomial correlation is used and the error is 0.001%. Since GRR provides only the refractive index of the droplets, a correlation between the refractive index and the liquid temperature needs to be determined. For some liquids the literature gives such correlations. Nevertheless, theses results can be obtained by using the multispectral refractometer available at laboratory. The results show a systematic linear evolution of liquid temperature as a function of the refractive index. From the global rainbow optical signal, the droplets mean temperature is determined by using an inversion code, developed at the CORIA laboratory by S. Saengkaew and G. Gréhan. By the use of the Non-Negative Least Square algorithm with light intensity computed by the Nussenzveig theory and minimizing the distance between the recorded and computed global rainbow pattern, a mean refractive index and a size distribution are extracted. For all the measurements the incident laser beam absorption is supposed to be too weak to influence the spray temperature or droplets evaporation.

6.2.2 Determined spray parameters

With this combination of PDA and GRR measurements a detailed characterization of the liquid phase of the spray is possible. The obtained data includes radial and axial profiles of the droplet size distribution (in D_{10},D_{20},D_{30},D_{32}), temperature, velocity components, number density and volume flux. Of this multitude of information, two parameters of great importance to the comparative IRE experiments are presented: Droplet size distribution and the radial droplet temperature profile.
To understand the impact of the former one on the Extinction measurements we have to recall one of the limiting conditions Drallmeier et al. give for the applicability of their simplification to this technique. They state, that only for spray with an Area Mean Diameter greater than 20 μm the refraction component of the extinction can be regarded as equal for both wavelengths (chapter 2.3.2 or [11]). Therefore, if the droplet size distribution shows a great number of particles inferior or close to this limit, an employment of the IRE is not possible. The following results were obtained using n-octane at a flow rate of 35 ml/min and at ambient temperatures between 26 and 27.5 °C.

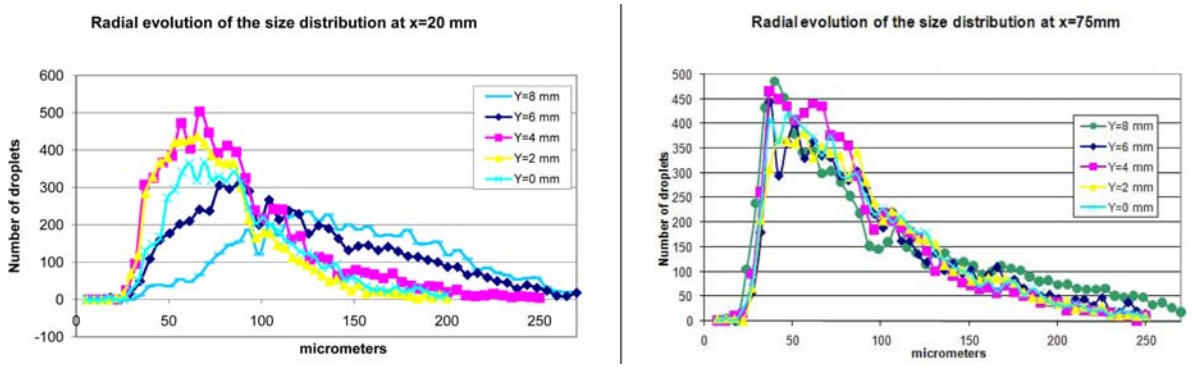

Figure 6.4: Droplet size distributions at x=20mm (left) and x=75mm (right)

Figure 6.4 presents the size distribution for two axial positions, x=20mm and x=75mm respectively. At each level, the profiles for five radial positions are compared.

We see, that the distribution closer to the injector shows a significantly larger number of droplets greater than 100 μm than the profile further downstream. This effect is strongest at the spray border, causing a great difference to the values near the spray axis. A quantification of this variation can be made by calculating the Area Mean Diameter (D_{20}) at radial positions of interest.

$$D_{20} = \left[\frac{\sum N(D) \cdot D^2 dD}{\sum N(D) dD}\right]^{1/2} \tag{6.1}$$

Applying equation 6.1 an Area Mean Diameter of $D_{20} = 154.3\ \mu m$ for y=8 and of $D_{20} = 92.8\ \mu m$ for the center position is obtained.
At 75 mm distance to the injector the spray is homogenized due to secondary breakup and evaporation. Much smaller differences between the radial positions can be observed. This is also expressed by the D_{20} of 117 μm at the border and 101.3 μm at the center respectively. For both positions these values are clearly higher than the limit of 20 μm. However, a similarity to both positions is a high number of droplets between 30 and 90 μm. This peak is just above the application limit for IRE measurements. They a further shift of the size distribution to the left should be strictly avoided.

The influence of the radial droplet temperature profile is more obvious. A lot of optical parameters, including refractive index (n, κ) and absorption coefficient (α), depend on the droplet temperature. For that, an important fluctuation of this temperature between the radial positions would demand specific corrective terms for each one to assure correct results.

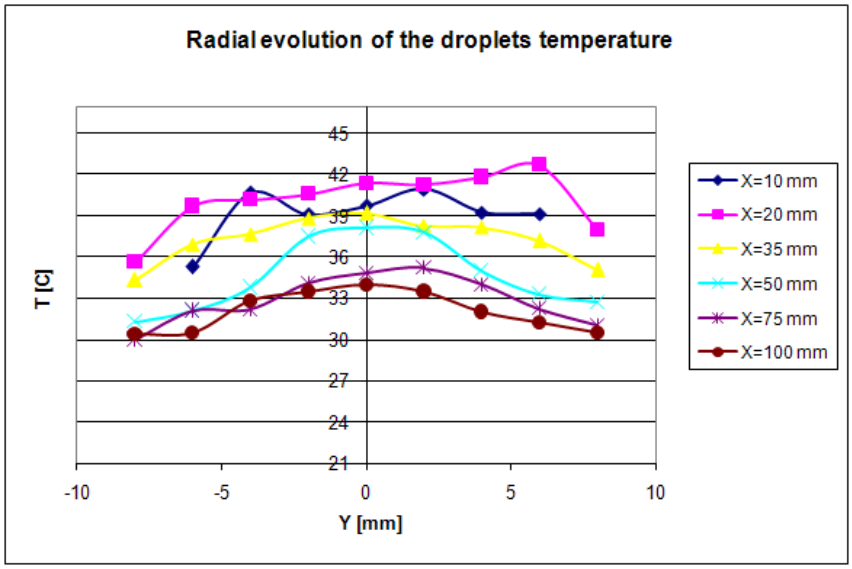

Figure 6.5: Radial evolution of droplet temperature from x=10 to x=100 mm

As we can see in figure 6.5, the radial temperature difference is most distinctive at x=50 mm. At this point, the borders of the spray have already cooled while the center is still close to the initial temperature. Upstream of this position, we observe the beginning of this temperature

drop at the borders while the core region shows only little differences ($< 3°C$ at x=35 mm). Downstream the overall level of temperature drops significantly, but flattens in radial direction. At the two positions chosen for the infrared comparison, x=20 and x=75 mm, the differences rest below $5°C$ (except the position at the very border at the upstream level). Literature research on the temperature dependence of the absorption coefficient shows, that for this variation, the change in the value of the imaginary part of the refractive index, and therefore of α, is minimal and the coefficient can be regarded as constant [61].

6.3 Changes to the IR-setup and experimental parameters

Thanks to the modularity of the IRE test bench, only small changes have to be made to adapt the setup to spray measurements.
The most important ones are the change from the piezo-driven monodisperse injector to the ultrasonic spray generator and the change of the experimental liquid. While the experiments on the droplet stream are performed using acetone - to assure comparability to the results of B.Frackowiak - for spray investigations n-octane is chosen according to the conditions of V.Bodoc.
Following the change of the injector, the way of controlling the liquid mass flow has to be modified. Since the flow through the droplet injector is limited by a diaphragm with fixed diameter, the knowledge of the injection pressure suffices to calculate the mass flow. For the ultrasonic system used in the spray configuration this is no longer possible. Therefore, a flow meter has to be added.
A positive side effect of these modifications on the injection system is the replacement of the rather fragile original support by a more solid construction (figure 6.6.
Minor changes concern the data acquisition. Since no time-resolved measurements are envisaged, the acquisition frequency can be dropped to 10 kHz (from up to 250 kHz at the monodisperse configuration). This allows to rise the acquisition time for each measurement (15 s in comparison to 0.3÷0.5 s) to obtain a greater number of values to be averaged.

Figure 6.6: Photograph of the modified IRE test bench. 1... injector; 2...pinhole

Chapter 7

Results and Discussion

7.1 Droplet Stream configuration

7.1.1 Methodology of the experimental runs

First step of every experiment made on the droplet stream is to preheat the laser sources and the electronic equipment. Following the test presented in chapter 4.3.1, this was done for at least 40 min.
The droplet injection frequency,f_{inj}, is generated as a higher harmonic of the chopper frequency. Its value is chosen by using the settings of the LIF experiments ([15, 4]) as a starting point and then modifying the frequency in order to obtain a stable stream of monodisperse droplets. The same procedure is applied to determine the injection pressure Δp_{inj}. The mono-dispersity of the droplets is continuously controlled by a shadowgraphic system (chapter 4.2.3) synchronized to the injection frequency.
The choice of the acquisition frequency depends on the injection frequency and the limits given by the acquisition chain (chapter 4.2.5). The goal is, to obtain a frequency that results in the same number of values per droplet crossing the beam for every droplet signal. This demands a two-step approach which is described by the following equations:

$$n_{p-eff} = \frac{f_{acq-max}}{f_{inj}} \tag{7.1}$$

$$\Downarrow$$

$$f_{acq} = base\,(n_{p-eff}) \cdot f_{inj} \tag{7.2}$$

First, the number of values per droplet at maximal acquisition frequency, n_{p-eff}, is determined (7.1). In general the result is no whole number. Experiments using this acquisition frequency would result in a varying number of points per droplet, making numerical averaging of the signals difficult. By cutting the digits of n_{p-eff} after the comma, we obtain an integer that leads - multiplied by the injection frequency - to the acquisition frequency nearest to the

maximum,f_{acq}, that guarantees the desired stability in points per droplet (7.2).

To determine the horizontal range and resolution of the measurements the droplet stream positions corresponding to the beam center and its limits have to be known. The center position is located by looking for the minimum of the detected laser intensity while moving the droplet stream across the laser beam. Equally, the limits are placed at the positions where no influence of the stream on the laser signal is detectable anymore. Using these values, the horizontal step size,Δy, is chosen as a compromise between spatial resolution and experimental effort.

Calibration measurements without the droplet stream are taken before and after each series of experiments. A median is created which serves as reference for the extinction measurements. Due to the high acquisition rate, a short acquisition time can be chosen to avoid large data files for the post treatment. In the present case, the acquisition time was 0.3s for measurements and 0.5s for the calibrations. Each horizontal positions is measured six times. From these values, again the median for each position is created.

Table 7.1 presents the experimental configurations investigated in this fashion, compared to the settings used by Frackowiak for the PLIF measurements.

Parameter	IRE		LIF
$\Phi_0[\mu m]$	50	100	100
$f_{inj}[kHz]$	9.8 / 16.9	8.6 / 9.3 / 17.9 / 26.5	22.69 / 9.28
$S_g[D_{drop}]$	$\approx$ 6 / 3	$\approx$ 4 / 3.75 / 2.5 / 2	2 / 3.76
$D_{drop}[\mu m]$	137 / 106	245 /238 / 220 / 194 / 173	173 / 238
$f_{acq}[kHz]$	80 /160	80 / 160 / 234 / 249.4	—
$\Delta p_{inj}[bar]$	0.35	0.38 / 0.4	0.35 / 0.4
$v_{inj}[m/s]$	8.05 / 6.95	8.42 / 8.3 / 8.68 / 9.17	7.87 / 8.30
$T_{drop}[°C]$	22 / 25 / 45.6	22 / 25 / 45.6	22.4 / 45.6

Table 7.1: IRE measurement parameters and comparison to available LIF data

All measurements use acetone as experimental liquid and are taken at a vertical distance of 37 mm to the injector head. This position is far enough from the oscillating orifice to obtain a stabilized, monodisperse stream of droplets while being close enough to neglect the diminution of the droplet diameter by evaporation [**?**, BrunoThese, BrunoArt]
Several limitations for the IRE in this experimental configuration are revealed by the performed test series:

- The exact reproduction of the PLIF settings prove to be impossible due to an instable droplet stream under these conditions.
- The lower detection limit of the infrared channel is reached when using a diaphragm of $50\mu m$ and injection frequencies superior to $\approx$ 10 kHz at room temperature.
- at injection frequencies $> 10kHz$ the signal-noise-ratio drops drastically for both investigating wavelengths. Rejection rates up to 40% of the values can be observed.

Reasons for the first difficulty may be the use of another type of frequency generator for the present experiments and the test-rig-based necessity to install the injector upside down in comparison to Frackowiak. However, configurations that lead to droplet characteristics close to those of the PLIF measurements will be used for comparison.
Point two and three are a consequence of the relation between droplet spacing and beam diameter. At elevated injection frequencies, the droplets are closer to each other, thus diminishing the axial differences in vapor concentration. Combined with the rather large beam diameters of ≈1.1 mm, a separation of single droplets is not achieved anymore. This is especially the case for small droplets at ambient temperature, since the absorption by their vapor field is already near the noise level.

7.1.2 Droplet results

Due to the difficulties to reproduce the conditions of the LIF experiments, a direct comparison of measurement results is not possible. On the other hand, there is good coherence between the LIF and the DNS calculations by B.Frackowiak (chapter 3.2.1). Therefore, an indirect way of confrontation by comparing the IRE results to the simulated data is chosen. Naturally, these values do not represent the current experimental conditions either, but they allow qualitative comparison for both, radial and axial profiles.
Furthermore, only measurements at conditions close to the low-frequency LIF case are presented, since the low S/N ratio at higher frequencies did not allow to obtain a reasonable amount of data.

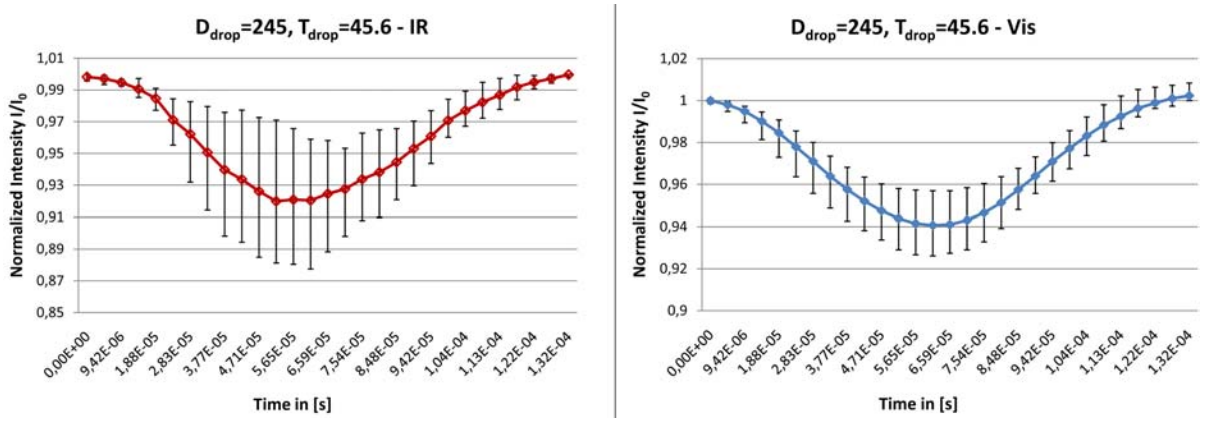

Figure 7.1: Mean vertical extinction profiles for $D_{drop} = 245\ \mu m$, $f_{ex} = 8.6$ kHz and $T_{drop} = 318.55$ K; **Left:**Infrared; **Right:** Visible

The results given in figure 7.1 represent the extinction of the two laser wavelengths for a droplet of 245 μm diameter and a temperature of 318.55 K, at an injection frequency of $f_{ex} = 8.6$. Both profiles show the smooth, symmetric curve that can be expected when a spherical droplet crosses a cylindrical laser beam. The general level of absorption is higher for the infrared wavelength than for the visible one. This too can be expected, since the infrared, being an absorbing wavelengths for hydrocarbons, is affected by both vapor and liquid phase

while the visible light is subjected to scattering only.
Regarding the dispersion of values for the two curves, it is visible that especially the infrared signal owes its smooth shape to the averaging over several measurements. While the error level for the visible signal rests nearly constant over the whole length of the extracted signal the change and the amplitude of the infrared dispersion is very high, with the latter reaching nearly 100% of the signal value. These number are qualified though, by the fact, that one droplet crossing only represents ≈ 1-2% of the whole measurement signal. Therefore are these fluctuations, as disturbing they may be for the droplet characterization, still in an common range for experimental investigations. Luckily their unsteady nature allows to eliminate them by averaging processes, as can be seen in these figures.

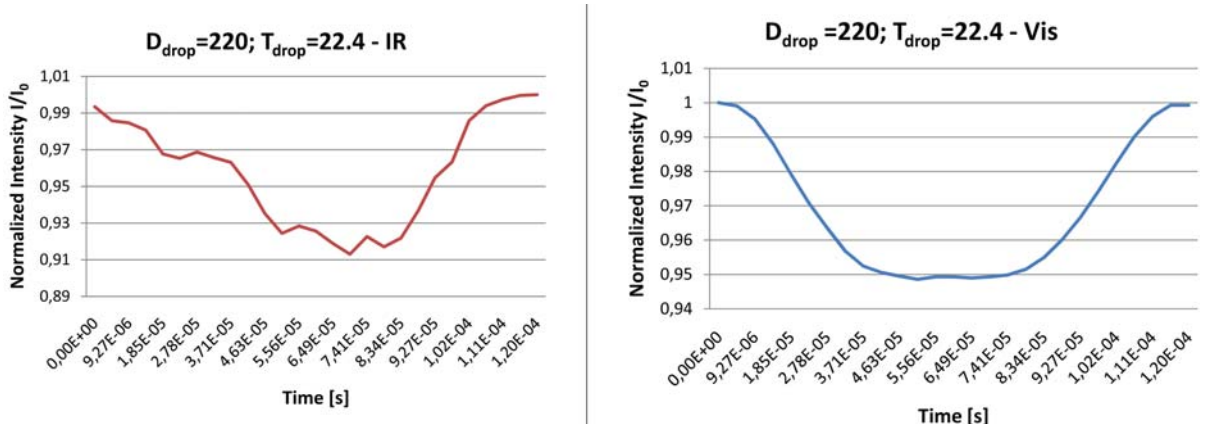

Figure 7.2: Mean vertical extinction profiles for $D_{drop} = 220\ \mu m$, $f_{ex} = 9.4$ kHz and $T_{drop} = 295.55$ K; **Left:**Infrared; **Right:** Visible

Figure 7.2 presents the same kind of profile as discussed above but for different experimental parameters. The droplet diameter for this case equals $220\mu m$ and is therefore a little smaller than in the former case. This reduction of diameter is due to the augmentation of the injection frequency to 9.4 kHz. The temperature of the droplets is set to 295.55 K and is therefore only two degrees above ambient conditions. For this configuration no detailed error statistics are available. Therefore the depicted curves represent a mean droplet signal over one measurement run only. In that way, however, it gives a good example for the difference in stability between visible and infrared wavelength. While the shape of the visible signal forms a nearly perfect symmetry, the infrared one is heavily distorted. This effect can be observed for every tested configuration. Since these disturbances usually appear asymmetrically (compare also the IR error bars in figure 7.1), they can be related to unsteady fluctuations of the surrounding vapor tunnel. This explains also the fact, that the visible, non-absorbing wavelength is not affected at all.
The differences in the experimental parameters between the two cases can also be observed when comparing the profiles. Since a higher injection frequency diminishes the droplet spacing, the resulting duration of on droplet period is approximately 9% shorter than for the first case. The lower level of extinction for the visible wavelength in comparison to the former results, indicates a smaller droplet size, since for the visible no vapor absorption occurs. The lower temperature gradient between droplet and ambient conditions, which subsequently results in a lower evaporation rate, should be visible as a smaller difference between the IR and the visible

signal than before. This effect, however cannot be observed in this example. Although, the steep drop at the right flank of the IR signal suggests that the presented center values are at the lower limit of the fluctuations, such as are shown in figure 7.1.

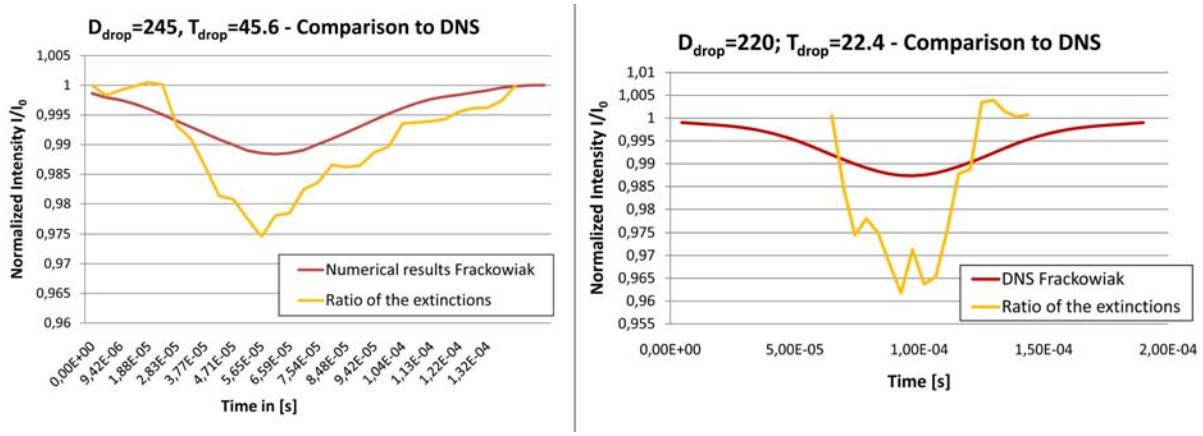

Figure 7.3: Comparison of the isolated vapor absorption to the DNS predictions. **Left:**$D_{drop} = 245\ \mu m$, $T_{drop} = 318.55$ K; **Right:** $D_{drop} = 220\ \mu m$, $T_{drop} = 295.55$ K

According to equation 2.27 the extinction due to the vapor phase can be separated by a subtraction of the logarithms of I/I_0 for both wavelengths. Since $-\ln(A) - \ln(B) = \ln\left(\frac{B}{A}\right)$, the simulated absorptions of the vapor phase can be compared to the fraction of the Infrared extinction profile over the visible one.
Both presented cases are compared in this fashion to the calculated vapor absorption profiles for the respective parameters. It has to be noted, however, that the conditions for the numerical simulations differ from the experimental ones because of the limited number of data available for this evaporation model! In the present case, the calculations are always performed for droplets of 238 μm diameter at a spacing of 3.76. Only the beam width as well as ambient and droplet temperatures can be modified according to the experiments.
For the heated configuration at $45.6°C$ the shape of the fraction resembles the simulated profile for a large part of the profile but for shift towards higher absorption. One part of this difference is certainly due to the fact that the experimental droplet (D_{drop}=245 μm) is slightly larger than the one used by Frackowiak to compute the vapor field (D_{drop}=238 μm). Another possible reason, especially for the center region where a significant peak appears, is the fact, that the effective scattering cross section of a particle exceeds its diameter. Therefore, the droplet can also influence beams, that are passing close by. This effect is not implemented in the absorption calculations. In any case, the general level of absorption is very low for single droplets ($< 2\%$ in comparison to the chopper signal), so that the influence of noise can never be completely negated for test runs consisting of 6 measurements only.
The cooler configuration results, however, show no resemblance to the simulated absorption values. The signal is much narrower and its amplitude is significantly greater than the numerical predictions. The large amplitude of the extinction ratio is a direct consequence of the great difference between the extinction curves of the two wavelengths and therefore of the disturbances on the infrared signal. Additionally, the sharp center peak, related to scattering effects before, appears near 0.1 ms.

The narrower shape can be explained by the fact, that the simulation takes into account the effects of interaction , but it computes a single droplet which happens to have these effects in its vicinity, without a trailing droplet disturbing the further development of the profile. Therefore, a smooth development of the profile in every direction is possible. The droplet stream signal, on the contrary, is extracted from a series of droplets passing. Since the spacing in the second configuration is significantly smaller than in the first one (S_d=3 and 4, respectively), the outer regions of the droplet signal merge into a vapor tunnel with a constant level of low absorption. As the droplet signals are detected as a function of the changing gradient at its borders by the evaluation routines, this constant level is likely to be ignored and the borders of the signal are therefore 'cut'. This results in a signal narrower than the one for the single droplet.

7.1.3 Conclusion

Because of the narrow stability range of the injector, only a small number of results could be presented. The extinction profiles in axial direction of the infrared and the visible wavelength have been extracted for two cases with different diameter, spacing and temperature. An analysis of the dispersion of the values confirms the necessity to average over multiple measurements in order to obtain clear profiles.
As a second step the experimentally determined extinction component due to the vapor phase is compared to values obtained by numerical simulation. For the experimental case closer to the theoretical conditions, similarities in level and shape can be observed for a large part of the signal. A significant difference in shape appears in the center region. This effect can be explained by scattering processes which are not taken into account in the modeling. The second case shows severe differences to the numerical predictions in amplitude as well as in shape. Although a part of the differences can be explained by several physical and numerical effects, the level of discrepancy rests unsatisfying. This second configuration is a good example for the limits of the simulation, using predefined vapor fields. At the same time the necessity to ameliorate the S/N ratio is emphasized!

7.2 Spray configuration

7.2.1 Experimental approach

The experiments on the spray follows a similar procedure as that for the droplet measurements. After the respective preheating period of all the components, the system is purged by sending the liquid at the nominal mass flow rate through the injector without excitation. Once all the air is evacuated, this process results in a smooth liquid stream from the center of the injector. This flow is used to verify the vertical orientation of the system and to center it on the laser beams. From now on, this center position serves as reference point to the horizontal movement of the injector and is expressed by the coordinate 'y=0'. The other coordinates are given by the vertical distance from the injector tip to the beam center ('x') and the axial distance of the injector center to the pinhole upstream ('z') (figure 7.4). The spray divergence is known from PDA/GRR measurements to be $\approx 7°$. With this information, the theoretical limits of the spray can be calculated in function of the vertical distance to the injector.

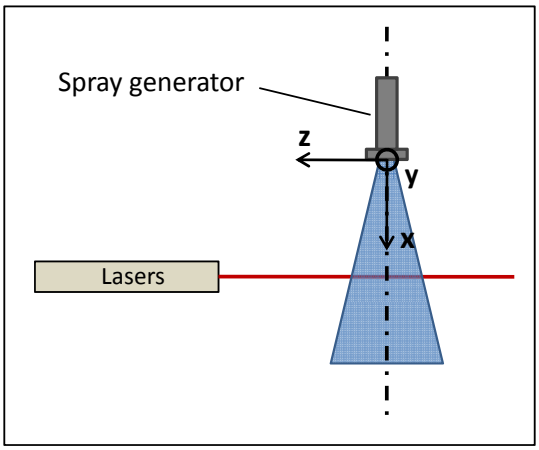

Figure 7.4: Coordinate system for the spray setup

As for the droplet stream measurements, each test series is preceded and followed by a calibration measurement without liquid flow. The average of these two measurements is taken as reference laser intensity. Table 7.2 gives an overview of the configurations investigated.

Vertical Position x [mm]	20	30	50	75	100	125
Axial position z [mm]	60 / 80 / 90					
Horizontal Range y [mm]	±13(18)	±13	±15	±18	±18	±18
Horizontal step Δy [mm]	1(3)	1	1.5	2	2	2
Excitation frequency [Hz]	20.000					
Exc. amplitude [% Amp. max]	30 / 75					
Injection temperature [$°C$]	45					
Flow rate [ml/min]	35(50.5)	35				
Ambient temperature [$°C$]	22.5 /25.4					
Acquisition frequency [Hz]	10.000					
Acquisition time per point [s]	20(15)					

Table 7.2: Parameters of the performed spray measurements

Each position is submitted to six consecutive measurements except a last test series at elevated mass flow rate. Due to the limited liquid reservoir, the repetitions for this setting are limited to three to guarantee stable conditions. The parameters for this special case are given in brackets. The figures presented in the following section give the mean value of these measurements with

error bars at each point to indicate the dispersion.

7.2.2 Spray results

To study the development of the evaporation in the spray, two vertical positions have been chosen for comparison and will be presented in this section. The absorption at x=20 mm represents a point close to the injector, while the second choice, x=75 mm, aims at the description of the fully developed spray. For each position, the absorptions of the infrared and the visible channel are presented and discussed. Additionally, the measured vapor concentrations are compared to numerical results obtained by Bodoc [17]. Due to reasons explained further below, this last step could be completed for the first position only.

Figure 7.5 shows the absorption of both employed wavelengths by the spray at x=20 mm. When looking at the absorption curve for the infrared wavelength, the typical bell-like shape of the absorption of a radial-symmetric field, as seen at the droplet measurements, is distinguishable. But unlike to the measurements presented at the beginning of this chapter, the absolute level of absorption is significantly greater due to the expansion of the spray cone.
The same shape can be observed for the visible wavelength, however much smoother. This can be expected, since the diminution of the infrared signal contains extinction by the vapor and the liquid phase, while the visible extinction depends on the droplets only.
Considering the error levels, the higher values at the infrared signal can be explained by same reason. A fluctuation in the spray causes changes in both vapor and gas phase. For that, the infrared signal is afflicted double.
Taking a closer look at the positions of the errors, we obtain the same distribution for both wavelengths: At the center positions, y=-2, y=0 and y=2, the error levels are small. They rise strongly at the rising flanks of the signal before diminishing again at the limits. This behaviour indicates an instability of the spray in radial direction, changing the distribution in the outer zones but not strong enough to influence the spray core. The fact, that this effect is less visible at the limits of the spray is due to the sensitivity limits of the detectors at these low levels of absorption.
A striking point of these measurements,however, appears at the superposition of the two absorption curves as shown in the bottom graph. For the greater part of the spray the visible channel shows a greater level of absorption than the infrared one. Considering, that following the simplifications by Drallmeier et al. the extinction by the liquid phase is considered as equal for both wavelengths and that the vapor only affects the infrared, this is exactly the opposite of what is to be expected.
Possible reasons for this behaviour are the fluctuations in the spray as mentioned above, or a misinterpretation in characterizing the spray, which is outside the conditions for IRE measurements in reality.
The first possibility is examined by performing an additional measurement run at the same position, but at an elevated mass flow rate of 50.1 ml/min. This measure has been found to stabilize the spray, but leads to spray conditions, for which no comparative numerical simulations are available. Therefore these settings can only be used for qualitative comparisons. Figure 7.6 presents the respective absorption curves.

The higher stability of the spray at this configuration is clearly visible at the significantly

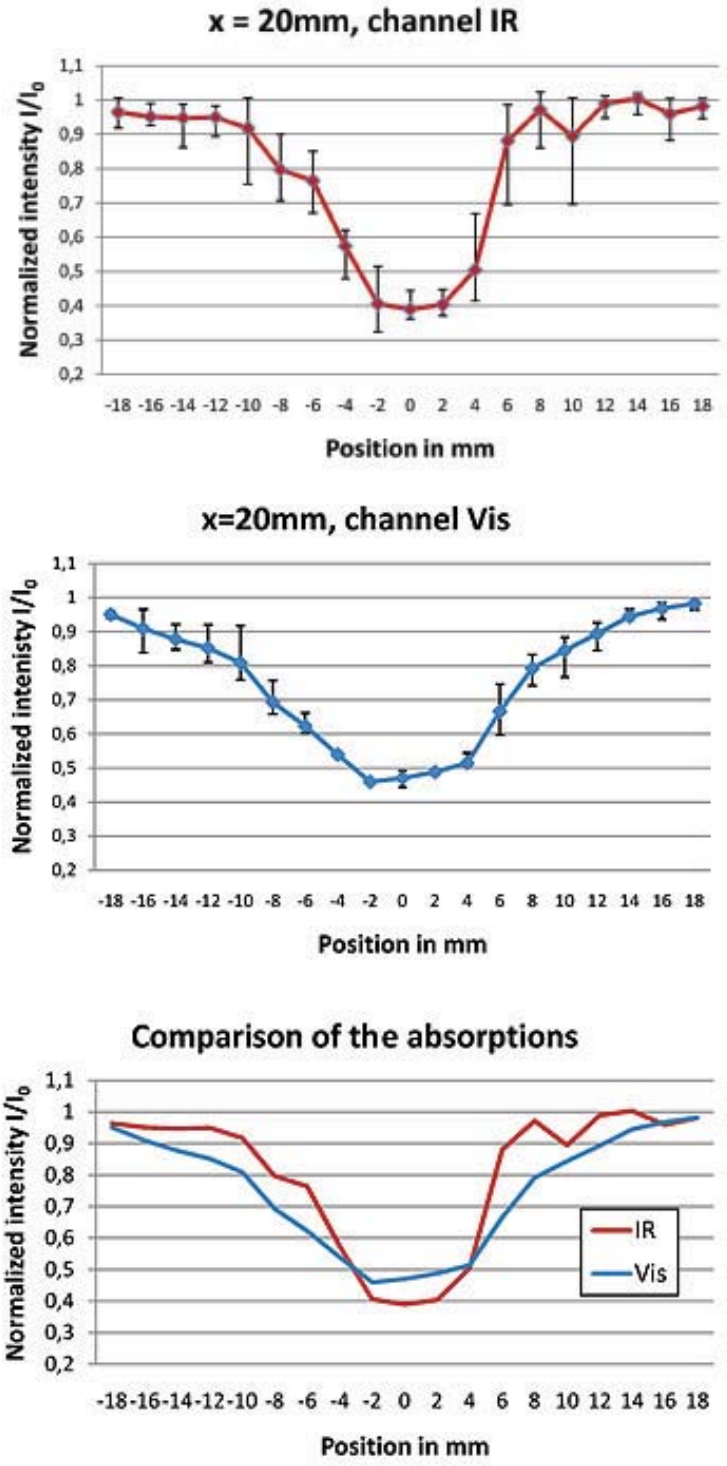

Figure 7.5: Mean extinction profiles for the spray at x=20 mm,$\dot{m} = 35ml/min$. **Top:**Infrared; **Center:**Visible; **Bottom: Comparison without error bars**

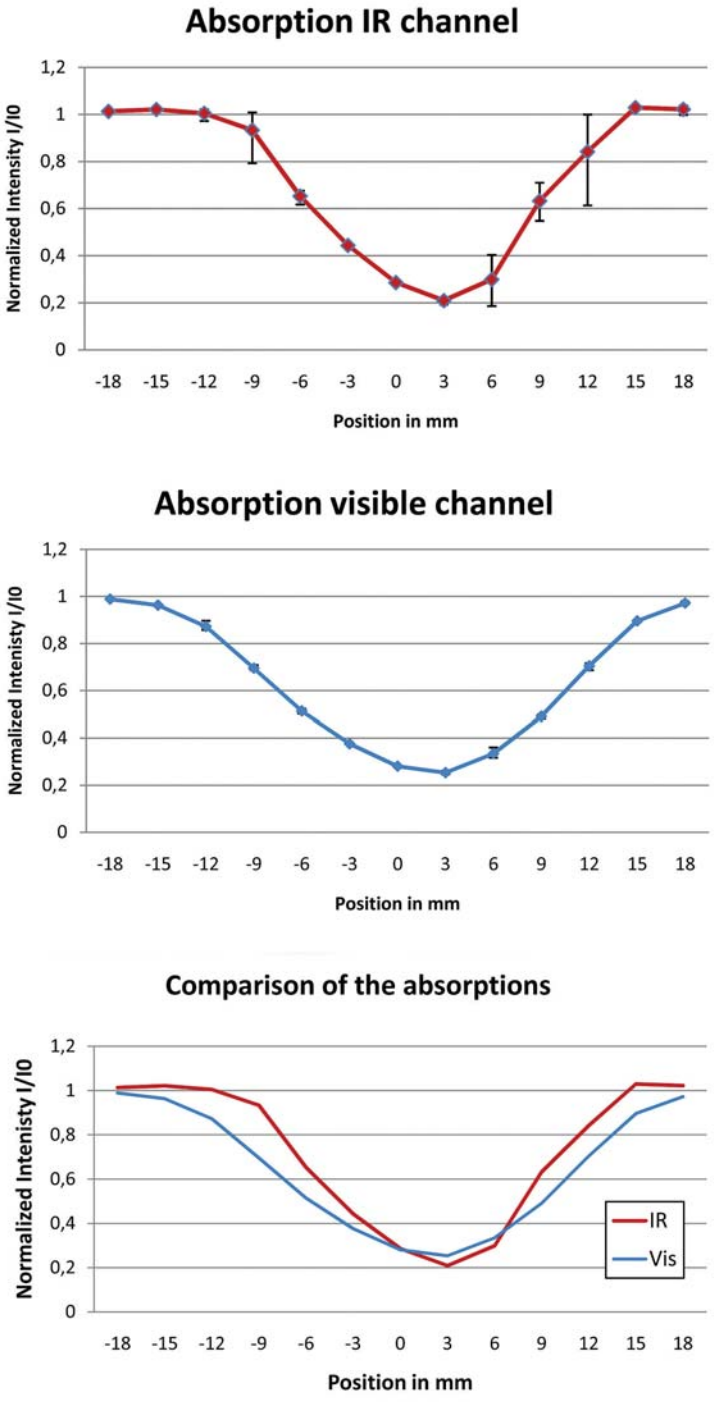

Figure 7.6: Mean extinction profiles for the spray at x=20 mm,$\dot{m} = 50.5ml/min$. **Top:**Infrared; **Center:**Visible; **Bottom: Comparison without error bars**

reduced error bars of the measurement values. Except for the rising flank between positions 6 and 13 of the infrared signal, practically no dispersion can be observed. The maximum of absorption has moved to position 3 which indicates, that the spray is not entirely symmetric. Values greater than one at the IR curve are due to the calibration tolerance and can be regarded as equal to one.
Regarding the comparison of the two profiles, we see, that the effect of higher extinction of the visible wavelength, except for the center positions, persists. Therefore it can be said, that this phenomenon is not caused by the instability of the spray.

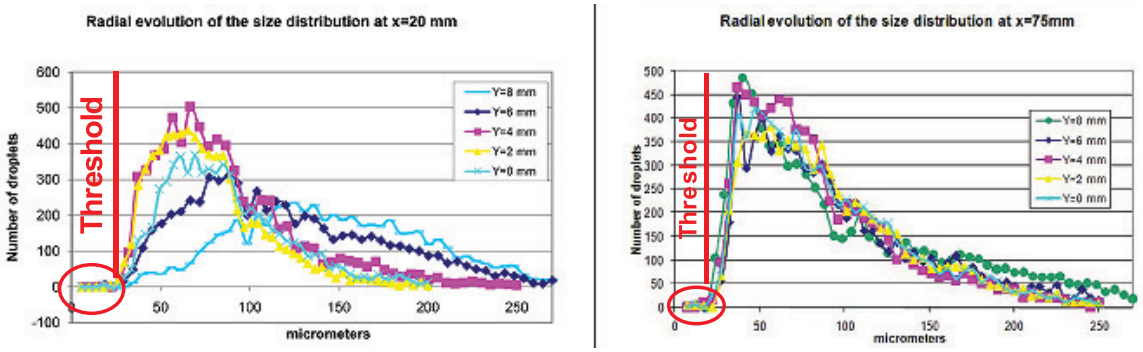

Figure 7.7: Threshold of the PDA measurements

A closer look at the PDA measurements as shown in chapter 6.2.2 leads our attention to the sudden drop of the droplet number for diameters smaller than 30 μm which escaped the former characterization of the spray (figure 7.7). In fact, these measurement were calibrated in a way to cover a maximum range of droplet sizes in the spray. As it seems, this versatility caused the PDA to optimize on the larger droplet sizes and therefore not detecting the smallest droplets anymore. However, an important number of not detected droplets smaller than these 30 μm, is very likely to shift the Mean Area Diameter of the spray below the limits given by Drallmeier et al. for the application of the simplified IRE measurements. Since the small droplets are very likely to be situated in the outer regions of the spray, partly due to beginning evaporation, partly due to suction effects of the entrained air, this hypothesis corresponds well to the measured absorption behaviour.

In spite of these problems at the outer regions of the spray, a quantification of the apparently reasonable values in the spray center is the next step. As shown in chapter 2.3.2, the local concentration value can be determined from the fraction of the absorption measurements of the two wavelengths:

$$\overline{c_m} = \frac{1}{\alpha \cdot l}\left[-\ln\left(\frac{I}{I_0}\right)_{632.8} - \ln\left(\frac{I}{I_0}\right)_{3.39}\right] \tag{7.3}$$

$$= \frac{1}{\alpha \cdot l}\ln\left[\frac{\left(\frac{I}{I_0}\right)_{3.39}}{\left(\frac{I}{I_0}\right)_{632.8}}\right] \tag{7.4}$$

The difficulty in obtaining the local concentration values for this points is based in the fact, that the Onion-Peeling scheme employed to deconvolute the axisymmetric system propagates from the spray limit towards the center. Therefore, a full set of valid values is necessary to achieve results at the innermost positions.
In the present case, the best fit to this condition can be found by using the values of maximal extinction for both wavelengths. The resulting relations of infrared and visible measurement are shown in figure 7.8 for the positions from '10' (spray limit) to '0' (center). We see, that these series shows the expected values below one except for the two positions '4' and '5', which indicates higher extinction of the visible laser at this points (marked in red in the figure). A deconvolution of this profile including these two values leads to heavy oscillations of the OP scheme which influence all the values afterwards. Therefore, the decision has been made to replace these points by values obtained through linear interpolation between the neighbouring points '3' and '6'. These interpolated values are indicated in figure 7.8 by the light-blue, red-bordered squares. It is clear, that by interpolating values the true behaviour of the spray is not represented. But this approach allows, to deconvolute until our points of interest,which lie in the spray center.

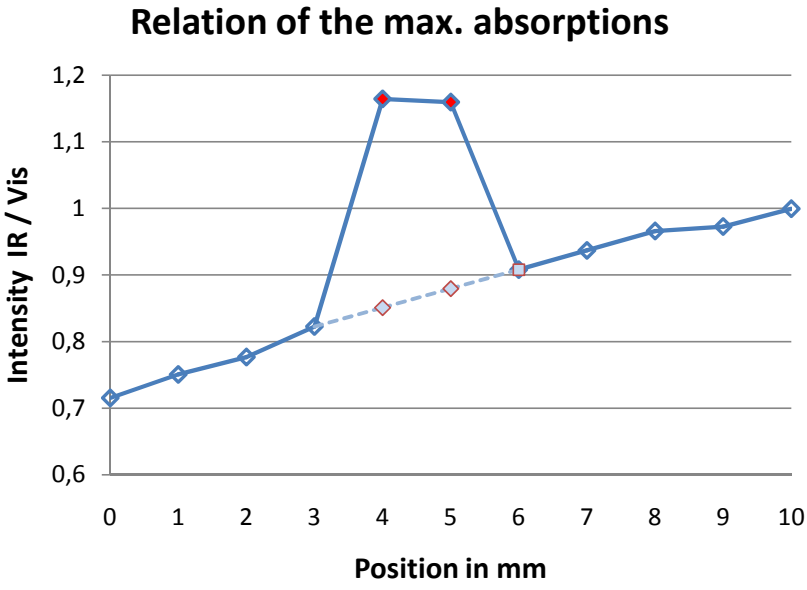

Figure 7.8: Interpolation of values for the deconvolution

The results of the deconvolution of this smoothened profile are presented in figure 7.9 and compared to values obtained through numerical simulations by Bodoc [16].

This comparison shows important differences between the experimental and the numerical values until close to the spray center. The constant underestimation of the spray concentration by the experimental results can be explained by the choice of the extinction values. While these were chosen for reasons of completeness, they represent not the average signal but the highest extinctions measured at these points. Therefore, a certain underestimation was to be expected. The differences in shape - the simulated profile rises much steeper than the experimental one - is a result of the interpolated values and an oscillating response by the OP scheme at position

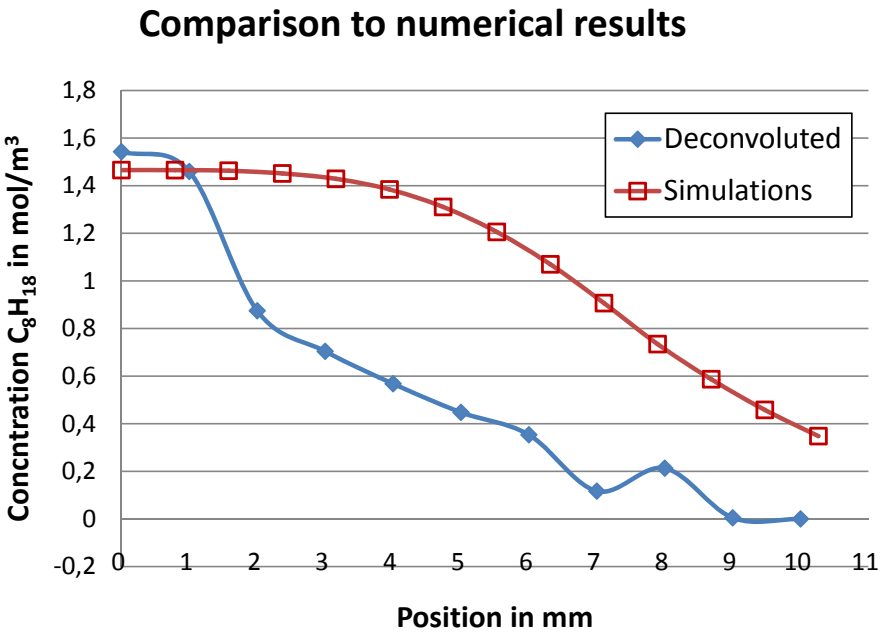

Figure 7.9: Comparison of the deconvoluted vapor mass fraction results to values predicted by V.Bodoc

'7'. This oscillation, caused by the fluctuations of concentration between the positions '8' and '9', has an underestimation of point '6' as consequence. Since this point is the starting point for the following linear interpolation, nearly the whole series is kept at a lower level. The influence of these two effects ends at point '2', which allows the profile to rise to its elevated values for the remaining center positions.
Considering all these effects on the deconvolution of the concentration values, it is the more satisfying to observe good coherence between experimental and simulated values for the last two positions. The difference of the center values, reaching 1.47 mol/m^3 in the simulations and 1.54 mol/m^3 after deconvolution, is less than 5%.
This indicates, that the present IRE setup is capable of performing extinction measurements of high accuracy if the investigated medium satisfies the necessary criteria concerning droplet size and density.
Figure 7.10 presents the absorptions for the position further downstream in the spray, at x=75mm.

At this position, the profiles are significantly less pronounced than further upstreams. This is due to the expansion of the spray which causes an homogenisation of both, velocity and droplet distribution repartition. The lower average density of the spray is also visible by the generally lower level of extinction for both wavelengths. Looking at the infrared extinction curve we see, that the error level is consequently high over all the positions of the spray. We can therefore assume, that the spray instabilities, which were visible at x=20mm at the outer zones only, now reach the whole spray.
More information on the nature of these fluctuations can be obtained from the visible extinction profile. An asymmetry of the spray towards the negative coordinates is recognizable. Since

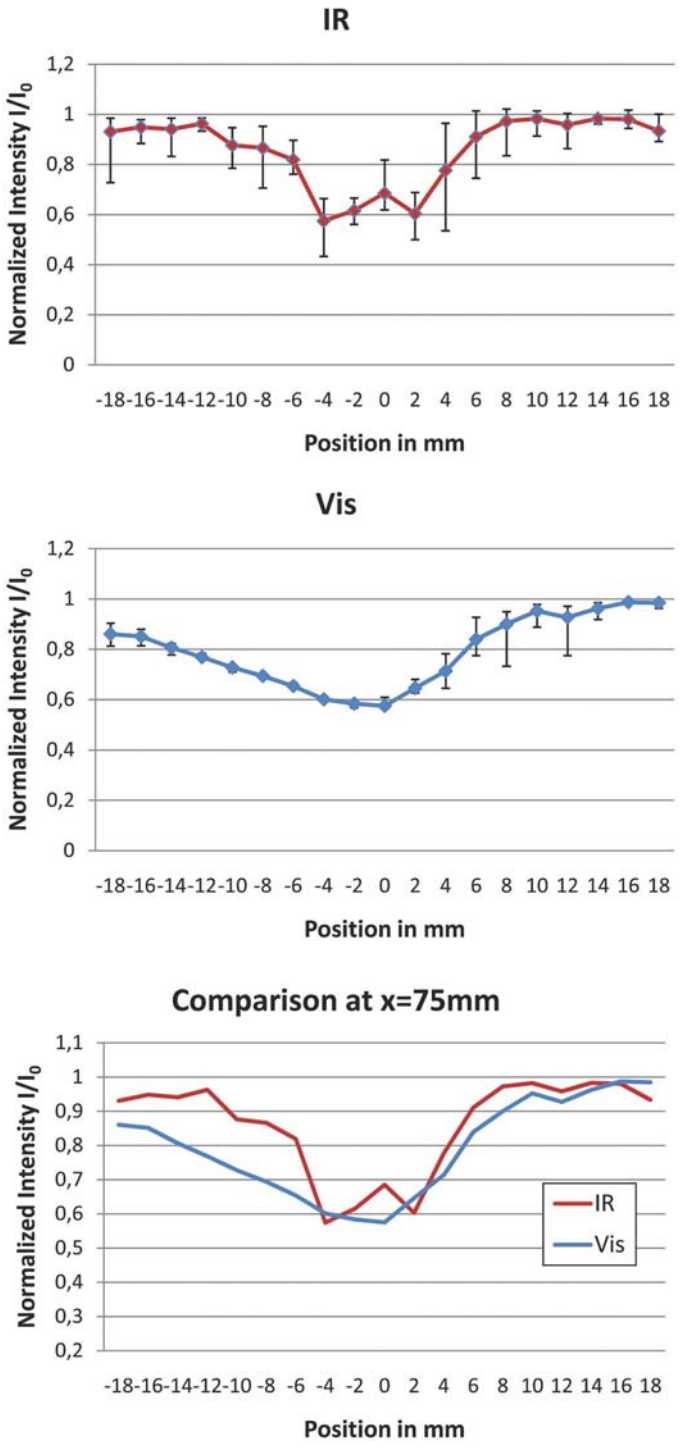

Figure 7.10: Mean extinction profiles for the spray at x=75 mm,$\dot{m} = 35ml/min$. **Top:**Infrared; **Center:**Visible; **Bottom: Comparison without error bars**

the error level in this region is very low, we can suppose that this deformation is due to a higher concentration of droplets in this region and is systematical to the injector. Therefore, the fluctuations in the infrared profile at these positions can be assumed to be mainly caused by the vapor phase of the spray.
From the comparison of the two profiles we see that this region is also the region of the greatest difference between IR and visible extinction. Following the insights from the investigations on the extinctions closer to the injector, this may signify that the concentrated droplets at these positions are very small.
However, the comparison shows also, that the effect of higher extinction of the visible wavelength persists over all of the radial positions at this distance from the injector. For this reason, no extraction of local concentration values is possible. An explication of this phenomenon through the diminished size of the droplets due to evaporation would fit into the hypothesis of the spray being outside of Drallmeier et al.'s conditions, but contradicts with the rise of the Mean Square Diameter at this position as measured by V.Bodoc (chapter 6.2.2. Further investigations on this problem are in progress but could not be finished in time for this thesis.

Chapter 8

Conclusions And Perspectives

This thesis describes the application of the Infrared Extinction Technique (IRE) to a jet of monodisperse droplets of acetone. An absorption simulation tool is developed and a suitable test rig is chosen and installed. Furthermore, routines for acquisition and signal treatment are created, including a 2D-extension to the Onion-Peeling deconvolution scheme. The measurements on the droplet configurations are complemented by a collaboration with V.Bodoc in applying the IRE to a ultrasonic spray configuration.

8.1 Summary

Definition of open questions in fuel concentration measurements

To optimize combustion, the prediction of the evaporation process, and therefore the local vapor concentrations, are of high interest. For this reason numerous numerical models are in constant development. For experimental verification of the influence of the assumptions made in these models, Laser Induced Fluorescence (LIF) is the first choice investigation technique today. Its advantages lie in the ability to obtain 2D images of the vapor field and the good adaptability to multiple reacting species. Negative characteristics are the necessity for high power laser sources to excite the molecules, which renders the equipment heavy, slow (in terms of acquisition frequency) and expensive, and the sensibility towards strong concentration gradients, as can be found in two-phase flows, which may produce saturation effects at the imaging devices. As a consequence, the quantification of concentrations at the liquid-gas-interface is very delicate, or nearly impossible. For this reason, an alternative technique is proposed to close these gaps.
The IRE is a lightweight, low-power investigation method, based on the absorption of infrared wavelengths by most of the hydrocarbons. The main advantage is the low amount of energy that is necessary for the extinction measurements, which allows to keep the equipment lightweight and inexpensive. Additionally, it renders the technique insensitive to abrupt changes of concentration. The downside of this technique is its limitation to point measurements and that the obtained results are line-of-sight averaged. These have to be deconvoluted in order to achieve spatial resolution along the beam axis. However, this is only possible for vapor fields

whose geometries contain a large number of symmetries.
A bibliographic study of the IRE, its development and recent applications reveals two interesting aspects that have not been subject to investigations yet. For once, no quantification of the IRE on small scale environments containing concentration gradients, such as droplets smaller than the beam width, can be found in the literature. And further, no comparison of this method to other optical measurement techniques, such as LIF, is known to the author. Consequently, four targets have been set for this thesis: Verification of the IRE's sensibility to detect single droplets, comparison to results obtained by LIF, gathering additional information from regions, where the fluorescence is not applicable and creation of an accompanying simulation tool for further development of the technique.

Numerical tools developed

With the aid of LabView^{TM}and Matlab^{TM}routines for data acquisition, treatment and comparison to a simplified simulated have been created. The treatment consists of several filtering and averaging algorithms which result in the extracted mean signal of the absorption by the vapor field around a single droplet which crosses the laser beam. As a next step, this signal can be compared to a numerical simulation of the absorption process. Three different evaporation models have been tested for this routine. The final choice fell on the implementation of computed vapor fields as provided by Frackowiak for a small set of experimental parameters. Although this limitation to the predefined cases renders the simulation inflexible, the chosen model is the only one, able to compute concentration profiles in axial as well as in radial direction to the droplet stream with sufficient accuracy. Efforts to replace this solution by a combination of simpler, more flexible approaches lead to a good approximation in radial direction, where the interaction between droplets is weaker, by the D^2-model. However no suitable simplified model to simulate the interaction effects between droplets could be found so far.
An important part in the post-treatment routines is the development of a 2D extension to the classic Onion-Peeling Scheme. The application on test profiles shows good coherence of the deconvoluted concentrations to the original ones for cases with high spatial resolution. However, a strong dependency on the initial values and a distinctive affinity to oscillate around sudden changes of the concentration gradient prevent this algorithm at the present state from being applicable to data with less than 100 data points. For this reason a deconvolution of the experimental data obtained during this thesis is not possible yet.

Measurements on the droplet stream

The goal of the measurements on a stream of monodisperse droplets was to test the behaviour of the IRE on a small-scale environment with strong concentration gradients and to obtain comparable results to the PLIF measurements performed by Frackowiak.
First test showed severe limitations to the actual setup concerning measurements at high injection frequencies or small droplet spacing respectively. Because of these restrictions, axial extinction profiles for larger droplets of 220 and 245 μm diameter at $22.4°C$ and $45.6°C$ respectively, are presented only. Comparisons to numerically determined vapor absorptions show a significantly higher extinction for the experimental data. An explanation for this effect was

given in scattering effects of the droplets which are not taken into account by the model. Due to the limits of the deconvolution scheme mentioned above, no spatially resolved results could be obtained.

Measurements on the spray configuration

To gain additional information on the test setup, experiments on a spray, formed by an ultrasonic injector have been performed. This part of the work has been done in collaboration with V.Bodoc, who characterized the spray using PDA and GRR. Tests were done using warmed n-Octane as evaporating liquid at several distances from the injector head. At all positions the phenomenon of higher extinction for the visible wavelength than for infrared occured in the larger part of the spray but for the positions at the spray center. As possible reasons spray instabilities and size distribution were investigated. Additional tests excluded the stability issue as source of this behaviour. However, investigations show a significant cut in spray characterization related to the employed measurement techniques. Therefore it can be considered, that the investigated spray is not entirely suitable for IRE measurements in its outer regions. In spite of this fact, a quantification of the central values could be done by the aid of a reconstructed radial profile. Although very limited in number, a good accordance to the numerical predictions by Bodoc was observed for these positions.

Conclusion

Of the four goals set at the beginning of this thesis, only the first one, consisting in the prove of the IRE's ability to separate single droplet signals, could be completely fulfilled. The comparison of the obtained data to PLIF results is only possible in an indirect way, using the simulations of Frackowiak, due to difficulties with the reproduction of the experimental conditions.
The numerical tools to obtain additional, spatially resolved information on droplet evaporation, which is not available when using (P)LIF, have been designed. Unfortunately the high numeric instability of the actual version prevents this algorithms from being successfully applied to the experimental results at the moment. A point, originally not mentioned as a goal, is the further validation of the experimental setup on a spray configuration. First tests on this application have been performed using an ultrasonic atomizer. This configuration was already in use for experiments on Global Rainbow Refractometry by V.Bodoc. Therefore the characteristics of the liquid phase were already known and a small number of simulated values for vapor concentration was available. Post treatment showed, that the outer regions of the spray do not fulfill all of the necessary prerequisites for IRE investigation. In spite this fact, results with good coherence to the simulations could be obtained for the center positions of the spray.
Concluding, it can be said that some big steps towards the application of the IRE on small-scale environments, such as droplet streams, have been made. Nevertheless, crucial points like a reliable deconvolution scheme or data, directly comparable to other optical concentration measurement methods are still to be completed.

8.2 Perspectives

Further numerical development

Concerning the simulation tool, a further research for a simplified model with interaction is strongly encouraged. Considering the good agreement of the basic D^2-model with the complex DNS simulations for the radial profiles, a similar replacement in axial direction would allow high flexibility to the simulation tool without sacrificing too much accuracy.
As improvement to the treatment of the acquisition signal, noise correction by adaptive filtering in the frequency range is recommended. First test show great potential to enhance the S/N ratio, especially for not completely stable droplet streams. Maybe the most important step for the near future is a refinement of the 2D - deconvolution scheme. Alternative deconvolution algorithms, less likely to oscillate around sudden changes of concentration, as proposed by Pretzler et al. [62] or Dumouchel et al. [63] should be investigated for their applicability to the droplet case. If successful, a such adaptation allowed to completely resolute two-phase flows by IRE measurements.

Continuative measurements

For continuative measurements a reduction of the beam width is preferable. Although this may increase the actual problems using the 2D-deconvolution scheme, it allows to investigate droplets with reduced spacing and size. Additionally the harmonization of the laser beam widths should be done separately for each wavelength by lens systems or optical fibers instead of the pinhole used in this setup. This way, the - wavelength dependent! - refraction before the investigation area can be avoided. Further IRE investigations should also include different experimental liquids, moving from mono-composants to bi- oder multicomposant fuels.
Possible alternative applications include the employment of infrared extinction under high pressure, high temperature or reactive conditions and the replacement of the single detectors by detector arrays or CCD cameras to obtain 2D images of the investigated zone.

In spite of the difficulties encountered during this work and the subsequent small amount of evaluable data, there is still a strong conviction in the possibilities of the IRE. Given the refinements, experimentally as well as theoretically, mentioned above, extinction measurements may prove a unique tool for fuel concentration measurements. If the basic evaluation algorithms and deconvolution schemes can be integrated into the measurement hardware, as it is already the case for industrial laser diffractometers, in-situ analyses of two-phase flows are imaginable.

Bibliography

[1] J.-U. Kim and B. Hong, "Quantitative vapour-liquid visualization using laser-induced exciplex fluorescence," *Journal of Optics A:Pure And Applied Optics*, vol. 3, pp. 338–345, 2001.

[2] F. Grisch, M. Orain, B. Attal-Trétout, G. Castanet, and F. Lemoine, "Laser based measurements in monodispersed droplet streams." NATO/PFP unclassified, RTO-MP-AVT-124.

[3] M. Orain, X. Mercier, and F. Grisch, "Plif imaging of fuel-vapor spatial distribution around a monodisperse stream of acetone droplets: comparison with modeling," *Combustion Science and Technology*, vol. 177, pp. 249–278, 2005.

[4] B. Frackowiak, A. Strzelecki, and G. Lavergne, "A liquid-vapor interface positioning method applied to plif measurements around evaporating monodisperse droplet streams," *manuscript for Experiments in Fluids*, no. EIF-0247-2007, 2007.

[5] M. Skinner, "use of infrared analysers for continuous measurement of the concentration of carbon monoxide in a moist and dusty atmosphere," *Modern Utilization of Infrared Technology V*, vol. 197, pp. 281–286, 1979.

[6] P. Ariessohn, S. Self, and R. Eustis, "Two-wavelength laser transmissiometer for measurements of the mean size and concentration of coal ash droplets in combustion flows," *Applied Optics*, vol. 19, No.22, pp. 3775–3781, 1980.

[7] A. Chraplyvy, "Nonintrusive measurements of vapor concentrations inside sprays," *Applied Optics*, vol. 20, No.15, pp. 2620–2624, 1981.

[8] M. Adachi, V. McDonell, and G. Samuelsen, "Non-intrusive measurement of gaseous species in reacting and non-reacting sprays," *Combustion Science and Technology*, vol. 75, pp. 179–194, 1991.

[9] J. Drallmeier and J. Peters, "Optical constants of liquid iso-octane at 3.39μm," *Applied Optics*, vol. 29, No.7, pp. 1040–1045, 1990.

[10] J. Drallmeier and J. Peters, "Experimental investigation of fuel spray vapor phase characterization," *Atomization and Sprays*, vol. 1, pp. 63–88, 1991.

[11] J. Drallmeier, "Hydrocarbon vapor measurements in fuel sprays: a simplification of the infrared extinction technique," *Applied Optics*, vol. 33, No.30, pp. 7175–7179, 1994.

[12] M. Golombok, P. Cooney, J. Kitching, and S. Nattrass, "Spatial resolution of fuel distribution in an engine using infrared absorption," *Rev.Sci.Instrum.*, vol. 68, No.11, pp. 4236–4246, 1997.

[13] J. Liu, G. Rieker, J. Jeffries, M. Gruber, C. Carter, T. Mathur, and R. Hanson, "Near-infrared diode laser absorption diagnostic for temperature and water vapor in a scramjet combustor," *Applied Optics*, vol. 44, No.31, pp. 6701–6711, 2005.

[14] K. Gurton, R. Dahmani, D. Ligon, and B. Bronk, "In situ measurement of the infrared absorption and extinction of chemical and biologically derived aerosols using flow-through photoacoustics," *Applied Optics*, vol. 44, No.19, pp. 4096–4101, 2005.

[15] B. Frackowiak, *Approche expérimentale et simulation numérique des effets d'interactions entre gouttes en évaporation.* Phd thesis, École Nationale Supérieure de l'Aéronautique et de l'Espace, Toulouse, 2007.

[16] V. Bodoc, J. Wilms, Y. Biscos, G. Lavergne, and O. Rouzaud, "Experimental and numerical investigation of a monocomposant polydisperse spray," *Proceedings of the 22nd European Conference on Liquid and Atomization and Sprays, Como,Italy*, 2008.

[17] V. Bodoc, F. Moreau, Y. Biscos, R. Bazile, and G. Lavergne, "Experimental investigation of evaporating bi-component droplets in a turbulent channel flow," *Proceedings of the 11th International Conference on Liquid Atomization and Spray Systems, Vail, Colorado*, 2009.

[18] M. Cochet, *Evaporation de gouttelettes polydispersées dans un écoulement de canal fortement turbulent. Analyse de la formation du mélange diphasique par imagerie de fluorescence.* Phd thesis, INP Toulouse, Toulouse, 2007.

[19] D. Spalding, "Combustion of fuel particles," *Fuel*, vol. 30, 1951.

[20] A. Atthasit, *Etude expérimentale des phénomènes d'interaction dans les jets diphasiques denses au moyen de jets rectilignes monodisperses.* Phd thesis, ENSAE, Toulouse, 2003.

[21] G. Castanet, P. Lavieille, F. Lemoine, M. Lebouche, A. Atthasit, Y. Biscos, and G. Lavergne, "Energetic bidget on an evaporating monodisperse droplet stream using combined optical methods. evaluation of the heat transfer," *Int. Journal of Heat Transfer*, pp. 5053–5067, 2001.

[22] P. Lavieille, A. Delconte, D. Blondel, M. Lebouche, and F. Lemoine

[23] G. Castanet, M. Orain, F. Grisch, and F. Lemoine, "Simultaneous characterization of the liquid and gaseous phase of evaporating acetone droplets by combined planar laser induced fluorescence and two-color laser-induced fluorescence." 6th World Conference on Experimental Heat Transfer, Fluid Mechanics and Thermodynamics, Matsushima/Japan.

[24] F. Ossler and M. Alden, "Measurements of picosecond laser induced fluorescence from gas 3-pentanone and acetone: implications in combustion diagnostics," *Applied Physics*, vol. 64, pp. 493–502, 1997.

[25] G. Castanet, C. Maqua, and M. Orain, "Investigation of heat and mass transfer between the two phases of an evaporating droplet stream using laser-induced fluorescence techniques: Comparison with modeling," *International Journal of Heat and Mass Transfer*, vol. 50, pp. 3670–3683, 2007.

[26] H. Zhao and N. Ladommatos, "Optical diagnostics for in-cylinder mixture formation measurements in ic engines," *Prog.Energy Comb.Sci.*, vol. 24, pp. 297–336, 1998.

[27] J. Reboux, D. Puechberty, and F. Dionnet. SAE Paper 941988.

[28] J. Reboux, D. Puechberty, and F. Dionnet. SAE Paper 961205.

[29] L. Melton, "Spectrally separated fluorescence emissions for diesel fuel droplets and vapor," *Applied Optics*, vol. 22, No.14, pp. 2224–2226, 1983.

[30] P. Felton, F. Bracco, and M. Bardsley. SAE Paper 930870.

[31] J. Desantes, J. Pastor, J. Pastor, and J. Juliá, "Limitations on the use of the planar laser induced exciplex fluorescence technique in diesel sprays," *Fuel*, vol. 84, pp. 2301–2315, 2005.

[32] T. Tsuboi, K. Inomata, Y. Tsunoda, A. Isobe, and K. Nagaya, "Light absorption by hydrocarbon molecules at $3.392\mu m$ of he-ne laser," *Japanese Journal of Applied Physics*, vol. 24, No.1, pp. 8–13, 1985.

[33] A. Klingbeil, *Mid-IR Laser Absorption Diagnostics For Hydrocarbon Vapor Sensing in Harsh Environments*. Phd thesis, Stanford University, Cambridge, MA, 2007.

[34] N. Swanson, B. Billard, and T. Gennaro, "Limits of optical transmission measurements with application to particle sizing techniques," *Applied Optics*, vol. 38, No.27, pp. 5887–5893, 1999.

[35] J. Wang, M. Maiorov, D. Baer, D. Garbuzov, J. Conolly, and R. Hanson, "In situ combustion measurement of co with diode-laser absorption near 2.3 μm," *Applied Optics*, vol. 39, No.30, pp. 5579–5589, 2000.

[36] J. Tishkoff, D. Hammond jr., and A. Chraplyvy, "Diagnostic measurements of fuel spray dispersion." ASME Publication.

[37] K. Cashdollar, C. Lee, and J. Singer, "Three-wavelength light transmission technique to measure smoke particle size and concentration," *Applied Optics*, vol. 18, No.11, pp. 1763–1769, 1979.

[38] T. Billings and J. Drallmeier, "A detailed assessment of the infrared extinction technique for hydrocarbon vapor measurements in a controlled two-phase flow," *Atomization and Sprays*, vol. 4, pp. 99–121, 1994.

[39] J. Drallmeier and J. Peters, "Liquid- and vapor-phase dynamics of a solid-cone pressure swirl atomizer," *Atomization and Sprays*, vol. 4, pp. 135–158, 1994.

[40] J. Drallmeier, "Hydrocarbon-vapor measurements in pulsed fuel sprays," *Applied Optics*, vol. 33, No.33, pp. 7781–7788, 1994.

[41] P. Jennings and J. Drallmeier, "Pulsed-fuel-spray vapor-phase characterization," *Atomization and Sprays*, vol. 6, pp. 537–562, 1996.

[42] S. Modiano, K. McNesby, P. Marsh, W. Bolt, and C. Herud, "Quantitative measurements by fourier-transform infrared spectroscopy of toxic gas production during inhibition of jp-8 fires by cf_3br and c_3f_7h," *Applied Optics*, vol. 35, No.21, pp. 4004–4008, 1996.

[43] C. Hassa, "Infrared extinction technique for hydrocarbon vapour measurements in a two-phase flow." LOPOCOTEP Deliverable 4.15, DLR IB 325-04-04.

[44] F. Giuliani, U. Bhayaraju, and C. Hassa, "Analysis of air-blasted kerosene vapour concentration at realistic gas turbine conditions using laser infra-red absorption." Proceedings of the European Combustion Meeting.

[45] E. Tomita, N. Kawahara, A. Nishiyama, and M. Shigenaga, "In situ measurement of hydrocarbon fuel concentration near a spark plug in an engine cylinder using the $3.392\mu m$ infrared laser absoprtion method: application to an actual engine," *Measurement Science and Technology*, vol. 14, pp. 1357–1363, 2003.

[46] M. Adachi, D. Tanaka, Y. Hojyo, M. Al-Roub, J. Senda, and H. Fujimoto, "Measurement of fuel vapor concentration in flash boiling spray by infrared extinction/scattering technique," *JSAE Review*, vol. 17, pp. 231–237, 1996.

[47] K. McNesby, R. Wainner, T. Daniel, R. Skaggs, J. Morris, A. Miziolek, W. Jackson, and I. McLaren, "Detection and measurement of middle-distillate fuel vapors by use of tunable diode lasers," *Applied Optics*, vol. 40, No.6, pp. 840–845, 2001.

[48] Y. Zhang, T. Yoshizaki, and K. Nishida, "Imaging of droplets and vapor distributions in a diesel fuel spray by means of a laser absorption-scattering technique," *Applied Optics*, vol. 39, No.33, pp. 6221–6229, 2000.

[49] W. Hentschel and K.-P. Schindler, "Flow, spray and combustion analysis by laser techniques in the combustion chamber of a direct-injection diesel engine," *Optics and Lasers in Engineering*, vol. 25, pp. 401–413, 1996.

[50] L. Ricart, R. Reitz, and J. Dec, "Comparisons of diesel spray liquid penetration and vapor fuel distributions with in-cylinder optical measurements," *Transactions of the ASME*, vol. 122, pp. 588–595, 2000.

[51] L. Rothman, "The hitran database: 1998 edition," *J.Quant.Spectrosc.Radiat. Transfer*, vol. 60, pp. 665–710, 1998.

[52] K. Gurton, D. Ligon, and R. Dahmani, "Measured infrared optical cross sections for a variety of chemical and biological aeerosol simulants," *Applied Optics*, vol. 43, pp. 4564–4570, 2004.

[53] X. Ouyang and P. Varghese, "Line-of-sight absorption measurements of high temperature gases with thermal and concentration boundary layers," *Applied Optics*, vol. 28, No.18, pp. 3979–3984, 1989.

[54] F. Grossmann, P. Monkhouse, and M. Ridder, "Temperature and pressure dependences of laser induced fluorescence of gas phase acetone and 3-pentanone," *Applied Physics*, vol. 62, pp. 249–253, 1996.

[55] C. Laurent, *Modélisation de l'Evaporation de Gouttes Multicomposants.* Phd thesis, École Nationale Supérieure de l'Aéronautique et de l'Espace, Toulouse, 2005.

[56] C. Connon, R. Dimalanta, C. Choi, and D. Dunn-Rankin, "Lif measurements of fuel vapor in an acetone droplet stream," *Combust.Sci.and Tech.*, vol. 129, pp. 197–216, 1997.

[57] B. Frackowiak, G. Lavergne, C. Tropea, and A. Strzelecki, "Interactions between evaporating droplets in a monodisperse stream," *Proc. of ICLASS 2009, Vail/CO*, no. ICLASS2009-126, 2009.

[58] N. Doué, *Modélisation de l'Evaporation de Gouttes Multicomposants.* Phd thesis, École Nationale Supérieure de l'Aéronautique et de l'Espace, Toulouse, 2005.

[59] D. Hammond-jr., "Deconvolution technique for line-of-sight optical scattering measurements in axisymmetric sprays," *Applied Optics*, vol. 20, No.3, pp. 493–499, 1981.

[60] V. Bodoc, C. Laurent, Y. Biscos, and G. Lavergne, "Advanced measurement techniques for spray investigations." Internal report ONERA.

[61] J. Rheims, J. Köser, and T. Wriedt, "Refractive-index measurements in the near-ir using an abbe refractometer," *Meas.Sci. and Technology*, vol. 8, pp. 601–605, 1997.

[62] G. Pretzler, H. Jäger, T. Neger, H. Philipp, and J. Woisetschläger, "Comparison of different methods of abel inversion using computer simulated and experimental side-on data," *Z.Naturforschung*, vol. 47a, pp. 955–970, 1992.

[63] C. Dumouchel, P. Yongyingsakthavorn, P. Vallikul, and B. Fungtammasan, "Application of the maximum entropy technique in tomographic reconstruction from laser diffraction data to determine local spray drop size distribution," *Experiments in Fluids*, vol. 42, pp. 471–481, 2007.

Appendix A

Development And Construction Of A Calibration Cell

The bibliographic study shows, that only limited data on the absorption coefficients of hydrocarbons is available. Most of the publications known to the author present coefficients derived theoretically [35] or which are valid for very specific experimental conditions only [48]. An exception to this rule is the paper of Tsuboi et al. [32] which gives the absorption coefficients of several molecules for a wide temperature range. However, these values are based on a very limited number of experimental conditions which makes it difficult to interpolate between those points. In addition, no investigation on the influence of non-ambient pressure on the obtained absorption coefficients has been made. To overcome this lack of information, a calibration device, which is able to provide well defined vapor concentrations, also at elevated pressure and temperature, is developed.

A.1 The evaporation system

The system consists of an evaporation device and an optimized test cell (figure A.1). Its center piece is the Bronkhorst W-202A Controlled Evaporation Mixer (CEM). This device allows to obtain fuel vapor at defined fractions from 0 to $\approx 100\%$, from ambient conditions up to a pressure of 10 bar and a temperature of 200 $°C$. The ensemble of flow meters and CEM is PC controlled with the calibration curves for several liquids and gases stored. A short list of the main technical specifications is presented in figure A.2.
As main process gas Nitrogen was chosen with regard to the use of this system for fluorescence calibrations also. By performing the calibrations under oxygen-free atmosphere, quenching effects are avoided. Additionally, the inert chemical behaviour of Nitrogen makes it a preferable fluid to purge the system.

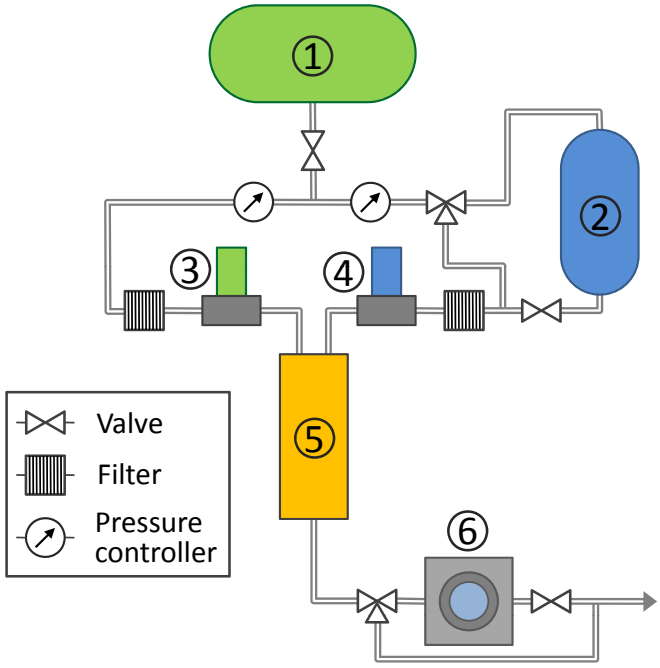

Figure A.1: Scheme of the evaporation system: 1...Nitrogen supply, 2...liquid tank, 3...gas flow meter, 4...liquid flow meter, 5...CEM unit, 6...test cell

max. liquid flow[a]	120 g/h
liquid flow precision	1% MF[b]
max. gas flow	10 l_n/min
gas flow precision	0.2% MF and 0.8% DV[c]
heating power	100 W
max. temperature	200°C

[a]based on water
[b]of maximal flow
[c]displayed value

Figure A.2: The Bronkhorst Evaporation Mixer CEM-W202A. Source: Bronkhorst

A.2 Definition of the required flow rates

Knowing the limits and precision of the CEM, a calculation of the required liquid flow rates for the planned experimental conditions can be performed. Starting from the desired molar fraction X_{liq}, the liquid mass flow $\dot{m}_{liq}$ can be derived using the following equations.

$$\dot{m}_{liq} = \frac{\dot{m}_{gas} \cdot Y_{liq}}{1 - Y_{liq}} \tag{A.1}$$

with

$$Y_{liq} = X_{liq} \cdot \frac{M_{liq}}{X_{liq} \cdot M_{liq} + (1 - X_{liq}) \cdot M_{gas}} \tag{A.2}$$

and

$$\dot{m}_{gas} = \dot{V}_{gas} \cdot \rho_{gas} \tag{A.3}$$

With Y_{liq} representing the liquid mass fraction and $M_{liq/gas}$ the respective molar masses. The conversion given in equation A.3 is necessary since the gas-flow meter works volumetrically, unlike the liquid flow meter, providing the volume flux only.
The respective liquid flow rates are calculated for mole fractions from zero to 0.95, beginning at ambient conditions up to the system limits of 10 bar and 200 $°C$. The examples in in figure A.3, expressed as percentage of the maximum flow, are calculated for 1 l/min of nitrogen at different ambient pressures.

As we can see, not all absolute mole fraction levels can be realized for most of the ambient conditions. This is due to saturation of the vapor. The theoretically needed temperature to obtain the desired mole fraction is given in brackets in the respective temperature line.
The green line marks the limit of concentration that can be reached by the system for the given gas flow rate. As an example, to achieve a molar fraction of 0.6 at the given conditions, the liquid flow would have to be nearly 130% of the maximum. In other words, to achieve higher concentration levels, the gas flow has to be reduced. This has to be done with care however, since the gas flow of 1 l/min as chosen for these calculations represents only 10% of the maximal flow rate already. By further reducing the flow, the level of the systematical errors is approached (compare figure A.2) and the accuracy of the system drop significantly.

1bar

Temperature in Celsius	Molar vapour concentration in %										
	0	10	20	30	40	50	60	70	80	90	95
20	0	9,61	21,61	--- (24,37°)	---	---	---	---	---	---	---
40	0	9,61	21,61	37,03	57,61	86,39	--- (41,5°)	---	---	---	---
50	0	9,61	21,61	37,03	57,61	86,39	129,61	201,61	345,67	--- (52,79°)	---
60	0	9,61	21,61	37,03	57,61	86,39	129,61	201,61	345,67	777,78	1641,67
...						...					
200	0	9,61	21,61	37,03	57,61	86,39	129,61	201,61	345,67	777,78	1641,67

5bar

Temperature in Celsius	Molar vapour concentration in %										
	0	10	20	30	40	50	60	70	80	90	95
20	0	--- (36,71°)	---	---	---	---	---	---	---	---	---
40	0	9,61	---	---	---	---	---	---	---	---	---
50	0	9,61	--- (55,83°)	---	---	---	---	---	---	---	---
60	0	9,61	21,61	--- (68,31°)	---	---	---	---	---	---	---
80	0	9,61	21,61	37,03	57,61	--- (85,55°)	---	---	---	---	---
100	0	9,61	21,61	37,03	57,61	86,39	129,61	201,61	--- (103,1°)	---	---
110	0	9,61	21,61	37,03	57,61	86,39	129,61	201,61	345,67	777,78	--- (110,1)
...						...					
200	0	9,61	21,61	37,03	57,61	86,39	129,61	201,61	345,67	777,78	1641,67

10bar

Temperature in Celsius	Molar vapour concentration in %										
	0	10	20	30	40	50	60	70	80	90	95
20	0	---	---	---	---	---	---	---	---	---	---
40	0	---	---	---	---	---	---	---	---	---	---
50	0	--- (55,83°)	---	---	---	---	---	---	---	---	---
60	0	9,61	--- (77,57°)	---	---	---	---	---	---	---	---
80	0	9,61	21,61	--- (92,15°)	---	---	---	---	---	---	---
100	0	9,61	21,61	37,03	--- (103,1°)	---	---	---	---	---	---
110	0	9,61	21,61	37,03	57,61	--- (112,3°)	---	---	---	---	---
120	0	9,61	21,61	37,03	57,61	86,39	--- (120,1°)	---	---	---	---
130	0	9,61	21,61	37,03	57,61	86,39	129,61	201,61	--- (132,3°)	---	---
140	0	9,61	21,61	37,03	57,61	86,39	129,61	201,61	345,67	777,78	--- (141,1)
...						...					
200	0	9,61	21,61	37,03	57,61	86,39	129,61	201,61	345,67	777,78	1641,67

Figure A.3: Determined flow rates relative to the maximum flow for acetone at a Nitrogen flow rate of 1 l/min at various pressures

A.3 The test cell

Function of the test cell (figure A.4) is to provide a calibration environment with well defined volume, laser path length and ambient conditions. A stainless steel cube with an edge length of 70 mm forms the cell body. The internal cavity has a spherical shape to minimize flow obstruction and internal recirculation, which would lead to liquid residues in corners. To maintain the vapor temperature, four electric heating elements with a total power of 1500 Watts are integrated in the body. A closely fit ceramic insulation permits save handling even at heated conditions (figure A.5).

Up to four optical accesses allow line-of-sight and laser sheet techniques. The employed quartz windows are made of Hereaus Suprasil 300©, which assures a transmittance superior to 80% for wavelengths from 175-3400 nm (figure A.6). With 7 millimeters thickness at a diameter of 26 mm their resistance to the planned elevated pressures is guaranteed.

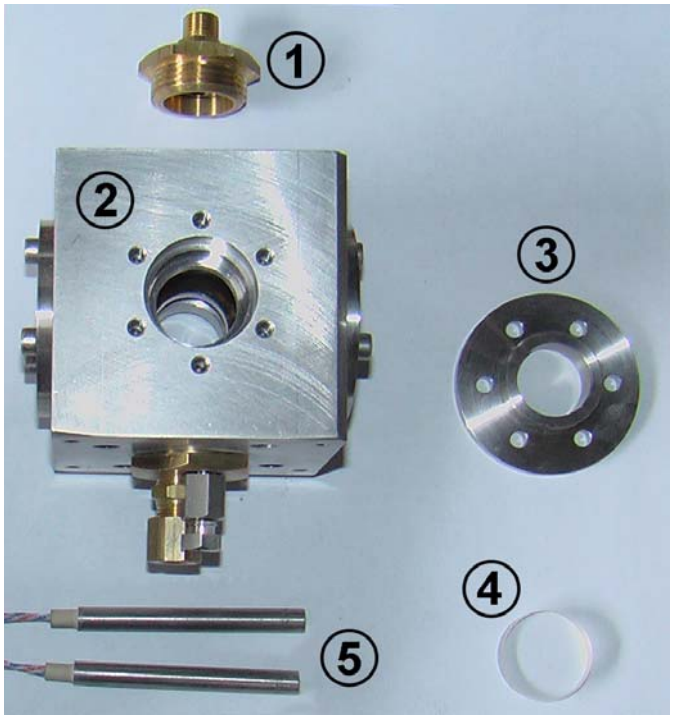

Figure A.4: Components of the test cell; 1...inlet lid, 2...cell body, 3...optical access lid, 4...quartz window, 5...heating elements

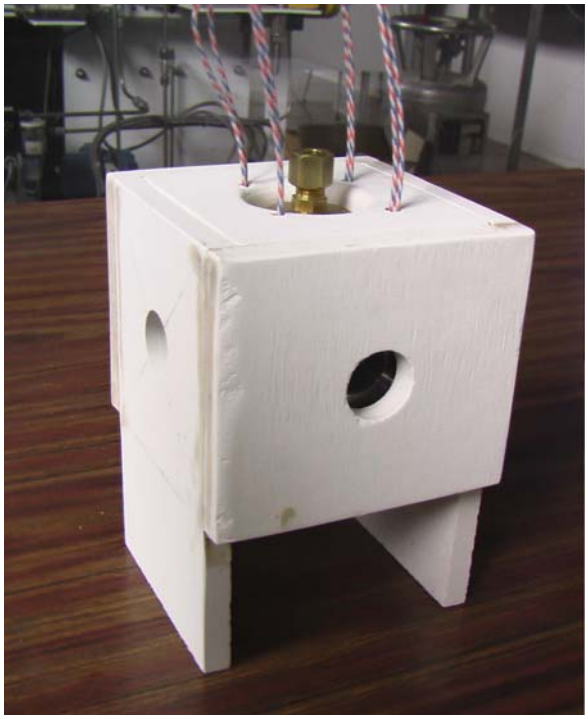

Figure A.5: Insulated assembly

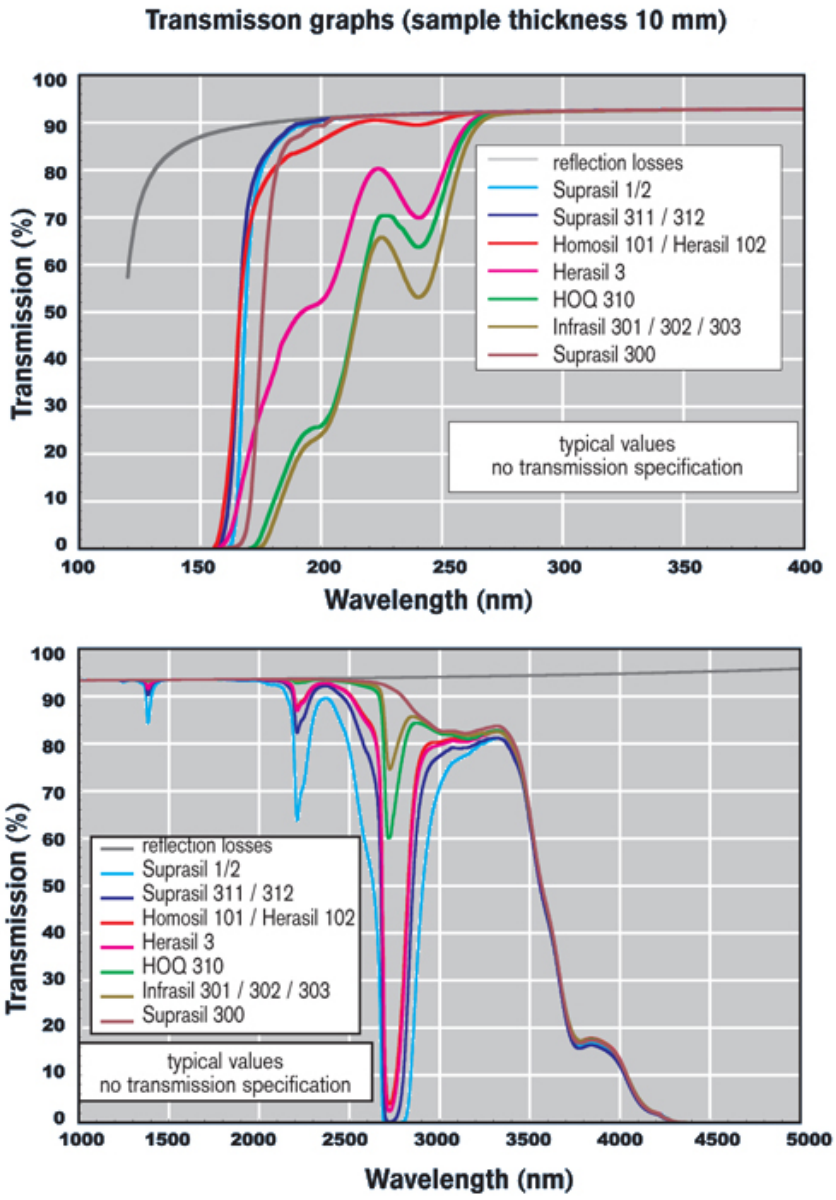

Figure A.6: Transmission of the selected window material.**Top:**UV to visible; **Bottom:**N-IR and IR: Source: Hereaus

Appendix B

2D-3D Transformation of the provided vapour fields

General problem

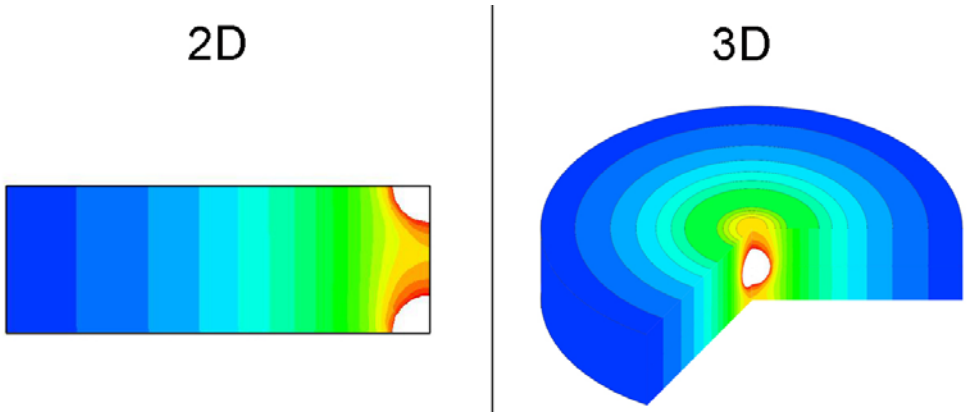

Figure B.1: Initial and desired state of the provided vapour data

Following the discussion in chapter 3.2, the DNS approach of Frackowiak was chosen as an evaporation model for the absorption simulations due to its high precision. However, the complexity of this approach does not permit a full 3D calculation because of the important computational costs. Therefore, advantage of the symmetries in the droplet stream configuration had to be taken, resulting in a 2D field between two quarter droplets (figure B.1 left). But to effectively simulate the absorption of laser energy by a vapour field of varying concentration, a complete 3D description of the volume's repartition - or at least its projection in direction of the laser propagation - is needed (figure B.1 right).
This chapter describes the Three-step-procedure, which is applied to transform the provided 2D concentration repartitions into the desired 3D format.

Steps of the transformation

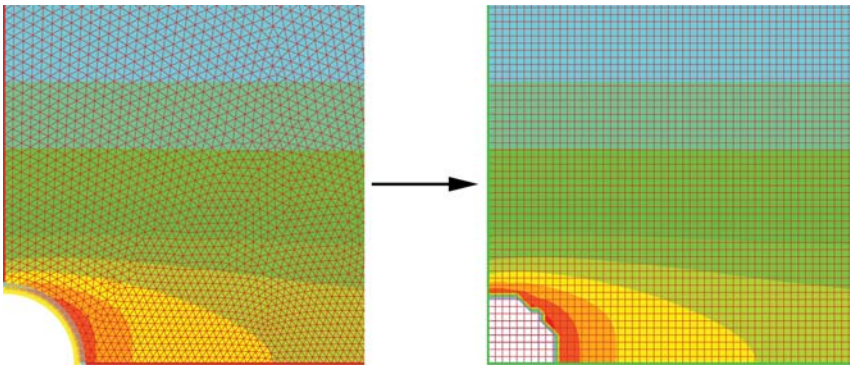

Figure B.2: Step one: Square interpolation of the vapour field

The first step of the transformation is to make the FLUENT results compatible to Matlab. For the DNS calculations, a triangular mesh was chosen by Frackowiak. This type of discretization is difficult to implement in Matlab. Therefore, the cell values are interpolated on a square Cartesian mesh. The cell width is chosen with a tenth of the droplet radius.
A comparison of the original and of the interpolated field (figure B.2) shows, that the concentration contours are well preserved. Only the interpolation of the boundary layer at the droplet interface causes slight differences in value and shape. The influence of this error on the resulting absorption profiles, however, is negligible.

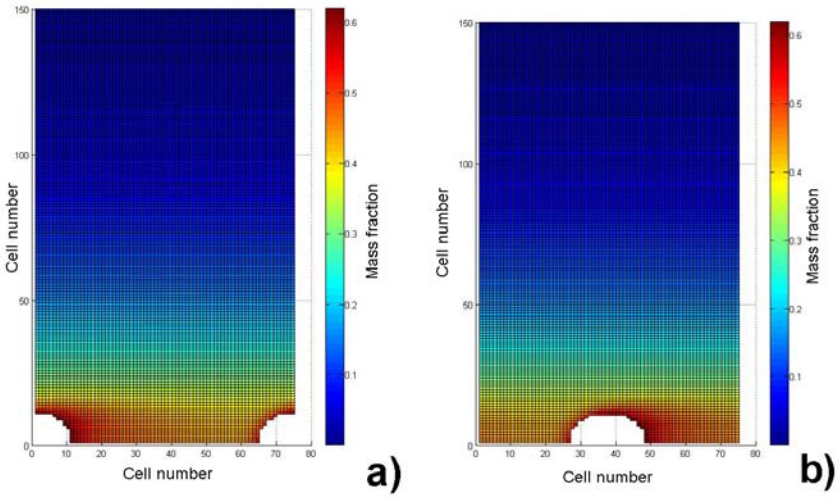

Figure B.3: Step two: Centering of the droplet

Step one provides the vapour field interpolated on a Cartesian grid, which cab easily be imported into Matlab, but is not centered on the droplet yet (figure B.3 left). As already mentioned in chapter 3.4.2, this can be achieved by a switch of some columns of the concentration matrix (figure B.3 right). Care has to be taken when choosing the separation position because of the wake in concentration after the leading droplet. Due to the fact, that the shape of this

wake strongly shifts with the flow parameters, this point is determined manually.

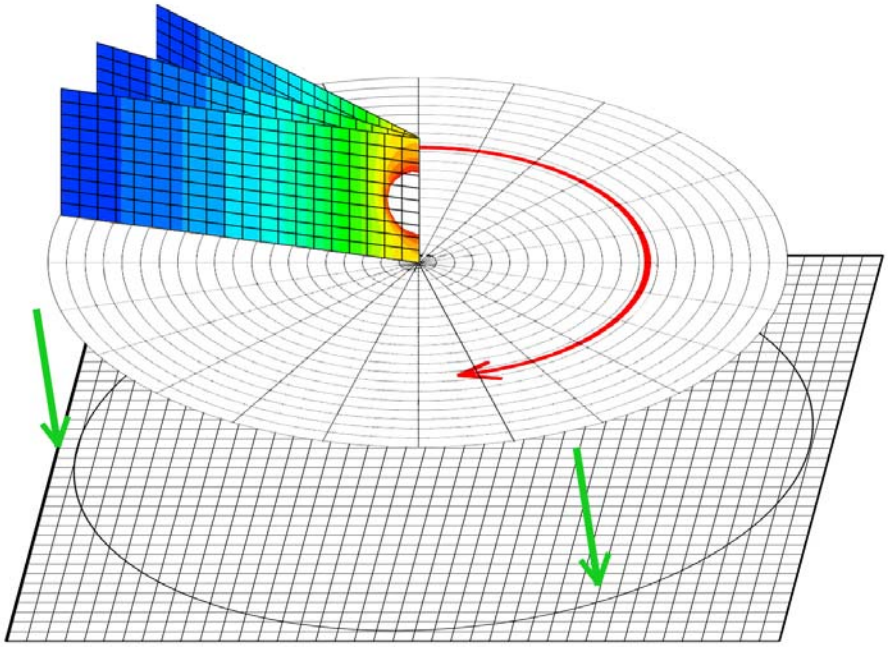

Figure B.4: Step three: Rotation and second interpolation

The third and last step consists of the rotation of the droplet-centered vapour field around the axis of propagation. As shown in figure B.4 this corresponds to multiple duplications of the concentration matrix at fixed increments of angle. The result is the desired 3D distribution of vapour concentration around a centered droplet, although in cylindrical coordinates. For this reason, another interpolation, on a 3-dimensional Cartesian grid, is performed before the resulting matrix is implemented in the absorption simulations.

Mesure de la concentration de vapeur autour de gouttes par absorption infrarouge

Cette thèse présente l'étude de la mesure de la concentration de vapeur de carburant autour de gouttes en évaporation dans un jet de gouttelettes mono-disperses et dans un brouillard au moyen de la technique par Absorption InfraRouge (AIR). L'étude bibliographique montre les limitations de la méthode utilisant la Fluorescence Induite par Laser (FIL) pour mesurer les concentrations de vapeur de carburant dans ces configurations. En raison de ces difficultés aucune quantification complète de l'évaporation dans un jet de gouttelettes en interaction ne peut être obtenue en utilisant cette technique. L'objectif de cette thèse est d'évaluer les possibilités quantitatives de la méthode AIR comme technique complémentaire ou alternative à la méthode FIL. Les moyens expérimentaux et les post-traitements des données développées pour cette recherche sont présentés. Une simulation numérique simplifiée du processus d'absorption dans un jet de gouttelettes est développée pour permettre des comparaisons avec les résultats expérimentaux. Les capacités de la méthode AIR à quantifier le champ de vapeur dans un jet de gouttelettes mono-disperses d'acétone et dans un brouillard de n-octane sont évaluées par comparaisons aux résultats d'expérience et de simulations numériques publiés. Les perspectives de développement de la méthode AIR pour quantifier la concentration de vapeur autour de gouttelettes sont discutées.

Mots clés : Gouttes en évaporation, mesure de concentration, technique absorption infrarouge, comparaison quantitative

Fuel vapor concentration measurements on droplets by infrared extinction

This thesis presents the study of measuring the concentration of fuel vapor around evaporating droplets in a monodisperse droplet stream and in a spray using the Infrared Extinction technique (IRE). A literature survey shows the limitations of Laser Induced Fluorescence methods (LIF) to measure the fuel vapor concentration in these configurations. Because of these difficulties, no complete quantification of the evaporation of droplets in interaction can be obtained using these techniques. The objective of this thesis is to assess the quantitative potential of the IRE as a complementary or alternative tool to the LIF. The experimental means and the post-processing of data, developed for this research, are presented. A simplified numerical simulation of the absorption process in a droplet stream is created to allow comparisons to experimental results. The capabilities of the IRE to quantify the vapor field in a monodisperse droplet stream of acetone and in a spray of n-octane are evaluated by comparisons to experimental results end existing numerical simulations. Prospects for the development of the IRE to quantify the fuel vapor concentration around droplets are discussed.

Keywords : Droplet evaporation, concentration measurements, infrared extinction technique, quantitative comparison